When do structural anomalies of ionic crystals begin?

Dissertation
presented to the Faculty of Physics of the TU Dortmund University, Germany, in partiall fulfillment of the requirements for the degree of Doktor rer. nat.

by

Corina Varga

Lehrstuhl für Experimentelle Physik IIa
Fakultät Physik
Technische Universität Dortmund
December 2016

technische universität dortmund

Examination board:
Prof. Dr. Manfred Bayer

Prof. Dr. Metin Tolan

Prof. Dr. Thomas Weis

Dr. Jörg Debus

Accepted by the Facultty of Physics of the TU Dortmund University, Germany
Day of the oral examination: 3.02.2017

Contents

Introduction

"There is no greater anomaly in nature than a bird that does not fly; yet there are several."

—*Charles Darwin*

Even before the invention of X-ray diffraction by M. von Laue, W. Friedrich, and P. Knipping in 1912, scientists were able to gather information about the anisotropy in cubic crystals. In those times the relevant technique was the measurement of optical birefringence in crystals. In an extensive review article and in a recently published monograph numerous examples of minerals and artificial crystals have been reported exhibiting anomalous birefringence [KM92, SPK07] . Anisotropic structural defects and inhomogeneous distributions of inclusions are considered to be the origin of anomalies in crystals. In general, optical techniques are essential for the search of residual stresses which is needed to study break of the material. The continous importance of birefringence measurements arises from their high experimental sensitivity and accuracy [Web95].

In spite of the intensive research on internal stress in the last century one fundamental problem remains. It is not possible to measure the internal sources of forces in a direct way. Since the invention of nanocrystals embedded in a isotropic transparent material, one may believe that the situation has changed [EO81, Bru83]. A new motivation for studying structural anomalies comes from the suggestion to introduce strain gradients in crystal physics. Of special interest is the so-called flexoelectric effect [BZ68, ZCT13, Res10, Tag86].

In the present work, we attempt to use the optical signal of embedded nanocrystals for the study of local forces. As an appropriate transparent and suitable material single NaCl crystals, doped by small amount of CuCl, were considered. For bravity, the doped material will be denoted as CuCl:NaCl. A further advantage is that CuCl nanocrystals can be embedded in a vitreous matrix is possible,too [AG93, KR74]. Doped crystals containing Cu^+ ions and CuCl nanocrystals were used in our project. The radii of the Cu^+ ions and the lattice parameter of CuCl are smaller to those of the corresponding sodium particles. Intuitively one expects that the small misfit produces contractive forces in the sample [WSPV04]. Roughly speaking, the concentration of copper is so small that the macroscopic properties of these samples are identical to those of a single crystal [HW98]. On the other side the average distance between two stress sources is sufficiently small to

expect mutual interactions. Notice, that the expression "small" should be related to the sensitivity of the experimental methods and to the potential influence of the defects.

In order to find a systematical approach towards structure anomalies in this system, we start with the well known stress equations of equilibrium of an elastic continuum [LL70]:

$$\frac{\partial T_{i1}}{\partial x_1} + \frac{\partial T_{i2}}{\partial x_2} + \frac{\partial T_{i3}}{\partial x_3} + f_i \;=\; 0, \tag{1}$$

where the T_{ij} are the stresses felt by the sample under consideration, i = 1, 2, 3, and the f_i represent the density of body forces. For pure crystals the only body-force is the gravitational force which is neglected here. If external forces are absent, the T_{ij} in Eq. 1 represent internal forces. In this case local forces which point towards the normal of a face should vanish if their source is positioned just at the surface. Thus, one may expect the appearance of strain gradients near to a surface.

The appeal of flexoelectricity is the ability to destroy the center of symmetry by a strain gradient which breaks the translational invariance [Tag86].

Obviously, the connection between flexoelectricity and traditional areas as defects and failure in materials is still an open question. The flexoelectricity effect in centrosymmetric materials seems to be a particular challenge and the level of flexoelectrical response in these materials is suitable for different applications [Cro06]. For the study of self-organized gradients in a single crystal as well in CuCl:NaCl system, those suppositions can be of special interest. This phenomenon is also of high importance for theory because periodic boundary conditions are needed. [Res10].

Thus, it seems to be necessary to study potential effects of the structure of an internal stress field due to self-organized nanocrystals and the spatial changes of strain. Obviously, to perform suitable experiments one should avoid the strong impact of traditional structural defects. This condition involves the control of strain of the magnitude of 10^{-6} and less. Therefore, it is necessary to use experimental techniques of high accuracy and high sensitivity [Web95, MS97, LW97]. The search for internal stress fields due to local sources is complicated because the embedded copper ions and CuCl nanocrystals are not only the sources of stresses but they also organize the structure of the elastic fields. A priori, it is not clear whether the local stresses are combined to one homogeneous field or not. In the latter case, boundaries between the different parts of the sample exist and a traversing optical wave will report the average of positive and negative impacts. Thus, it is difficult or even impossible to guess the correct structure of internal stress fields and the embedding of detectors will be a useful addition to already existing indirect methods.

In Chapter 1 we describe the basic theory of the phenomena which are considered to be helpful for understanding the experiments. The experimental techniques applied are shortly described in Chapter 2. The experimental results and a short summary are outlined in Chapter 3. Chapter 4 presents the most important experimental results.

Chapter 1

Theoretical background

1.1 Definition of a crystalline structure

In this work it is important to distinguish three types of a crystalline material.

(I) The ideal crystal consists of identical unit cells which fill the space of a sample completely and the atoms occupy geometrical positions which obey the rules of a space group lattice. This leads to a translational invariance.

(II) A less ideal crystal contains imperfections which modify its properties without breaking the basic definitions of a crystalline state.

(III) Anomalies should indicate the existence of internal forces or structural interactions. Typically, those anomalies are unusual or even forbidden for the assumed space group of the ideal crystal.

The difference between type (I) and type (II) materials is mainly a matter of defect concentrations. Experimental results reported for a new material are usually understood in the sense that the concentration of defects is "sufficiently small" and that Neumann's principle is respected [Neu23]. "Neumann's Principle" represents the most important concept in crystal physics which claims that the symmetry and any physical property of a crystal must include the symmetry elements of the point group of the crystal.

NaCl is a cubic crystal belonging to the point group $m3m$. The CuCl:NaCl system can be considered to be also a member of the aperiodic crystals family. Usually, in aperiodic crystals the structural deviation from a ideal single crystal is significantly stronger compared to CuCl:NaCl crystal and the structural modifications usually known [TLE$^+$11]. The detection of an anomaly needs experimental techniques with high sensitivity and careful measurements. If the CuCl:NaCl system is in the state (I), it shows only few optical properties which are not consistent with the crystallographic structure. Such anomalies are more easily detected in materials with a nominal isotropic structure.

1.2 The impact of defects in crystals

In general, in a real crystal the atomic arrangement does not respect the perfect crystal model. All real crystals contain imperfections which disturb locally the regular atomic

arrangement. For example, the atomic arrangement in $NaCl$ is described by alternating Na^+ and Cl^- ions in a three-dimensional simple cubic lattice. A lattice defect in NaCl means the absence of a Na^+ or a Cl^- ion. Obviously, the crystal properties such as density and elastic constants are usually modified by the concentration of defects. Considering the basis geometry, the defects in crystal can be classified in the following way:

(1) Point defects are defined as atoms or ions may which are missing from the crystal structure, thus such defects are called vacancies.

(2) Line defects or dislocations are described by excess of atomic planes introduced in the crystal. Another dislocation type are screw dislocations. These are characterized by the twisting of atomic planes in a spiral form.

(3) Two-dimensional defects are defined as boundaries between parts in the crystal which are tilted at different angles with respecting the atomic planes.

(4) Three-dimensional or volume defects are defined as three dimensional conglomerations of atoms or vacancies.

1.2.1 Point defects

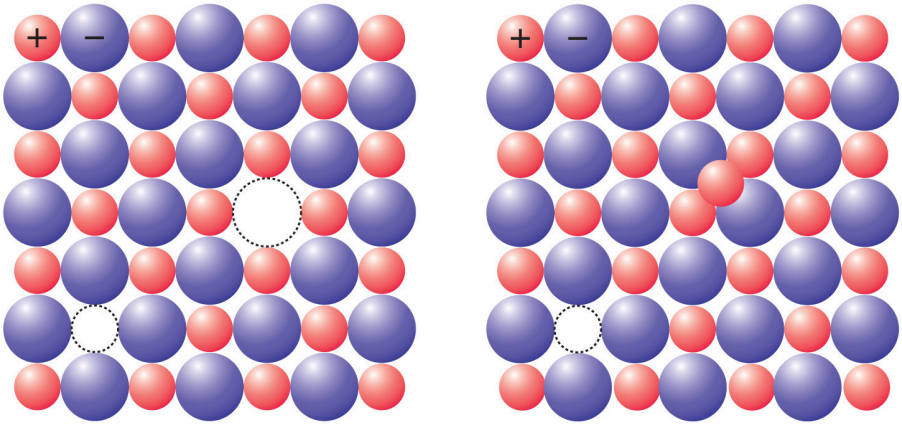

Figure 1.1: Point defects in ionic crystals. Schottky defects on the left side and Frenkel defects on the right side.

Vacancies are defined as unoccupied atom sites. In general, those defects can be categorized as Schottky or Frenkel defects. In order to generate a Schottky defect inside in a crystal, an atom has to be removed from its place in the crystal and placed in a surface. This remove process is followed by relaxation of the structure around the vacancy. The second important point defect is the interstitial atom. In this case an atom is placed in a position that is not a site in the perfect crystal. In order to generate an interstitial atom, an atom may be removed from a normal site in the bulk of the crystal to an interstitial site, producing an interstitial atom and a vacancy and this defect pair is known as Frenkel defect. In a NaCl crystal, Schottky defects are described by a cation-anion pair and the Frenkel defects are defined by an interstitial ion and the corresponding

vacancy. Experiments have revealed that Schottky defects are dominant in NaCl crystals. Their existence has a special importanece in nulceation process [Hul75].

1.2.2 Dislocation. Plastic deformation

Line imperfections or one dimensional defects are called dislocations [Ame58]. They are characterized by a strong change in the atomic arrangement along a line and this line describes the displacement in the atomic arrangement. Line defects appear when an extra incomplete or an additional atomic plane in the crystal structure is inserted. These defects always start at the surface of the crystal. Simple ionic crystals are considered not only as good prototype systems to study dislocations but also as a concerned model to explain the dislocations in metals. Even nowadays, NaCl crystal represents a prototype system to study the mechanisms of dislocations in crystal.

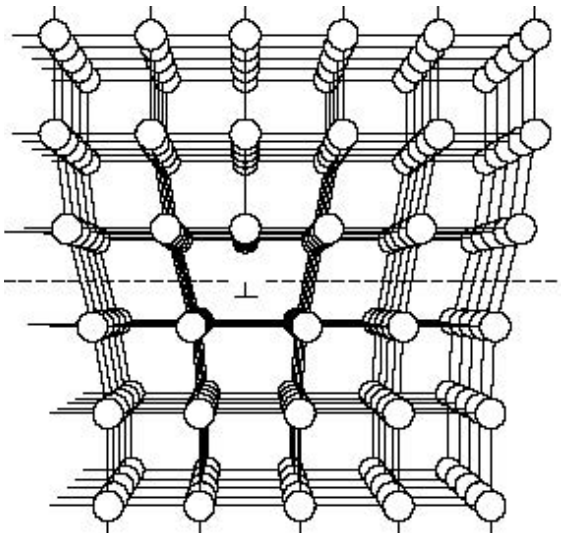

Figure 1.2: A pure edge dislocation in a simple cubic structure, according to [Spr76].

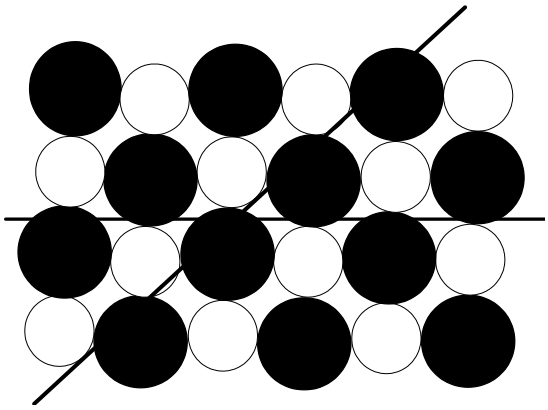

Figure 1.3: Glide planes in the NaCl structure: (diagonal line)-[110] represents the first glide plane and [100] describes the second glide plane- (horizontal line), according to [Spr76]

A pure edge dislocation in a simple cubic structure is illustrated in Fig. 1.2. In the second vertical atomic plane, the ions have exactly the same positions but the opposite sign. The third vertical atomic plane is again the same as the first etc. The edge dislocations can be considered as introducing two supplementary half atomic planes of the (110) type. The atomic half planes are necessary to maintain charge balance. These extra planes are adjacent to the normal atomic planes of the crystaline structure, thus the dislocations are not extended as in face centred cubic metals [Ame58]. Edge dislocations arise when a slight mismatch in the orientation of the adjacent part of the growing crystal exists. Line defects can start at the surface of a crystal and at grain boundaries, but never inside a

crystal. Line defects have the ability to move inside the crystal. Those movements are known as glide and climb types.

A crystal structure can recover at the original size and shape when the external applied stress is very small [Spr76]. The minimal value of stress when the crystal is able to recover when the external applied strain disappears is defined as yield stress. If the applied external stress is large enough, after removing the external forces, the crystal suffers a plastic deformation [Spr76]. A classification of crystals due the ability to store deformation is:

(1) A material is defined as a ductile material when it is deformed under tensile stress and is able to store a large amount of deformation before breaking occurs.

(2) A material is defined as a brittle material when it breaks without significant deformation-strain (glasses, polymers, ceramics, steel at low temperature).

The plastic deformation is a property of crystals which under external stress can recover a part of strain when the stress vanishes. In ionic crystals the plastic deformation occurs by gliding. The gliding direction corresponds to close-packed ions or to a successive displacement of one atom plane over another. This plane will be called slip plane. The slip plane corresponds to the highest density of atoms and the slip direction describes the direction in the slip plane where the most atoms are closely spaced. The combination of the glide plane and the glide direction is defined as the glide system or the slip system. It is well known that rupture in a crystal is related to several mechanisms. The most important of them are known as elastic deformation, plastic flow, yielding, work hardening, movement and multiplication of dislocations.

In general, under external stress, the deformations in NaCl occur most easily along the [110] direction as illustrated in Fig. 1.3 [JKL24]. Thus, [110] is defined as the easy glide system or first glide system in NaCl. [100] represents the second glide system and coincides with the cleavage plane.

The plastic deformation mechanisms in crystalline structures are detectable when the applied stress in the glide direction reaches the critical value of the shear stress. If the external applied stress increases the material can break. Breaking in the material occurs when the external stress indicates the elastic limit. Plastic anisotropy occurs in crystalline structures when the glide planes are activated [Gil59].

Many simple ionic crystals are brittle at room temperature and single crystals cleave readily. The cleavage plane is considered to be, usually, the plane which contains anions and cations in close contact. In NaCl, the elastic limit for the (100) glide is 3 times larger than that in the (110) plane [Bue30, Dom34]. Since this is not directly connected to the gliding process, NaCl crystal can break by brittle fracture although plastic flow has been activated [NTH02]. Thus, the external applied stress $T \geq T_{crss}$ drives the movement of dislocations on glide-planes.

In ductile materials, T_{crss}, may be identified as yield point or the critical resolved shear stress [Spr76]. A second stage of external stress is T_f, characterizing the value at which atomic bonds break permanently. In brittle materials, the maximum value of the external applied stress T_f is near to T_{crss}. In ductile material, the shape of crystal changes in the range $T_{crss} < T < T_f$ (where T respresents the external applied stress) due to gliding

mechanisms and the material fails at T_f. Thus, a material break mechanism due to atomic sliding through dislocation motion is observed [Abr03].

The external applied stress $T \geq T_{crss}$ drives the movement of dislocations to the glide-planes. If the dislocations are trapped by pinning centers, the accompanying strain will be stored inside the material. The ability to store strain offers the possibility to investigate the elastic interaction between the CuCl nancrystals and the NaCl matrix [WSPV04].

1.3 Phenomenological theory of flexoelectricity

The name "flexoelectricity" comes from Latin, "flexus" means bending. Thus a strain gradient occurs in the usual way due to bent of a plate. Flexoeletricity was predicted long time ago but its direct study was difficult. Even our days, the flexoelectric effect seems to be not completely resolved due to the fact that the corresponding responses are superposed with other secondary effects. Currently, the flexoelectric effect or flexoelectricity is researched in two different areas of condensed matter physics, namely in soft materials (such as liquid crystals and biological materials) and in common solids. Nevertheless, this effect can offer explanations for different phenomena especially at the nanoscale.

The flexoelectric effect is defined to be the response of electrical polarization under a mechanical strain gradient [Cro06]. The flexoelectric effect in solids was identified for the first time theoretically by Mashkevich and Tolpygo in 1950 based on the lattice dynamics in crystals [MT57, Tol63]. The first phenomenological theoretical model which describes the flexoelectric effect was introduced by Kogan in 1964 [Kog64]. This model is based on the electron-phonon coupling in centrosymmetric crystals where it is expected that the flexoelctric response may play an important role. Flexoelectricity appears to be interesting for practical applications in ferroelectric materials. Flexoelectricity has been studied in the classical ferroelectrics $BaTiO_3$ and $SrTiO_3$ where a spontaneous polarization driven by a strain gradient was detected [BZ68].

The flexoelectric effect is defined by the linear response of polarization $\mathbf{P}$ to the strain gradient. This is a fourth-rank tensor described by:

$$P_i \;=\; \mu_{klij} \cdot \left(\frac{\partial u_{kl}}{\partial x_j} \right), \tag{1.1}$$

where $\left(\frac{\partial u_{kl}}{\partial x_j}\right)$ corresponds to the strain and the (μ_{klij}) describes the flexoelectric coefficient. Deeper research and systematical studies followed in ferroelectric ceramic materials from which it was concluded that the flexoelectric response can be several orders of magnitude larger compared to the predicted results from theoretical estimations. The trend to miniaturization leads to structures in the nanoscale range and as the length scales decrease larger strain gradients and flexoelectric effects are expected.

The flexoelectric effect depends on the relative strength of elastic properties, dielectric coefficients and flexoelectric coefficients. Usually, flexoelectricity occurs at the nanoscale size < 10 nm but observation were also reported in the scale of hundreds of nanometers [ZCB$^+$08, MC03, ZCT13, MC06]. In soft materials, experimental results show that

the flexoelectric response is of the same order or even larger compared to crystalline structures [SGB03].

In a large sense, the flexoelecric effect is considered to be a typical property which is allowed in all dielectric materials or centrosymmetric crystals. It leads to a coupling of the polarization and the strain gradient. Nevertheless, it is well known that homogeneous stress and strain are not able to break the symmetry of crystals.

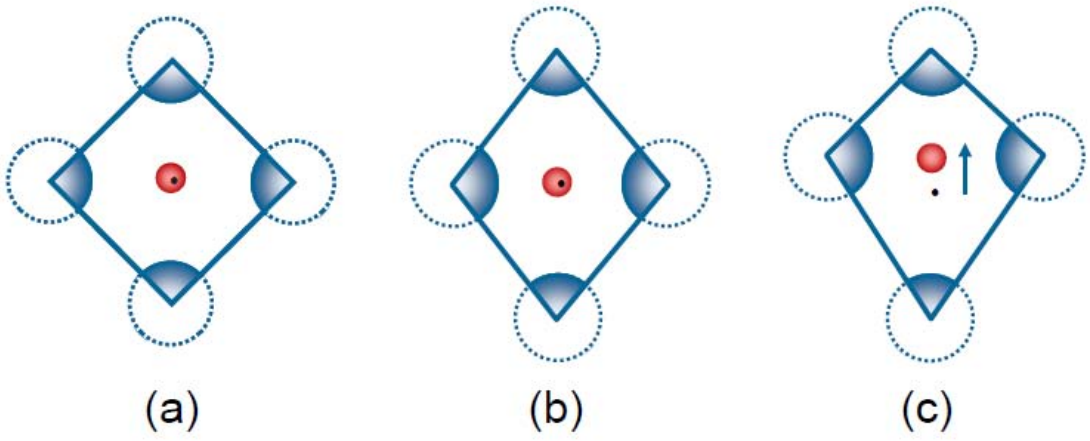

Figure 1.4: Part of a simple unit cell: a) free unit cell, b) unit cell under homogeneous deformation, and c) unit cell under inhomogeneous deformation. Negative ions depicted in blue, positive ions depicted in red and black dot represents the center of negative charge. The arrow indicates the direction of the flexoelectric polarization, according to [CSG04].

Considering a centrosymmetric material like in Fig. 1.4(a) and applying a homogeneous stress, the resulting displacements of ions are symmetric and the centers of negative and positive charge coincide with each other, resulting in null polarization Fig. 1.4(b). The situation is different, if an external strain gradient is applied. In this case, the displacements of the charges are different from each other and thus a dipole moment is generated in the opposite direction to the strain gradient. Thus, as a consequence of displacements a polarization appears (see Fig. 1.4(c)).

The flexoelectric coefficients were estimated using the standard theoretical model and their magnitude can be compared to the $(\frac{e}{a})$ value, where (e) describes the electronic charge and (a) represents the lattice parameter [Kog64]. The flexoelectric phenomenon includes several contributions [Tag86]. Obviously, these are divided into two contributions, namely the static flexoelectricity effect such as due to bending in a thin plate and the dynamic bulk effect due to waves traveling in the dielectric material [ZCT13].

Static flexoelecricity arises from several mechanisms: bulk flexoelectricity, surface flexoelectricity and surface piezoelectricity.

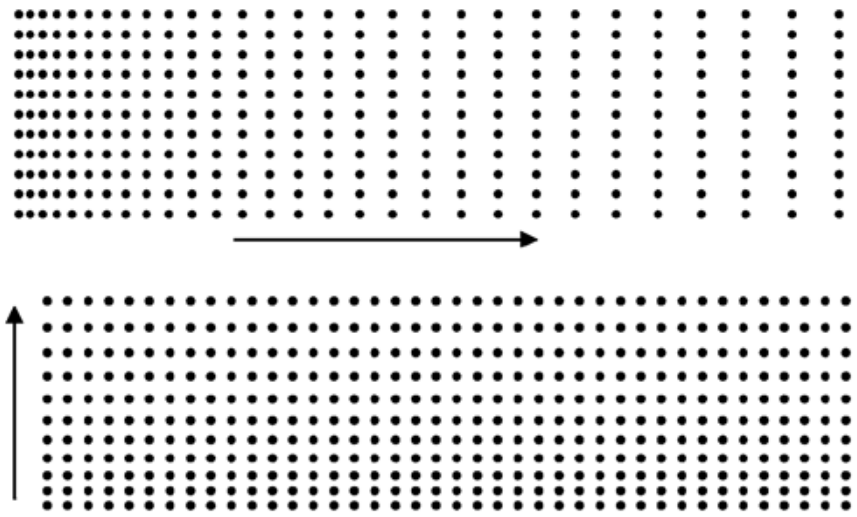

Figure 1.5: Model with a built-in uniform strain gradient (uniaxial). The x-direection is described by the arrow in each panel. Top: Traverse case where strain, strain gradient, and polarization are parallel to the model, while the field vanishes. Bottom: Longitudinal case—in this case strain, strain gradient polarization and depolarization fields are all normal to the model, according to [Res10].

Taking into accont the constitutive equation the electric polarization is given by [Kog64, Tag91, Tag86]

$$P_i = \chi_{ij} \cdot E_j + d_{ijk} \cdot u_{jk} + \mu_{klij} \cdot \frac{\partial u_{kl}}{\partial x_j}, \tag{1.2}$$

where the E_j represent the macroscopic electric field, the (u_{jk}) represent the strain tensor and the $\left(\frac{\partial u_{kl}}{\partial x_j}\right)$ describe the spatial strain gradient, respectively. The first and second terms of Eq.1.2 characterize the dielectric and the piezoelectric response with the tensor of dielectric susceptibility (χ_{ij}) and the piezoelectric tensor (d_{ijk}), respectively. The last term of Eq.1.2 describes the linear polarization response to a strain gradient following the definition of the the flexoelectric effect.

The strain tensor is defined as the symmetric part of the tensor $\left(\frac{\partial U_l}{\partial x_j}\right)$, and $u_{jk} = \frac{1}{2}(\frac{\partial U_j}{\partial x_k} + \frac{\partial U_k}{\partial x_l})$. The U_i is defined as the displacement of point (x_j) in the material. The (μ_{klij}) form a fourth rank tensor and they are called flexoelectric-coefficients. They control the flexoelectric effect, see Eq. 1.2. The relative contribution of bulk flexoelectricity and surface piezoelectricity are considered to be independent of sample thickness [Tag86].

Surface flexoelectricity decreases inversely proportional to the sample thickness and may be in principle neglected for the bulk sample contributions. Resta defined the flexoelectricity to be the linear response of polarization to a strain gradient and proved that there is no additional contribution to flexoelectricity except of the bulk contribution.

The flexoelectric tensor is defined as the bulk response, manifestitly independent of the surface contribution [Res10].

Flexoelectricity and piezoelectricity can be considered as the properties of the materials in the absence of a macroscopic electric field.

Piezoelectriciy is defined to be the ability of a material to convert electrical stimuli into mechanical deformation. The piezoelectric effect is allowed only in non-centrosymmetric materials while the flexoelectric effect is allowed in all centrosymmetric materials. This characteristic feature makes the principal difference between both effects. The piezoelectric and flexoelectric tensors describe the properties of a material in the absence of macroscopical electric field. The piezoelectic tensor is described by:

$$d_{ijk} = \left(\frac{\partial P_i}{\partial u_{jk}}\right)_{E=0}, \tag{1.3}$$

where the P_i represent the polarization and the (u_{jk}) represents the elastic strain which occurs in non-centrosymmetric materials. Considering the case when the polarization and strain gradient are homogeneous, the flexoelectricity is described by:

$$\mu_{klij} = \chi_{ij} \cdot f_{klsj}. \tag{1.4}$$

According to Equation1.4 the flexoelectric and flexo-coupling tensors suggest that the flexoelectric response should be enhanced in materials with high dielectric constants (high-K materials) such as ferroelectric materials. The flexoelectric coefficients (μ_{klij}) are proportional to the permittivity and the (f_{klsj}) form the flexo-coupling tensor. Considering the strain gradient effect to be very small in the absence of an electric field, the polarization is described by:

$$P_i = \mu_{klij}\frac{\partial u_{kl}}{\partial x_j}, \tag{1.5}$$

In the case of finite samples, the surface contributions are always considered to exist. The surface-piezoelectricity induces a flexoelectric response in the bending mode [Cro06]. The polarization arises due to the surface piezoelectricity and is related with the bulk value of the dielectric constant and the effective flexoelectricity due to the surface. A strain gradient can be generated in special devices which are defined as nanocomposite structures with built-in shape gradients [FCL99] and those are able to produce an effective piezoelectric response [Cro06, FCL99, FZL$^+$07]. These devices are built of an array of truncated dielectric pyramids with high flexoelectric coefficients. They are embedded in another medium and inserted between two metallic plates and when the plates are compressed, a strain gradient can be generated in each pyramid. Thus, a flexoelectric polarization and an effective piezoelectric response are induced.

The flexoelectric effect is investigated by different ab-initio methods. Density Functional Theory (DFT) is a method to calculate the flexoelectric coefficients from the dynamic matrix of the crystal. The components of the flexoelectric tensor were calculated for $BaTiO_3$ and for $SrTiO_3$ [MS09]. Another method to determine the flexoelectric coefficients consists of direct calculations of the polarization response in an inhomogenously

deformed crystalline lattice of ferroelectric pervoskites [HV11]. This approach uses a static strain wave which fixes the positions of the atoms. In view of Kogan's estimation and this ab-initio approach, a strong difference of the flexoelectric coefficients for $BaTiO_3$ and for $SrTiO_3$, respectively, were obtained.

The flexoelectricity in solid materials can be directly evaluated. Obviously, two different experimental methods are possible. The first one is an analysis of the phonon spectra. The second method represents a macroscopic characterization of the electrotechnical response of a finite sample. Usually, both experimental methods provide different information about the phenomenon. The phonon spectra give information in which the static and dynamic bulk flexoelectricity are involved. The static flexoelectric response can be determined by a dynamical bending procedure in a cantilever-beam geometry in order to generate a strain gradient. Nevertheless, the flexoelectric polarization can be determined measuring the displacement in the currentscale [MC01, MC02, MC05, MC06]. The flexoelectric coefficients in perovskite ceramics were determined from cantilever bending and pyramid-shape structures under compression of $(Ba, Sr)TiO_3$. In $SrTiO_3$ good agreement between experimental and theoretical results was obtained.

The considerable effort expended on theoretical and experimental studies of flexoelectricity so far seems to have yielded only limited understanding of this phenomenon in real systems. Therefore, this phenomenon has still open questions.

1.4 Copper Chloride system

1.4.1 Crystal symmetry and structural properties of CuCl

Copper-Halides, I-VII compounds, have received considerable attention in the 1960's and 1970's, primarily for their excitonic properties but also due to potential applications. The attractiveness of these compounds arises from their non-linearity effects [Gol77, MKK95, MWK92]. They have been intensively probed in the visible and ultra-violet spectral ranges [Nik80, Car63]. A wide class of semiconductors systems have been prepared in nanocrystal form including III-V, II-VI and I-VII compounds [Wog97, Yof93, BEI96]. The technology, in many cases, aims at a control of the size, the shape and the surface of the nano-semiconductor crystals [Bru83].

Copper-Halides are members of semiconductors with four valence electrons per atom. Among these semiconductors are the elemental semiconductors of group IV of the periodic table which are purely covalent bound and crystallize in the diamond structure type with (O_h) space group. Most of these semiconductors crystallize, under ordinary conditions, in cubic zinc-blende structure with (T_d) space group or hexagonal wurtzite structure type with (C_{6v}) space group. Most I-VII compounds, therefore, are octahedrally coordinated and adopt a rock-salt arrangement. Nevertheless, CuCl, CuBr and CuI also form zinc-blend or wurtzite structures. Thus, the Cu^+-Halides are situated in the region between tetrahedral and octahedral coordination.

The ionicity of the compounds increases with increasing distance of the elements within the periodic table of elements. Obviously, I-VII compounds are found to be strongly ionic;

thus the ionicity approach is based on the critical threshold of the zincblende structure. They become unstable with respect to the more closely packed rock-salt or CsCl structure and due to this instability can undergo a phase transition of polymorphous form [ABT$^+$06].

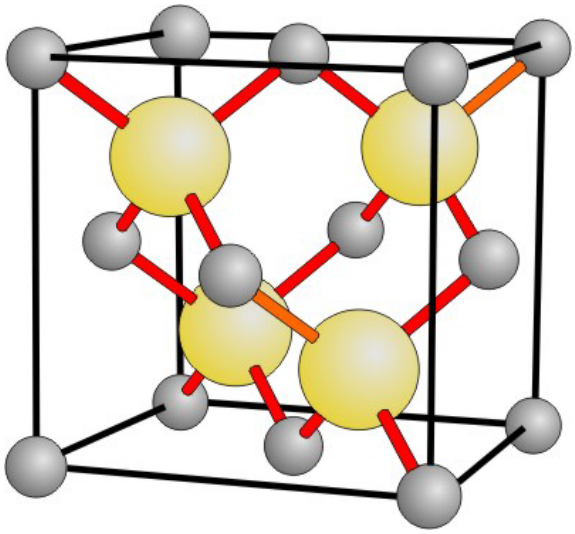

Figure 1.6: Unit cell of cubic phase CuCl. (gray spheres) represent Cu^+ ions and (orange spheres) represent Cl^- ions. The coordinates of the atom Cu^+ are:: $(\frac{1}{4}\ \frac{1}{4}\ \frac{1}{4})$; $(\frac{1}{4}\ \frac{3}{4}\ \frac{3}{4})$; $(\frac{3}{4}\ \frac{1}{4}\frac{3}{4})$; $(\frac{1}{4}\ \ \frac{3}{4}\frac{3}{4})$.b) The coordinates of the atom Cl^- are: (000); $(0\frac{1}{2}\frac{1}{2})$; $(\frac{1}{2}0\frac{1}{2})$; $(\frac{1}{2}\frac{1}{2}0)$.

As shown in Fig. 1.6, each atom of Cl^- from group VII is surrounded by a regular tetrahedron constructed from four atoms of Cu^+, forming its next neighbors at a distance of $\left(\frac{a\sqrt{3}}{4}\right)$ where (a) is the lattice parameter. CuCl is composed of two interpenetrating f.c.c of O_h sub-lattices occupied by Cu^+ and respectively by Cl^-. The important feature in this system is the lack of an inversion or symmetry center. The asymmetrical nature of CuCl leads to piezo-electrical effects. Notice, the ambiguity with respect to the sign of differently oriented sub-lattices.

At ambient pressure, CuCl undergoes a phase transition at 680 K to the wurtzite structure (β-CuCl) before it reaches the melting point at 695 K [Car63, Gol77]. (β-CuCl) is a super-ionic conducting phase and a static compression favors transition to more dense structures. This is also the case when CuCl transforms into the rock-salt structure as an intermediate tetragonal structure and the CsCl structure with increasing pressure.

1.4.2 Band Structure and Electronic Properties

Crystalline solids are classified as metals, insulators and semiconductors. This classification is based on the band gap energy and the position of the Fermi energy. The materials where the Fermi level is located between valence and conduction bands are defined as semiconductors or possibly as insulator materials. Isolated atoms that are brought together in a crystal structure give rise to an overlapping periodic potential as their electron wave

functions overlap due to shorter inter-atomic spacing. Since two electrons cannot possess the same quantum state the broadening of the discrete electron state into "bands", appear. Thus, in semiconductors the valence band represents the filled band, and the conduction band which is described as the next highest band above the valence band, exists as empty band. The distance between these two type of bands is defined as the band gap (E_g) of the material.

In the elemental semiconductors, the valence bands arise from the bonding of the (sp^3) hybrid orbitals, and the conduction band arises from the anti-bonding (sp^3) hybrids. On the other side, in the case of ionic binding, the valence bands arise from the highest occupied (p)-levels of the anions with a more or less pronounced mixture with (d) levels of the cations. The conduction band states originate from the lowest empty s levels of the cations. In CuCl, the valence band is formed by a hybridization of the filled ($3s^2 3p^6$) noble-gas shell of Cl^- ions and the ($3d^{10}$) shell of Cu^+ ions [MSW$^+$93].

Due to the hybridization between the halogen p orbitals and the Cu-(3d) orbitals, the physical properties of these semiconductors are altered with respect to those of the other families [GRC$^+$98, Gol77]. In particular, their first absorption edge occurs at a much lower energy than expected by extrapolating the corresponding edge of the isoelectronic II-VI compounds.

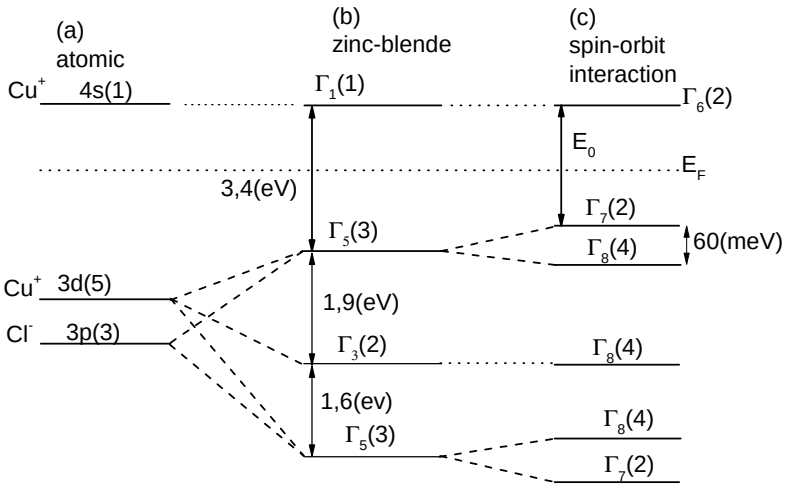

Figure 1.7: Scheme of CuCl conduction and valence band. a) Atomic levels of Cu^+ and Cl^-. b) Partial lifting of degeneracy and hybridization by the crystal field. c) Spin-orbit splitting which is responsible for the level splitting between (p) and (d) states, according to [GRC$^+$98].

In the CuCl system, the spin orbit splitting is different compared to other Cu^+-Halides compounds. The spin orbit interaction between (p) and (d) orbital states with Γ_5 leads to a splitting into separate levels with Γ_7 and Γ_8 symmetry. As a consequence, the spin-orbit coupling in CuCl is reversed compared to other zinc-blende semiconductors structures [GRC$^+$98]. The relative atomic states of Cu^+ and Cl^- are described in Fig. 1.7,

the orbital copper levels are split into two Γ_5 and one twofold degenerate Γ_3 level. The hybridization with Cl^- (p)-levels with the same symmetry results in two threefold degenerate Γ_5 levels. This hybridization raises the top of the valence band relative to the anion Cl^- the (p)-level, in the absence of Cu^+ cations the (d)-orbital would determine the valence band maximum. The (d) states contribute a negative spin-orbit term causing the valence bands to be flipped: the two-fold degenerate Γ_7 states are at higher energy than the four-fold degenerate Γ_8 states [Car63].

In linear optical experiments performed on CuCl two Wannier excitonic transitions were observed just below to the band gap [Wan37].

Table 1.1: Correlation between atomic (s) and (p) levels in conduction and valence band of symmetry-group T_d [KDWS63].

Atomic level	**Orbital momentum angular**	Γ	**Degeneracy**	**Spin**
s	0	Γ_1	1	$\frac{1}{2}$
p	1	Γ_5	3	$\frac{1}{2}$

Table 1.2: Correlation between (s) and (p) atomic levels in the conduction and valence band for symmetry-group T_d [KDWS63]

Atomic levels	**Total angular momentum j**	Γ	**Degeneracy**
s	$\frac{1}{2}$	Γ_6	2
p	$\frac{3}{2}$	Γ_8	4
p	$\frac{1}{2}$	Γ_7	2

The important energy scales are: (E_g) represents the direct band gap energy of 3.43 eV, Δ_{so} describes the spin-orbit band energy of 60 meV and a small indirect band gap 0.41 eV has been observed [GRC$^+$98, GW83]. Of most interest in CuCl are the excitons which arise due to excitation of an electron from the Γ_7 valence band up to the Γ_6 conduction band. Copper-Halides occupy an important position among the binary semiconductors, since they form the end-points of several isoelectronic series. CuCl has a dipole-allowed direct gap that increases with increasing temperature. The unique band structure of CuCl has been determined through a combination of theory and the influence of experimental interpretation [DW79, ZC79]. In most tetrahedrally coordinated semiconductors, the conduction and the valence band arise from (sp^3) hybridization of the atomic states.

1.4.3 Excitons. Quantum confinement effect

In a direct band-gap semiconductor the electrons are excited to the conduction band when light with a photon energy in excess or equal to the band-gap illuminates a sample. The interval between the top of the valence band (E_v), and the bottom of the conduction band, (E_c) is called the band gap energy, (E_g). The minimal band gap (E_g), between the valence band and the conduction band occurs at the same (k), crystals of this type are called direct-gap semiconductors. The electrons in the conduction band of a crystal can be described by a negative charge (-e), spin ($\frac{1}{2}$), and mass (m_e). An electron in the conduction band is the primary elementary excitation of the electron sub-system in the crystal. The further elementary excitation is a hole (h) which is a quasi-particle relevant to an ensemble of electrons in the valence band from which one electron (e) is removed. The hole (h) is described by a positive charge (+e), spin ($\frac{1}{2}$) and effective mass (m_h). The electron leaves a hole in the valence band and the Coulomb attraction between the two opposite charges binds them together generating an exciton of Wannier-Mott type [Wan37]. The exciton is able to travel freely throughout the lattice. A transition from the ground state occurs as the result of some external perturbations, for example, photon absorption with energy and momentum conservation.

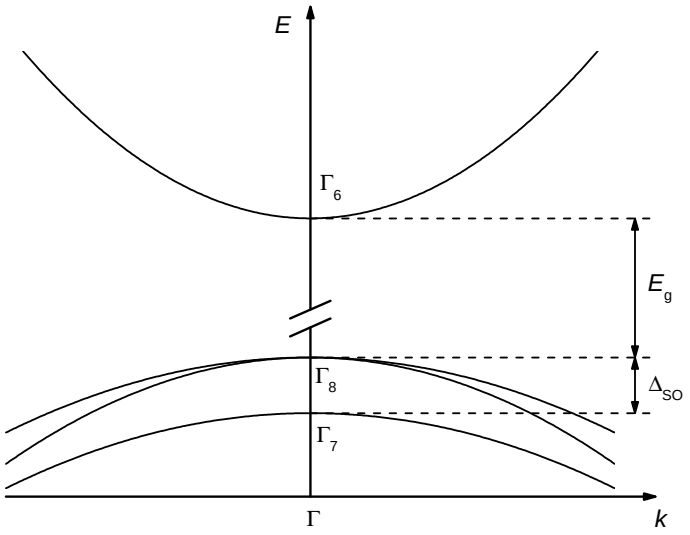

Figure 1.8: Schematic band diagram in $CuCl$ near the Γ point at $\vec{k} = 0$. $CuCl$ shows the inverse ordering of the upper valence bands, the twofold degenerate Γ_7 band has a higher energy than the fourfold degenerate Γ_8 band, according to [Mad12].

The direct electron transitions from the valence band to the conduction band take place without momentum change. In such systems a direct transition at the k = 0 symmetry point Γ is allowed. These systems are known as direct band gap semiconductors. A direct optical excitation with photons at $E_g = h\nu$ can occur.

In Copper-Halides compounds, the excitons are described as Wannier-Mott interactions [CST85]. The electron (e) and hole (h) are only weakly bound due to a strong

screening of the electrons in the valance band and thus separated by a number of inter-atomic spacing's. The single particle model is based on non-interacting "electrons and holes" (e-h) as the only elementary excitons. In a real crystal, the electrons (e)and the holes (h) are charged particles, they create an exciton via Coulomb interaction. As a bound "electron-hole" (e-h) pair, an exciton is analogous to a hydrogen-atom [KGFU74]. This has a correlated movement and an effective mass approximately equal to that of two particles moving with the effective mass of the valence and conduction band.

The exciton is considered as an unbound electron (e) with wave-vector (k_e) in the conduction band, thus a simple relation dispersion is described as:

$$E_e(k_e) \;=\; E_g + \frac{\hbar^2 k_e^2}{2m_e}, \tag{1.6}$$

where E_g is the band gap energy and (m_e) is the effective mass of the electron (e). In a similar way, an unbound hole (h) is described with wave-vector (k_h) in the valence band, as:

$$E_h(k_h) \;=\; \frac{\hbar^2 k_h^2}{2m_h}, \tag{1.7}$$

where (m_h) is the effective mass of the hole (h). The electron-hole interaction is described by an Hamiltonian as follows:

$$H \;=\; -\frac{\hbar^2}{2m_e^*}\bigtriangledown_e^2 - \frac{\hbar^2}{2m_h^*}\bigtriangledown_h^2 - \frac{e^2}{\varepsilon|r_e - r_h|}, \tag{1.8}$$

where (ε) represents the dielectric constant in the crystal. The electronic structure is governed by the relative importance of different terms which constitute the Hamiltonian and their contributions are: confinement potential, spin-orbit interaction, Coulomb and exchange interactions. An exciton is characterized by the exciton Bohr radius and this is described by:

$$a_B \;=\; \frac{\varepsilon\hbar^2}{\mu e^2} \;=\; \frac{\varepsilon m_0}{\mu}\cdot 0.53(\mathring{A}), \tag{1.9}$$

where $\frac{1}{\mu} = \frac{1}{m_e^*} + \frac{1}{m_h^*}$ and (μ) is the reduced "electron-hole" (e-h) pair mass. The Rydberg energy for an exciton is given in analogy to the hydrogen atom by:

$$R_y^* \;=\; \frac{e^2}{2\varepsilon a_B} \;=\; \frac{\mu e^4}{2\varepsilon\hbar^2} \;=\; \frac{\mu}{m_0\varepsilon^2}\cdot 13.6(eV), \tag{1.10}$$

The dispersion relation is described as:

$$E_n(K) \;=\; E_g - \frac{R_y^*}{n^2} + \frac{\hbar^2 K^2}{2M}, \tag{1.11}$$

where $M = m_e^* + m_h^*$ is center of mass, (K) is the wave vector and (n) represents the principal number. The Coulomb attraction between two opposite charges binds them

together forming an exciton. This quasiparticle can travel freely throughout in the lattice. The quantum confinement effects change the electronic properties in semiconductor nanocrystals [BK93, Wog97]. The exciton structure is commonly observed through low temperature absorption spectra [Ell57, GCSC90]. Photons with energy above the band gap are absorbed, generating free electrons and holes. The energy to create excitons is slightly less than the band gap energy to account for the exciton binding energy. The excitons are generally characterized by their size relative to the host lattice.

Due to the quantum confinement effect, the excitons are moved to higher energies, as can be observed in optical absorption spectra. The experimental evidence for the exciton confinement effect in all three dimension has been found. This effect is found for microcrystallites of CuCl embedded in a vitreous matrix [EE91]. This result lead to the theoretical concept introduced by A.L.Efros and Al.L.Efros. The quantum dots are considered to be spherical microcrystallites with infinite potential barriers at the crystalline boundary. A.L.Efros and Al.Efros proposed a classification of quantum confinement regions, taking into account the size of quantum dots (r) and the exciton Bohr radius (a_B). The quantum confinement effect depends on the ratio of the crystalline radius to the Bohr radius of electrons (e) and holes (e) and the "electron-hole" (e-h) pair [EE82]. In Effective-Mass-Approximation (EMA) model, it is considered that the electrons and holes have isotropic effective masses. Therefore, the electron properties are described in terms of a particle-in-a-box consideration. Comparing the average crystallite radius (r) to the exciton Bohr radius of bulk semiconductor a_B, three quantum confinement regimes can be distinguished. The Bohr radius reads as:

$$a_B \;=\; a_e + a_h, \tag{1.12}$$

where a_e, a_h are the Bohr radii of the electron (e) and hole (h), respectively.

Quantum confinement regimes

Considering the size of microcrystallites (r) and the Bohr radius a_B, quantum confinement effects in semiconductors microcystallites are divided in three regimes. These quantization regimes are:

(I) The strong confinement regime occurs when (r) $<<$ a_B. In the strong confinement regime the Coulomb term turns out to be small and can be ignored or treated as a perturbation and the uncorrelated motion of an electron and a hole may be considered as the first approximation.

In this case the electron (e) and the hole (h) can be thought of as confined independent particles. Thus, the excitons are not formed, and the size quantization of the electron and the hole is the dominant term in Hamiltonian. The energy and the momentum conservation laws result due to selection rules, thus the allowed optical transitions are the transitions which couple the electron and the hole with the same principal (n) and orbital quantum (l) numbers.

(II) The intermediate confinement regime occurs when: (r)$<<$ a_e, (r) $>>$ a_h and μ) can be replaced by the (m_e^*), thus the effective mass of the hole (h) is much bigger

compared to the electron (e) mass. Taking into account these conditions, the quantum confinement effect of hole (h) and electron (e) are different.

(III) The weak confinement regime is observed in the case when (r) >> a_B, that $a_B = a_e + a_h$. This regime is characterized by the Coulomb interaction. In Eq.1.8 the term which describes the Coulomb interaction is the dominant term in Hamiltonian. The exciton-center of mass motion is quantized. The lowest energy state corresponds to the exciton state whose energy is shifted to higher energies by confinement and the shift of the energy is proportional to $\left(\frac{1}{r^2}\right)$.

Excitons in CuCl

In the CuCl system, the excitons are well known to be of Wannier type [Wan37]. The excitons generated in the CuCl system appear in a diverse landscape of semiconductor materials. Since the excitons span many lattice sites, the complex two-body problem is simplified (EMA) model. Thus, it becomes a hydrogen-like problem with a Coulomb potential leading to the hydrogen series. The weak confinement regime occurs in a semiconductor like CuCl compounds when the (r) >> a_B, where the bulk exciton Bohr radii is $a_B \approx 8\ \mathring{A}$. Thus, in weak confinement regime the transitional degree of freedom of excitons are modified due to the size quantification of the excitons. The interaction of "electron-hole" (e-h) is described by a Hamiltonian, and the interaction is given by [Wog97]:

$$H = -\frac{\hbar^2}{2m_e^*}\nabla_e^2 - \frac{\hbar^2}{2m_h^*}\nabla_h^2 + V_{r_e}(r_e) + V_{r_h}(r_h). \tag{1.13}$$

The value V_{r_i} represents the potential of the localized electron or hole and r_e and r_h are their coordinates in the crystal. Two cases can be distinguished:

(I) $V_{r_i} \to \infty \Rightarrow |r_i\ ,| > r$,(i=e,h),

(II) $V_{r_i} = 0 \Rightarrow |r_i| < r$,(i=e,h)

From the optical selection rules, in the weak confinement regime just the mixing of states with $\Delta l = 0, 2, ..$ for transitions such as (s-s) and (p-f) are allowed. Further, the quantization of the exciton center of mass motion is introduced described by $M = m_e^* + m_h^*$. CuCl posseses a direct band gap with a simple structure. Special interest is focused on the 1s exciton in CuCl involving the transition between the lowest conduction Γ_6 and highest valence Γ_7 bands, commonly labeled as the Z_3 exciton. The $Z_{1,2}$ exciton $\Gamma_8 \to \Gamma_6$ is the second notable exciton. However, this appears only in absorption spectra and has no luminiscence signature. The electron-hole exchange interaction in the Z_3 exciton leads to splitting into a triplet state and an optically-inactive singlet state.

Optical transitions

In most semiconductors the absolute values of the hole effective mass (m_h) in different directions is considered to be different. Thus, in a complete description the complex strcture of the valence band has to be considered. Neglecting it, the kinetic energy of the hole (h) is described in form of the Luttinger Hamiltonian-relation [Lut56], which reads

in a spherical symmetry [BL73].

$$H = \frac{\gamma_1}{2m_0}[\hat{P}^2 - \frac{\mu}{9}(P^{(2)}J^{(2)})], \tag{1.14}$$

where J is the angular momentum operator, $P^{(2)}$ and $J^{(2)}$ are second rank operators, the (μ) is defined as $\mu = (\frac{6\gamma_3+4\gamma_2}{5\gamma_1})$ and the (γ_i) are the Luttinger parameters. The orbital angular momentum contains the number (l) but also the number (l+2) due to the fact that the states with $\Delta l = 0, 2, -2$ are coupled. The quantum number n for the single particle will be replaced by a quantum number $n^*(l, l+2)$ and characterizes the ground state and the excited state. The mixing of the valence band has an influence on the optical selection rules.

1.4.4 Growing process of the nanocrystals

Quantum dots or nanocrystal materials are grown using different techniques in environment or in the growing processes. Quantum dots or nanocrystals can be incorporated in a vitreous-matrix, in crystalline matrix or on a crystalline surface. The growth process occurs due to the phase separation in a supra-saturated solution. The growth process is controlled by the diffusion of ions in a dissolute matrix and can be performed in different temperature ranges. Obviously, in the growth process three different stages are included. Those stages are describes as: a nucleation phase, the normal growth process and a competitive growth.

(I) The nucleation stage is the first growing stage and small nuclei are formed. It is well known that in this stage the nucleation process starts.

(II) The normal growth stage represents the second stage in the growth process. The crystallites exhibit a mono-atomic growth and the total volume of semiconductor phase increases monotonically. At the end when the crystallites are large enough and the supersaturation is negligible, in this phase almost all ions are already incorporated and the surface tension becomes important.

(III) Ostwald ripening describes the final stage in the growth process. In this phase a mass transfer from the small particles to the larger ones is predicted.

The nucleation and growth processes are very slow in time. Those mechanisms can be observed performing optical measurements for which a conventional spectrometer can be used [VW26]. In the growth process a time dependence of the nucleation rate is defined. In the growth dynamics theory each stage is separately analyzed. They offer the possibility to obtain information for different experimental conditions. In the nucleation stage, the ionic concentration is considered to be constant. Nevertheless, the number of nuclei and the critical radius are controlled by the super-saturation mechanisms. In the Ostwald-ripening stage, the number of seeds increase linearly in time. In the growth process, temperature and time combination are considered to be important parameters, those offer the possibility to obtain nanocrystals with the same sizes.

In the case $T_{melt} < T_{growth}$, this stage provides a second treatment of the nanocrystals near to T_{melt}. A long annealing time T_{anneal} close to the melting temperature but less than the T_{melt} gives a sharper exciton line resonance. Since, the T_{melt} is size dependent a

fine annealing process is considered to be a size-selective procedure. The T_{anneal} should be chosen according to the mean radius ($\bar{r}$) of the nanocrystals embedded in the matrix. In the case of small nanocrysals and reduced thermal annealing temperature, a long thermal treatment will be necessary to obtain considerable effects. Usually, different methods used to incorporate micro-crystallites in the matrix will have an inevitable influence on the size distribution of nanocrystals.

1.4.5 The CuCl:NaCl system. Optical properties

Reducing the dimension from bulk over two-dimensional quantum wells and one-dimensional wires to zero-dimensional quantum dots is an ongoing trend in semiconductor physics and technology. The emphasis is usually focused on the electronic properties of those structures. Semiconductor nanocrystals can be embedded in vitreous or crystalline matrices and the investigation of the resulting semiconductor nanocrystals is imporant in solid state physics [Yof93, BK93, Wog97].

The NaCl and CuCl compounds show the phase diagram of an eutecticum system [Sad14]. They have different structures, the one for NaCl is rock-salt type and the one for CuCl is zinc-blende structure. In a strict sense, the thermodynamically driven phase separation should produce a mixture of two crystals such as NaCl + Cu^+ and CuCl + Na^+. Therefore, CuCl:NaCl shows on the NaCl rich side a strong tendency for a local supersaturation of copper during cooling down to room temperature. These spots of enriched CuCl content are sources for the nucleation of CuCl seeds and finally they form nanocrystals.

Obviously, the existence of nanocrystals indicates the absence of a final thermodynamic equilibrium. On the other hand, the nanocrystals show a good local stability after some time of ripening. Nevertheless, different states of a sample with respect to the existence or nonexistence of the nanocrystals can be used to identify several anomalous effects.

In the CuCl:NaCl system, the nucleation processes of CuCl nanocrystals in a NaCl matrix require only the diffusion of a small amount of cations Cu^+, whereas the anions Cl^- remain in the same state of the homogeneous mixed crystal [SSVdO93]. Experimental results obtained by Two-Photon Spectroscopy show that CuCl nanocrystals have a pronunced orientation. Thus, the crystal axes of the CuCl nanocrystals and the NaCl matrix are found to be parallel oriented to each other [FHR95].

The CuCl:NaCl system has been described by Sadonnini [Sad14], he reported the phase diagram for the first time in this system. The research of the CuCl:NaCl system continued and later optical absorption experiments with a relatively small amount of CuCl in UV range and at room temperature were performed [Sma27]. The experimental results illustrate a band absorption close to 255 nm. Additionaly investigations of CuCl:NaCl were continuously performed, varying the thermal conditions in CuCl:NaCl. Two resonance lines were detected at 380 nm and 250 nm [Mah29].

As the nanocrytal structure forms, CuCl nanocrystals were first embedded in a vitreous matrix and those structures were analysed performing absorption and luminescence experiments [EEO85]. The quantum confinement effect in CuCl nanocrystals attracts special interest in the case of a crystalline matrix. CuCl nanocrystals were embedded in NaCl matrix. The size and shape of CuCl nanocrystals were investigated by Small Angle

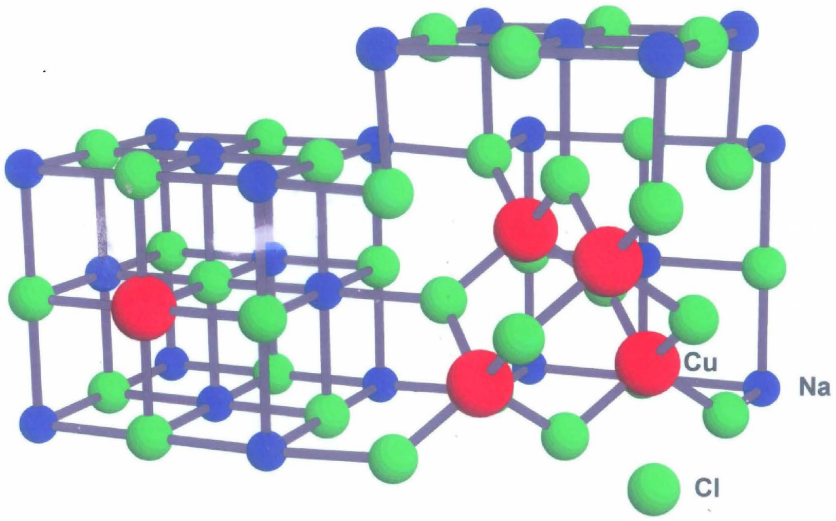

Figure 1.9: Illustration of the CuCl:NaCl structure: blue spheres represent Na^+ atom, green spheres represent Cl^- atom and red spheres represent Cu^+ atom. In the right side CuCl interpenetrated in a NaCl structure is shown.

X-ray Scattering [IIK88, UIN65]. It explained the broadening of absorption bands which are shifted to higher photon energies compared to bulk material. Obviously, the exciton states are expected to be influenced by the quantum size effect [EE82].

In further research of CuCl nanocrystals embedded in a NaCl matrix, the interaction between the nanocrystals and the matrix was considered[WSPV04, WKLPV05]. Resonant Ulrasound Spectroscopy experiments combined with exciton spectroscopy and X-ray diffraction methods described CuCl nanocrystals as internal sources of stress [WKLPV05]. Near Field Scanning Optic Microscope (SNOM) and Atomic Force Microscope (AFM) were experimental techniques used to scan the deformation field of CuCl nanocrystals caused by the lattice misfit [DHRW98, Ro94].

Exciton spectrum of CuCl:NaCl. Determination of CuCl nanocrystal size

The exciton spectrum of the Cu^+-halides can be interpreted along the same lines as the absorption edge of other materials with wurtzite and zinc-blend structure type. The excitons in CuCl are formed by an electron in the lowest conduction band Γ_6 symmetry and a hole either in the upmost twofold-degenerate Γ_7 symmetry (Z_3 excitons) valence band or in the fourfold degenerate Γ_8 symmetry ($Z_{1,2}$ excitons) [Car63]. The valence band has $Cu3d^+$ character [KGFU74]. The fourfold degeneracy of Γ_8 leads to a complicate quantitative treatment of the confinement effects. Therefore, the Z_3 exciton resonance line corresponding to Γ_7 symmetry is more suitable to investigate CuCl nanocrystals embedded in a

NaCl matrix. Since, the CuCl has a large exciton binding energy of $E_b = 190\,\text{meV}$ [Kli01]. Therefor, the distance between the first two lines in the exciton series is rather large and they do not overlap [LB89].

Table 1.3: Parameters of CuCl at T = 78 K

Chemical Formula	**CuCl**
Exciton Bohr Radius–$a_B[\text{Å}]$	5.8 [LB89]
Exciton energy–**E [eV]**	$Z_3 = 3.218$ [GRC$^+$98] and $Z_{12} = 3.283$ [Kli01]
Spin orbit splitting–ΔE **[meV]**	65 [LB89]

The two exciton resonance lines Z_3 (Γ_7 symmetry) and $Z_{1,2}$ (Γ_7 symmetry) in bulk CuCl are observed also in doped NaCl, the only difference is that those absorption bands are shifted to higher photon energies. The exciton resonance lines of CuCl nanocrystals are strongly dependent on temperature and the size of the nanocrystals. A small size effect of the nanocrystals produces a shift of the resonance lines towards higher photon energies, this is the common blue-shift due to spatial confinement. The dependence of the exciton energies for the Z_3 and $Z_{1,2}$ excitons on the mean radius of quantum dots are described below. The energy for the lowest state (n = 1, m = 1 and l = 1) can be described as [EE82]:

$$\hbar\omega_{Z_3} \;=\; E_3 \;=\; E_g - E_b + \left(\frac{0,67\hbar^2\pi^2}{2Mr^2}\right), \tag{1.15}$$

where the (r) represents the mean radius of the nanocrystals embedded in the matrix, E_g describes the band gap, E_b describes the binding energy in bulk material and the $M = 2,3 \cdot m_0$ [IIK88]. The lowest-energy state is idenitified by its shift to higher energies by confinement scaling with $(\frac{1}{r^2})$.

The size dependence of the nanocrystal resonance line $Z_{1,2}$ needs a more adequate and complex descriptions compared to the Z_3 expression. In the CuCl:NaCl system, the mean radius r of CuCl nanocrystals is larger compared to the Bohr radius. Thus, the shift ΔE in energy of the ground-state exciton is described by [EE82]:

$$\Delta E(r) \;=\; \left(\frac{\hbar^2\pi^2}{2Mr^2}\right), \tag{1.16}$$

where (M) represents the mass of the exciton given by $M = m_e^* + m_h^*$, with (m_e^*) and (m_h^*) being the effective masses of electron (e) and hole (h), respectively.

A statistical distribution of the nanocrystals in the system leads to variations in the position of the exciton lines and widths. The physical origin of the broadening in the absorption spectra is due to dephasing which occurs within a single quantum dot, through scattering of the optically generated electron-hole pair with impurities, photons or through the radiative pair recombination.

These processes produce the effect of the homogeneous broadening. The optical absorption spectra contain, additionally to homogeneous broadening, the inhomogeneous broadening [KK71, Baj74]. Thus, the inhomogeneous broadening effect reflects the statistical distribution of the nanocrytals in the matrix. Within the material one finds quantum dots with different sizes. Each quantum dot or nanocrystal size contributes to the total absorption with a weight, which is given by the probability to find this particular size in the sample.

Short review of CuCl optical absorption experiments

In absorption spectra of CuCl the signatures of the Z_3 and $Z_{1,2}$ exciton peaks are observed and those are followed by a flat absorption up to 6 eV [Fus69]. A difference in the exciton spectra of CuCl and other copper-halides is observed. All, of them have an inverted order of Z_3 and $Z_{1,2}$ as compared to CuCl. The peak position inversion describes the strong Γ-point d-mixture at the upper valence band.

Optical experiments performed on CuCl films deposited on different substrates and (micro)crystals shown that the values at which the Z_3 and $Z_{1,2}$ exciton lines are detected have approximately the same value. The optical absorption spectra obtained on a CuCl film reflect measurements on single crystals. Kaifu et al. determined the exciton spectra and the temperature dependence on CuCl films, they used a Kramers-Kronig analysis of reflection measurements on single crystals [KK71]

A large absorption coefficient, usually, leads to experimentals inaccuracies. In the case of high quality samples and sufficient energy resolution the exciton fine structure can be determined. In addition to the lowest energy state (n = 1) of the Z_3 exciton, peaks corresponding to the (n = 2) and (n = 3) lines of a hydrogen-like series are found. From this structure the binding energy and the band gap were determined [Gol77].

1.5 Phase transition B1 → B2 in KCl under pressure

For a number of alkali halides, the phase transitions from the B1 phase (NaCl-structure) to a denser B2 phase (CsCl-structure) is a typical rebuilding behavior [CG75, PLR$^+$94]. In general, at zero external pressure the B1 phase is considered to be a stable structure. Then, when the point of polymorphic transformation is reached, the B2 phase occurs. The polymorphic transformation is a characteristic structural change in the atomic coordinatios. Thus, it occurs at moderate pressure when the solid becomes unstable under given thermodynamic conditions. In several materials, the phase transition was studied [Bri40, Bri45, VBPK73]. Therefore, in a more limited sense the expression "structural-phase-transition" is used for changes which can be described by well defined geometrical paths. Atoms change their crystallographic position during a phase transition.

Under pressure, the inter-atomic distances are reduced and the forces between atoms are changed. As a consequence the Gibbs free energy of the atomic arrangement is changed. An increase of pressure will lead to an increase of the Gibbs free energy of the stable atomic arrangement of a material in phase B_1. A specific atomic arrangement in phase B_2 (CsCl structure in KCl material) can exist with a small Gibbs free energy at a well defined pressure. At high pressure, the atomic arrangement becomes unstable compared to the new atomic arrangement in phase B_2. Thus, a new phase becomes favorable for the system. Thus, a change in atomic arrangement follows in order to minimize the Gibbs free energy at those conditions. The existence of the new phase B_2 is accompanied by an increase of the density in the material. Usually, the structural phase transition which appears under pressure is of first-order [KKT06].

However, a phase transition to the CsCl structure is predicted [BRB97, RFF$^+$02].

Table 1.4: First order phase transitions under pressure in KCl from B_1 to B_2.

p_{tr} **[GPa]**	literature-experimental methods
1.97	[Bri45]–under static compression
2	[Hay74]–stress gauge (100), (110)
1.89	[DPP65]–gauge method
2.5 ; 2.2; 2.1	[MNT$^+$02]–phase transition along (100); (110); (111)

In an atomic arrangement, the cations have smaller sizes compared to the anion sizes. For example, the sodium chloride crystals have a B_1 structure where the chloride ion size is $r_{Cl^-} = 1.81$ $\mathring{A}$ [SSS13] is almost twice that of the sodium ions $r_{Na^+} = 0.98$ $\mathring{A}$ [Zac31]. In KCl, the values of the ionic radii were reported as $r_{K^+} = 1.57$ $\mathring{A}$ [MI67] and $r_{Cl^-} = 1.67$ [SSS13], as determined by X-ray diffraction measurements. Compared to the theoretical results, the ionic radii are found to be: $r_{K^+} = 1.617$ $\mathring{A}$ [Sys69] and $r_{Cl^-} = 1.81\,\mathring{A}$ [Sha76].

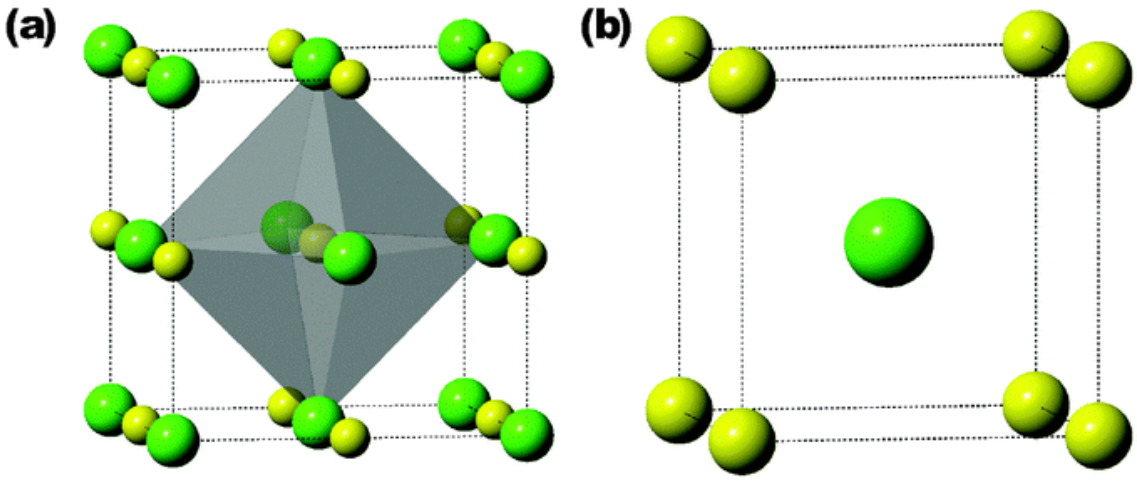

Figure 1.10: Conventional unit cell of KCl.(a) B1 (rock-salt) Cl atoms are green and K atoms are yellow. The gray polyhedron in (a) outlines the octahedral arrangement of K around a central Cl.(b) B2 (CsCl) KCl structure. K atoms are green and Cl atoms are yellow.

The cations have a larger size compared to anions to be included in the voids. Thus, the cations move relative to the anions and the atomic packing is loose. In these conditions, the free space of NaCl or KCl (A^+B^--compounds) is too small to insert one or more ions. Thus, the ratio of ionic-radius $\left(\frac{r_{B^-}}{r_{A^+}}\right)$ defines the type of ionic structure. If the ratio values is changed due to external parameters such as temperature, pressure etc, the crystalline structure in the ionic compound changes.

The polymorphic phase transition in crystals can be investigated by experimental techniques or theoretical ab inito models. One of these methods represents Desity-Functional-Theory (DFT). This method is used to investigate the properties of many-particle systems. The DFT method works by minimizing the thermodynamic potential and determining the inter-ionic distance at a given external pressure. Thus, DFT can study the features of phase transitions in ionic crystals under pressure. As long as the external pressure is lower than the polymorphic transition, the B_1 phase (NaCl-structure) is more stable, since $\Delta G > 0$. In the vicinity of the phase transition point $\Delta G \approx 0$ both phases are in equilibrium. As the external pressure becomes higher than the polymorphic transition pressure $\Delta G < 0$, and B_2 phase becomes stable [KKT06].

The Molecular Dynamics (MD) method is applied to investigate the phase transition from $B1$ to $B2$, considering ab inito calculations. In KCl, the B2 phase is predicted at 3.5 MPa by the MD method [KMK05, Ove62, And66]. The MD method is applied taking into account that the phase transition is generated through displacements of the atomic lines parallel with the (100) axis of $B1$ and these lines are parallel with the (110) axis directions of $B2$. Thereby an explanation from B1 to B2 can be given. Thus, the phase

transition starts around the dislocations and the phase transitions pressure decreases as regards dislocations.

Another method to investigate the B1 $\rightarrow$ B2 phase transition in ionic compounds is the Pseudo-potential approach. This approach addresses the structural properties during the phase transitions including their electronic properties. It is used to study the structural energies and gives information about internal pressure and stress. Increasing the pressure, the new phase B2 appears and the energy gap positions change as well as the gap increases by increasing pressure.

The dependence of the elastic coefficients on hydrostatic pressure is very important due to the relationship between stress and strain increments. The elastic coefficients provide information about the nature of the bonding between adjacent atomic planes and the anisotropic character of the bonding and the structural stability.

Chapter 2

Experimental Techniques

2.1 Characterization of CuCl:NaCl

CuCl:NaCl is an eutectic system which permits the preparation of single crystals of NaCl with embedded CuCl nanocrystals. The eutectic temperature was found to be $T_e \approx 600\,\mathrm{K}$ [HW98]. CuCl nanocrystals nucleate in a NaCl matrix as a consequence of a thermodynamically driven phase separation. In the CuCl:NaCl system, the major constituent-NaCl represents the dielectric matrix or the host material and the minor constituent-CuCl represents the embedded semiconductor nanocrystals. The corresponding crystallographic structures are described in Table 2.1. In the nucleation process of CuCl nanocrystals in the NaCl matrix only the diffusion of a small amount of Cu^+ ions is needed whereas the Cl^- anions of the sub-lattices remain in the state of a homogeneous face-centered cubic (f.c.c) sub-structure.

CuCl:NaCl crystals were grown by the Czochralski method and the concentration of CuCl in the melt was varied between 0.8% and 3.5%. The difference between the lattice parameters of both sub-structures generate a gap between the nanocrystals and the matrix. Nevertheless, this space or gap can be closed due to internal forces developed between the nanocrystal and the matrix [WSPV04, WKLPV05]. In general, the internal forces cannot be directly measured. An essential problem in CuCl:NaCl system is to find out the residual stress due to elastic interaction between the nanocrystals and the matrix. An important aim is to find out in which way the existence of the embedded nanocrystals are able to elucidate these problems.

Table 2.1: Structure parameters of CuCl, NaCl and KCl compounds. p_{tr} represents the pressure for the new phase B2, a represents the lattice parameter and T_m represents the melting temperature.

Molecular formula	**Structure-B1**	p_{tr} $[GPa]$	**Struture-B2**	a$[\mathring{A}]$	$T_m[^\circ$ C]
CuCl	zinc-blende	10 [BCC86]	NaCl	5.416 [LB89]	430
NaCl	rock-salt	30 [Bas68]	CsCl	5.64012 [LB89]	801
KCl	rock-salt	1.93 [VBPK73]	CsCl	6.2931 [LB89]	770

2.2 Exciton Spectroscopy

The radiation interacts with matter, and different processes can occur in material: reflection, scattering, absorbency, absorption and re-emission. When a beam of light propagates through a sample which has the ability to interact with the electromagnetic radiation, part of the radiation is absorbed by the sample and the rest of it is transmitted through the sample. In the Exciton Spectroscopy method, the unoccupied electronic states of the sample will be populated via transitions between the valence band and the conduction band.

If a specimen is irradiated with a continuous spectrum of light with intensity I_0, a part of it is reflected and a part is absorbed by the sample. The transmitted light of intensity I depends on the absorption coefficient α, the thickness of the sample (d), and the wavelength (λ) of the incident beam. The relation between the incident intensity beam and the transmitted light of the sample, I_0 and I, is given by:

$$\left(\frac{I}{I_0}\right) \;=\; e^{(-\alpha \cdot d)}. \tag{2.1}$$

In Section: [3.3, 3.4 and 3.7] the CuCl:NaCl system has been investigated performing optical absorption measurements. The optical properties in this system are used to explain different effects regarding the elastic interaction between nanocrystals and matrix. The optical spectra were recorded in the Ultra-Violet (UV) and Visible (VIS) ranges. The spectrum resolves the excitonic or inter-band transitions from valence band to conduction band. The optical absorption spectra contain a lot of information about the amount of CuCl in NaCl in crystalline form and noncrystalline form as Cu^+ ions. The size of the nanocrystals can be determined from the central position of the resonance lines, usually, the resonance lines at low temperature are well resolved.

The optical absorption measurements were carried out using a standard Spectrometer Cary–2300 from Varian. The spectrometer is able to record the optical absorption spectrum in the (UV), (VIS) and (NIR) Near-Infra-Red ranges. Optical absorption spectra were recorded between 200 nm and 460 nm.

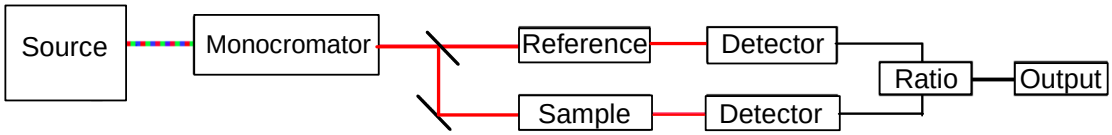

Figure 2.1: Schematic diagram of a double–beam UV-VIS Spectrophotometer.

The spectrometer uses in the wavelength rang $\lambda < 340\,\text{nm}$ a Deuterium lamp as light source and for $\lambda \geq 340\,\text{nm}$ an incandescent lamp. The maximal scan resolution is 0.04 nm. Usually, the optical measurements were performed as a function of temperature between 20 K and 550 K. The Cary 2300 is able to work with two different cryostate systems. A closed helium cycle machine was used between room temperature and about 573 K. The second cryostat working with a controlled flow of liquid nitrogen between 72 K and 800 K. The experimental spectra were collected by an external computer.

2.3 X-ray diffraction technique

In a general sense, X-rays are considered to be a part of the electromagnetic spectrum with photons of suitable short wavelength. A crystal can be used as a three-dimensional diffraction grating for X-rays. The X-ray diffraction phenomenon is applied in a crystalline structure to get structural information. X-ray diffraction is a highly sensitive method compared with another technique used for revealing information on the crystallographic structure of a material as well as the chemical and physical properties.

This method exploits constructive interference of the beams diffracted by the crystal satisfying the Bragg's Law. X-ray waves are considered as being reflected by sheets of atoms in the crystal. When a beam of monchromatic X-rays strikes a crystal, the waves scattered by the atoms in different sheet combine to form a reflected wave. If the path difference for waves reflected by successive sheets is an integer multiple of the wavelength, the waves will combine to produce a strong reflected beam. Bragg expressed this in an equation well known as Bragg' Law or Bragg condition, it's given by:

$$2d\sin\theta \;=\; n\lambda, \tag{2.2}$$

where (n) is an integer number for constructive interference, (θ) is the angle between the incident rays and the surface of the crystal and (λ) is the wavelength of the X-rays. Figure 2.2 shows the X-ray diffraction mechanisms. This is described as an incident wave which is directed onto a material and a detector is typically moved about to record the directions and intensities of the outgoing diffracted waves, the incident wave must have a wavelength comparable to the spacing between atoms. A diffraction pattern from a material typically contains many distinct peaks, each corresponding to a different interplanar spacing (d). If the sample contains multiple phases there can be ambiguity in assigning a diffraction peak to a specific diffraction pattern, and an overlap of peaks from different patterns may occur.

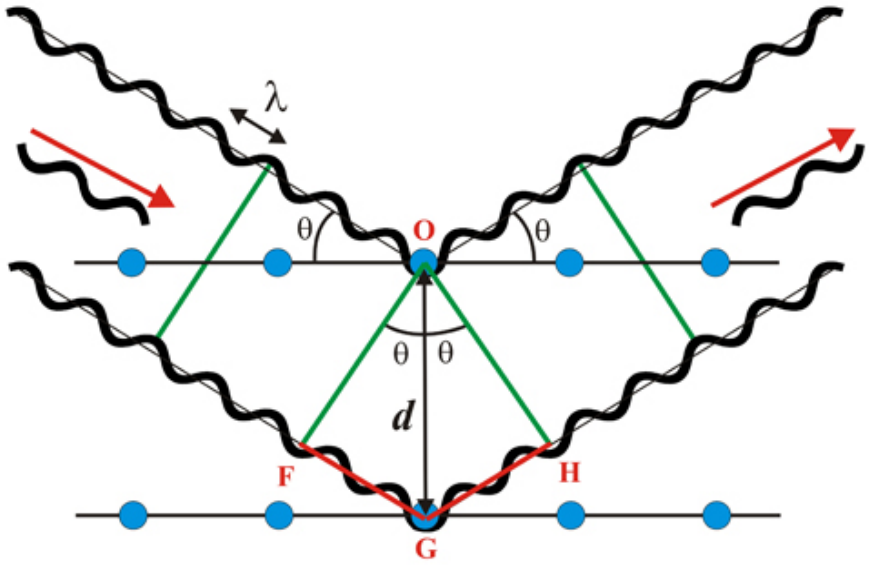

Figure 2.2: Geometry for interference of wave scattered from several atomic planes separated by the spacing d.

The diffractograms contain information about structure of material in encrypted form. The positions and intensities of diffraction peaks contain information about the ideal crystal structure. The atomic structure of crystals can be deduced from the directions and intensities of the diffracted X-rays beam. A crystal is built of unit cells which are regularly arranged in three dimensions. The X-ray beam depends on the distance of the unit cells, and the strength of the diffracted beam depends on the arrangement of the atoms in each unit cell. In X-ray powder diffraction peak profiles, usually a broadening appears. The sources of peak broadening are well known to be due to instrumental broadening, the finite crystalline size, extended defects and strain. The strain can produce two effects in the peak convolution: a shift in the peak positions due to an uniform strain effect and a broadening due to an nonuniform strain. The width of a diffraction peak is affected by the number of crystallographic planes which are involved in the diffraction process. As crystallites became larger, the diffraction peaks became sharper in (θ)-angle.

In X-ray diffraction experiments, the intensity of the diffracted beam is continuously recorded as the sample and detector are rotated through their respective angles. Results are commonly presented as peak position at (2θ), the intensity I is either reported as peak height intensity above background or as integrated intensity, i.e. the area under the peak. Obviously, the most important information from a diffraction spectra are obtained from the peak central peak position, the peak intensity and the linewidth. The Full Width of Half Maximum (FWHM) of the reflected peaks is important to study the stored strain in specimens. The diffracted X-ray intensity peaks can be fitted with a Gauss function, a

Lorentz function or a pseudo-Voigt function.

2.3.1 Beamline 9 Delta-Dortmund

The experiment reported in Subsection: [3.1.2-3.1.3] has been performed at the beam line BL9 of the Dortmunder Elektronen Speicherring-Anlage DELTA at Dortmund University [KPS+06]. The experimental setup described in Fig. 2.3 is used for measurements in materials such as powder, single crystal or liquids form.

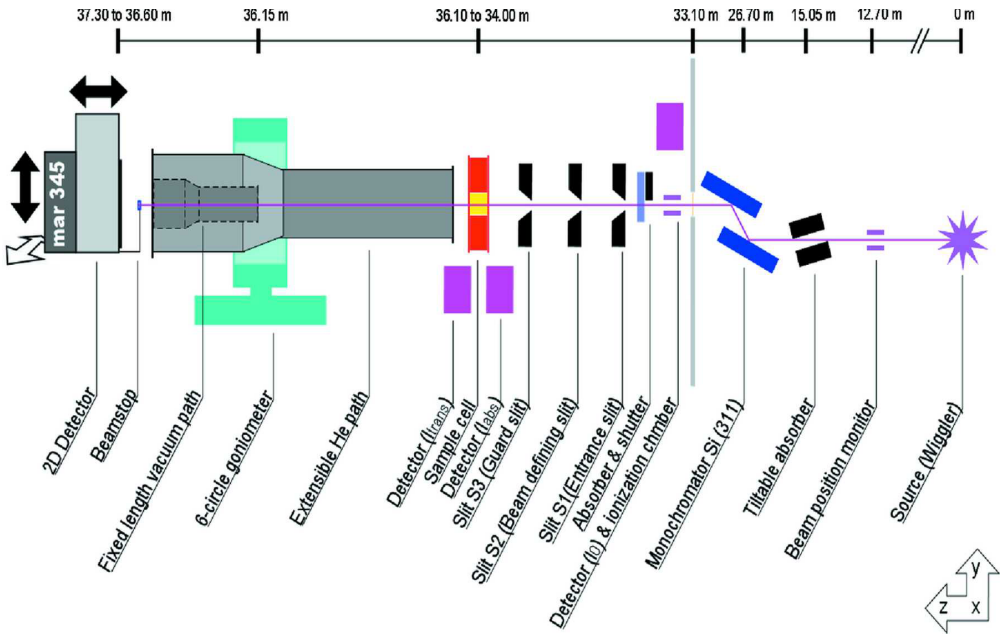

Figure 2.3: Schematic set-up on BL9 of DELTA, according to[KPS+06].

The Electron Accelerator at BL9 is equipped with a Huber six-circle diffractometer(see Fig. 2.3). The storage ring is able to work at a maximum energy of 1.5 GeV with an electron beam of 120 mA and a life time of ~ 10 h. At BL9 the incident beam is monochromatized by a double monochromator with an energy resolution ($\frac{\Delta E}{E} \simeq 10^{-4}$). The monochromator provides synchrotron radiation between 4 keV and 30 keV. All measurements were carried out at 25° C room temperature and at least six Bragg reflexes between (100) and (820) have been recorded. To avoid texture effects, the experimental samples were rotated about the axis perpendicular to the incident beam.

2.3.2 Beam line B1-HasyLab Hamburg

The MAX 80 system of the Geo Forschung Zetrum Postdam is a typical cubic-anvil pressure apparatus with six tungsten carbide anvils compressing a cubic sample volume. A Multi-Anvil X-ray device is used to investigate the stability of minerals under pressure and

temperature. Obviously, the bulk moduli, thermal expansion and phase transitions of materials, pressure and temperature of the kinetics phase transitions can be determined. The external pressure is generated by a 250-tons hydraulic ram. The experiment can be performed applying additional to external pressure a temperature regime. The temperature is generated by an internal graphite heater and it is controlled by a thermo-couple.

The internal pressure is mainly determined by a sample used as a reference sample. The experiment described in Section:3.6 has been performed at BL B1-HASYLAB in order to improve the internal pressure filled by grains and the phase transitions in KCl material. The Synchrotron beam is guided between the tungsten anvils through the sample. A Ge solid state detector with a resolution of 135 eV for 6.3 keV and 450 eV for 122 keV detects the diffracted beam at a fixed angle. Notice, that in our experiments the energetic limits are improved. The MAX 80 device can be adjusted in 3 directions: vertical, rotational and horizontal movements perpendicular to the synchrotron beam with an accuracy of 10 μm. The size of the primary beam and the diffraction beam are controlled by a stepper-motor driven crossed-slit system.

Within the experimental configuration, the orientation of the incoming X-ray beam and the scattering angle are fixed. The peak reflections are observed just for the grains which match the incoming beam and the detector positions. A variety of diamond-anvil cells based on the simple principle of applying a moderate force to the relatively large surface area and this force is transferred to six diamond-anvils was used. It is very important to perform high-pressure diffraction experiments under well-defined conditions of applied stress. Thus, this means that a hydrostatic pressure medium must be used to enclose the crystal.

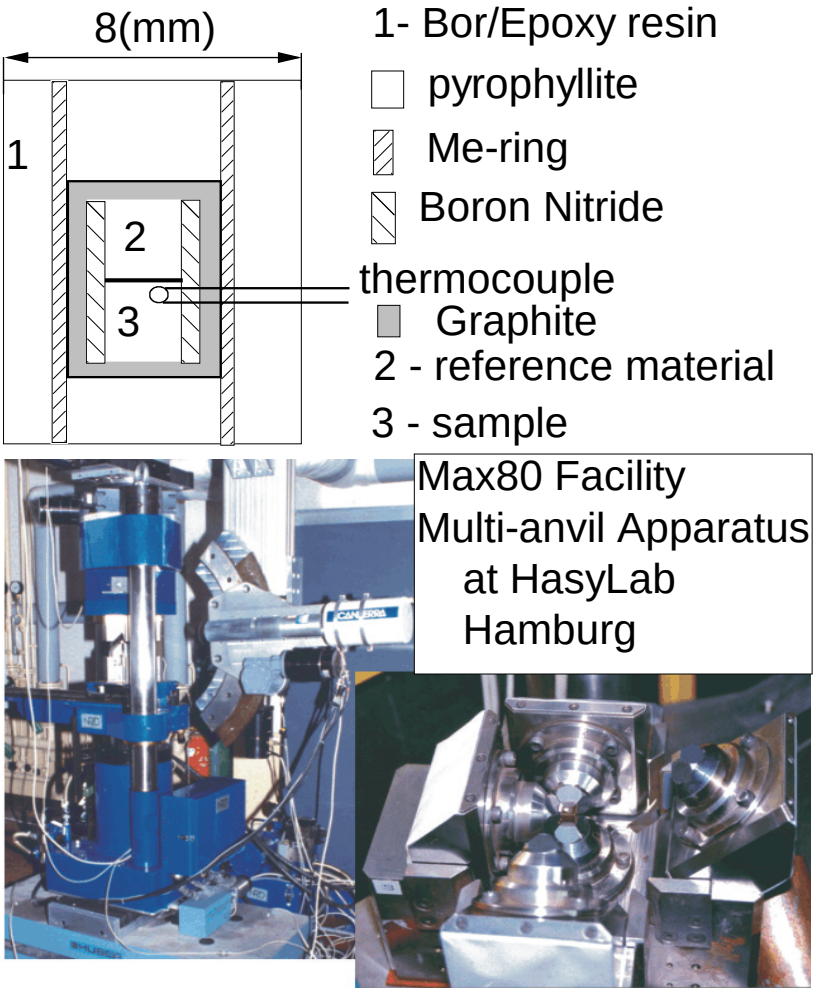

Figure 2.4: Typical sample fitting in the Max 80 Multi-Anvil System, according to [Oht07].

2.3.3 Powder sample preparation

A well known method to prepare powder from single-crystals is the so-called ball-milling method. This method is a method where the size of the grains depends of the milling time [UGRB01]. In our X-ray diffraction experiments, the experimental samples were prepared by the classical so-called "pestle-in-the-mortar" method. This method includes rather complex processes which can be decomposed into several stages. In the first stage, the pulverizing process starts with an uniaxial pressure along the vertical direction and additional torsional forces around the vertical axis produce shear stress. Practically, the particular feature of this process is the activation of different types of glide systems and of fracture mechanismus [JKL24]. The torsional forces produce a shear stress which activates

gliding along the (001) plane. The same torsional forces activate the (001) plane, which results in the failure process. The size of the grains is about 20 μm if the pulverizing time was approximately 5 minutes and their sizes were measured by a microscope. The pulverization procedures together with the measurement of stored strains can be used as a test for the existence of embedded nanocrystals in material.

The glide systems in NaCl are $\{110\}\ \langle 110\rangle$ [JKL24, Bue30]; $\{100\}\ \langle 110\rangle$ [Dom34, Bue30] and $\{111\}\ \langle 110\rangle$ [Dom34, Hes65]. Easy gliding occurs on a (110) plane corresponding to a combination of plane and direction. In contrast to standard creep experiments this kind of pulverizing has the particular feature that two different types of glide systems can be activated simultaneously.

2.4 Optical Birefringence technique

The birefringence phenomenon is defined as a double refraction of light in a transparent material. Thus, this phenomenon is described by the existence of orientation-dependent differences in the refractive index. The optical birefringence measurements are used in the present work for detecting the internal sources of stresses in pure and doped NaCl. Due to these measurements it is possible to detect structural changes in a material with high sensitivity. The sensitivity of birefringence measurements is several orders of magnitude higher compared to X-ray diffraction technique [Web95].

The birefringence experiment is described in Section: 3.2 for pure NaCl and CuCl:NaCl crystals for which a standard experimental set-up illustrated in Fig. 2.5 was used. The doped NaCl crystals show all the macroscopic properties of a large single crystal, however, due to the low doping chemical contamination the CuCl:NaCl crystal can be compared with a pure NaCl single crystal.

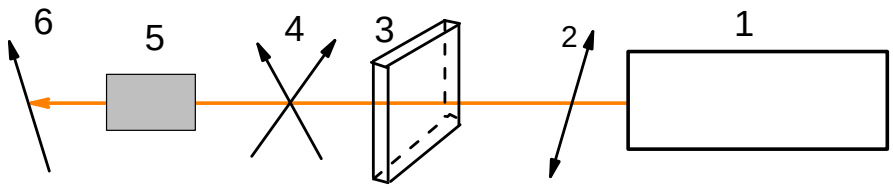

Figure 2.5: Sketch of the experimental set-up used in the optical birefringence experiment. Optical components are described as: 1-[He-Ne] laser, 2-polarize, 3-sample, 4-compensatory, 5-Faraday Cell and 6-analyzer.

2.5 Resonant Ultrasound Spectroscopy—RUS

Resonant-Ultrasound-Spectroscopy (RUS) is a highly sensitive technique, used to study the mechanical resonance in the crystals. RUS is a method based on the measurement of the vibrational eigenmodes of the samples. The experimental sample has a well defined shape, usually, a regular shape such as a parallelepiped. A typical arrangement used in

the RUS technique is illustrated in Fig. 2.6. The specimen is fixed lightly between two transducers as illustrated in Fig. 2.6. The drive transducer is used to excite the sample and the pickup transducer serves as a detector. In order to measure the resonant response, the frequency of the first transducer is swept through a frequency range corresponding to a large number of vibrational eigenmodes of the sample. The resonant response is recorded by the second transducer-pickup transducer. In Section: [3.7] a RUS experiment performed on two different samples of doped NaCl in order to investigate their elastic properties is described.

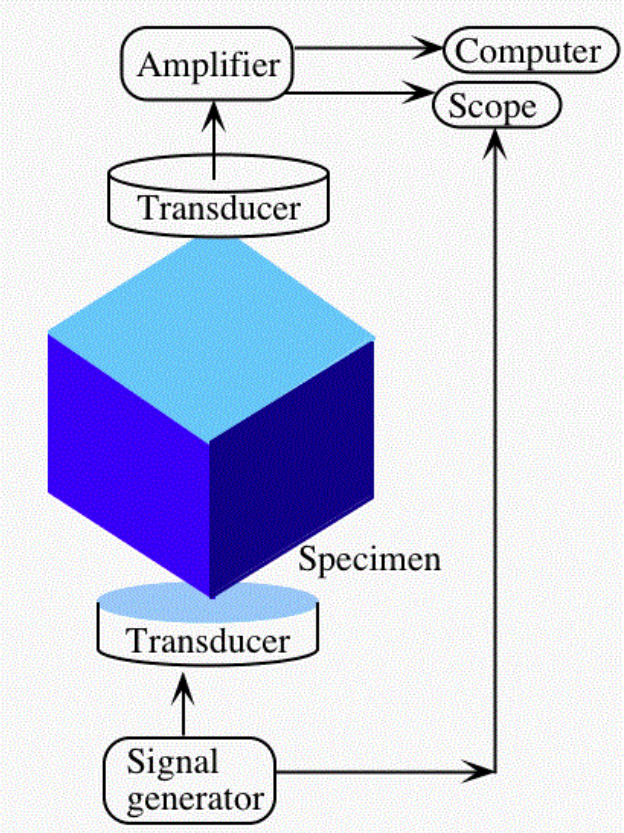

Figure 2.6: Sample-transducers arrangement for RUS experiments, according to [LW97].

Chapter 3

Experimental Results

3.1 The influence of dislocations

Considering different experimental results describing the elastic interaction between matrix and embedded nanocrystals a new idea has appeared. The central aim is to confront CuCl nanocrystals embedded in NaCl with plastic processes of the matrix[HW98]. Searching in the literature for a suitable experimental technique to probe the essential mechanisms of plastic flow in alkali-halide crystals the following hint was found in an old paper. When Straumanis improved the Debye-Scherrer technique to determine lattice parameters as exact as possible he recognized that, when NaCl was used, the film camera recorded narrow reflection lines only if the powder was annealed at high temperatures to remove the induced strains[SI38]. Most likely he pulverized the material in the traditional way by pestle in a mortar. The reported strong broadening motivated us to analyze this process of pulverization. It was found that the pulverizing by a pestle in a mortar yielded some surprisingly clear results which differ from previous observations in alkali-halides. The rupture of a material is related to elastic deformations, plastic flow, yielding, work hardening, solution strengthening, movement and multiplication of dislocation.

3.1.1 Uniaxial stress effect

Plastic properties of a crystalline material are most reliably measured on single crystals of macroscopic size. Two samples with a parallelepiped shape were prepared with [100] edge directions. The first one consists of pure NaCl and the second one of CuCl:NaCl. The uniaxial experiment was performed in order to study the dislocation effect in pure and doped NaCl. The samples used in the uniaxial experiment are illustrated in Table 3.1. An uniaxial compressive pressure is loaded along the longest edges (l_3) in several steps with increasing weights. The external stress was removed after a weight had been rested on a sample for 15 minutes. The length of the sample was measured with high sensitivity after each loading and deloading. In addition the occurrence of persisting birefringent bands was tested up to a final maximal loading of 3.5 MPa.

After each loading step, the samples were inspected under a polarization microscope.

Table 3.1: Characterization of samples prepared from pure and doped NaCl crystals. The length of the edges are noted as l_i

Sample	$l_1[mm]$	$l_2[mm]$	$l_3[mm]$
NaCl-pure	3.55	3.79	15.97
CuCl:NaCl	3.60	3.77	13.94

Figure 3.1: Crystal: (left side) pure NaCl, (right side) CuCl:NaCl, between crossed Nicol prisms after uniaxial pressure along [010]. The variation of light intensity in pure $NaCl$ corresponds to birefrigent bands along [110] and [1$\bar{1}$0] which had been written-in by the uniaxial pressure.

The faces perpendicular to the pressure were observed by a polarization microscope to detect birefringent bands as a consequence of plastic flow and the appearance of micro-cracks that indicate the failure of the material. The uniaxial experiment accomplished in pure NaCl shows the typical birefringence bands illustrated on the left side in Fig. 3.1. The birefringent bands are induced by the shear strain compounds of the applied stress. The transmitted optical waves were linearly polarized parallel to [100] or [010].

Figure 3.1 demonstrates a different plastic behavior of pure and doped NaCl. Only in the pure material the birefringence bands are stored. Thus, this stored effect most likely stems from arrested edge dislocations. The appearance of birefringence in the pure material and its absence in the contaminated material must be considered as a strong anomaly in the field of crystal growth and needs further studies.

The stress-strain curves were obtained by the uniaxial pressure on large single crystals. There are illustrated in Fig. 3.2. T_{cr} represents the elastic limit. In ductile materials, the T_{cr} may be identified with the yield point or critical resolved shear stress. T_f represents the stress at which the atomic bonds break permanently. In brittle materials T_f is near to

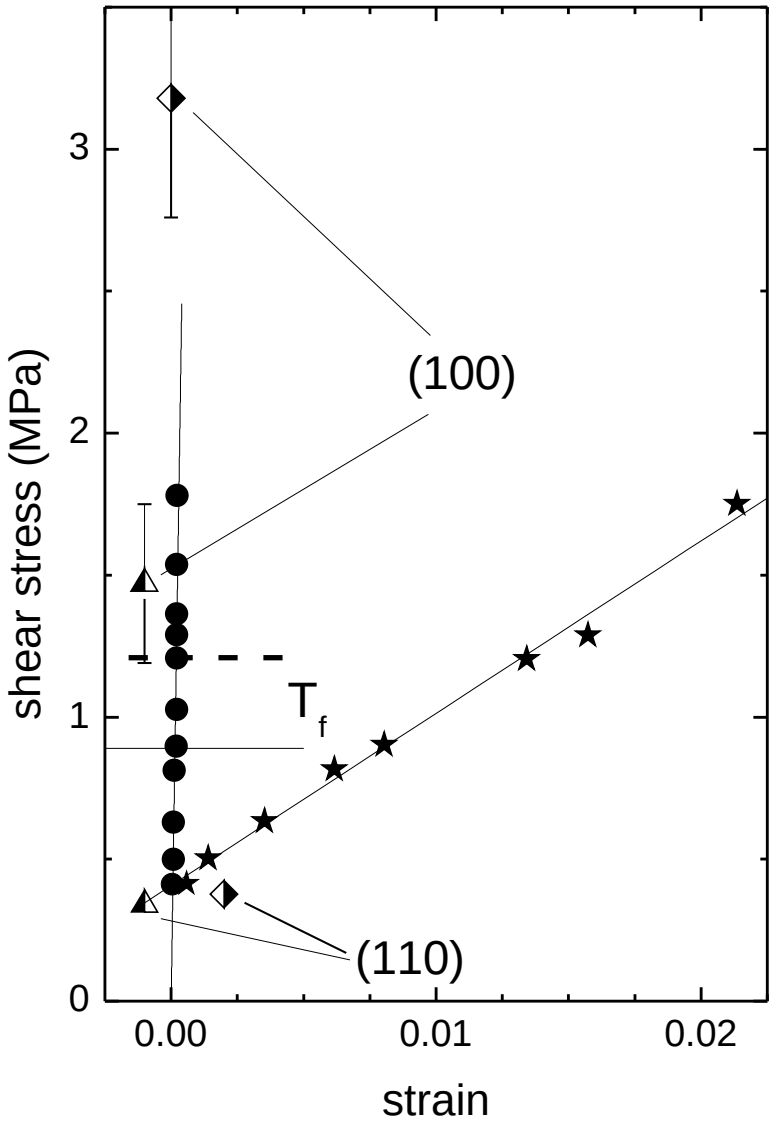

Figure 3.2: Stress-strain relationship observed by uniaxial pressure on single crystals of CuCl:NaCl—circles and pure NaCl—stars. Solid lines are results of least square linear fits. Furthermore, the characteristic data for the plastic behavior of NaCl and KCl were obtained by averaging values from different sources. Diamonds represent T_{crss}— values in the NaCl glide plane (110) [NTH02, Dom34, GN70, Sea81, SB55, KKN74] and the high value for the glide plane (100) [Dom34, GN70, Sea81, SB55, KKN74]. Triangles are data for KCl for glide plane (110) [GN70, Sea81] and for glide plane (100) [GN70, Sea81]. Horizontal lines indicate the fracture stress T_f of NaCl (solid line) and KCl (dashed line).

T_{cr}, and the material changes shape by gliding and the solid fails at T_f by atomic sliding

through dislocation motion.

The strain values match the observed persistent changes of the height. They correspond to half of the applied magnitudes of the vertical pressure to the shear stress and this value is significant for activating the gliding processes. The small inconsistency of data points of the CuCl:NaCl sample from the exact vertical line does not exceed the experimental uncertainty. The observed slope for the NaCl sample is two orders of magnitude smaller than in the CuCl:NaCl sample. The yield stress is S = 0.41(2) MPa, the corresponding literature data of NaCl (diamonds) and KCl (triangles) are 0.38 MPa and 0.34 MPa. All these data support the impression from Fig. 3.1 that edge dislocation are the origin the anomalous phenomenon.

3.1.2 FWHM in pure and in doped NaCl

Samples of pure and doped NaCl powder were prepared by pulverizing pieces of single crystals. The powder samples were investigated by X-ray diffraction. When studying the stored strain in the material due to the preparation procedure, the observed line-widths of Bragg reflexes in pure NaCl are larger than expected from the well-known data of a single crystal which has been subject of a plastic flow mechanism. This effect of broadening is absent in NaCl containing CuCl nanocrystals.

The samples under consideration are listed in Table 3.2

Table 3.2: Characterization of powder samples prepared from pure and doped NaCl crystals. First column: name of samples: P— pure material, HD— high doping, LD— low doping, VD— varying doping and MD— medium doping). Second column describes the amount of CuCl in the melt. Third column and fourth column describe the mole fraction of crystalline amount x_{cr} and the total amount x_{tot} of CuCl molecules where the numbers have to be multiplied by 10^{-4}. In the last column T_{gr} describes the temperature at which the nanocrysals nucleated and T_{ann} describes the annealing temperature. The grains have a diameter of about $20\,\mu$m.

Sample	**Chemical Data**	x_{cr}	x_{tot}	**Remarks**
P1	NaCl pro analysis grade(p.a.)			first measurements
HD	4%CuCl; NaCl p.a	12.7	17.4	T_{gr} = 120°C for 20 days
P2	NaCl super-pure (s.p.)			
P3	P3 is the annealed P2 sample			T_{ann} = 327°C for 2 days
P4				solution growth
LD	0.6%CuCl; NaCl p.a.	0	1.7	as grown
VD1	1%CuCl; NaCl p.a	0.93	3.1	T_{gr} = 40°C for 34 days
VD2	2%CuCl; NaCl p.a.	2.5	4.7	T_{gr} = 40°C for 34 days
VD3	3%CuCl; NaCl p.a.	3.7	6.4	T_{gr} = 40°C for 34 days
MD1	2.5%CuCl; NaCl s.p.	4.1	9.1	as grown
MD2	2.5%CuCl; NaCl s.p.	4.2	9.2	T_{gr} = 82°C for 4 days
MD3	2.5%CuCl; NaCl s.p.	4.2	8.9	T_{gr} = 97°C for 4 days
MD4	2.5%CuCl; NaCl s.p.	4.0	8.1	T_{gr} = 112°C for 4 days

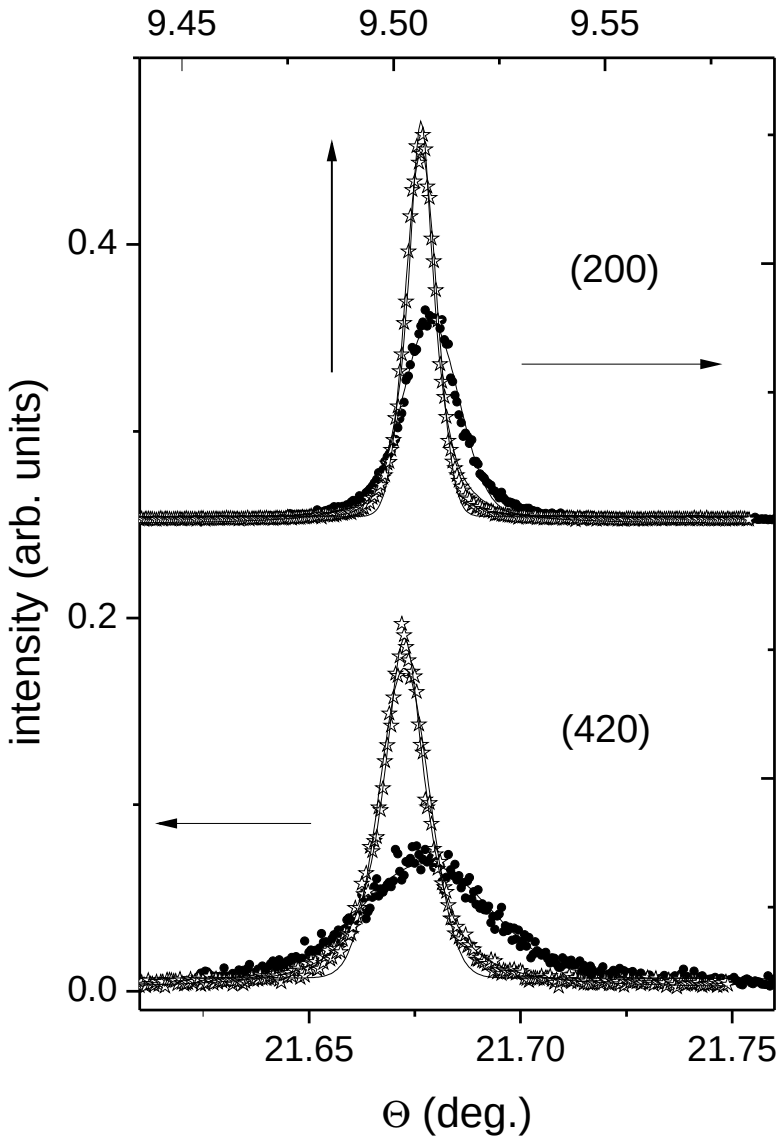

Figure 3.3: Diffracted X-ray intensity of (200) and (420) reflexes as a function of θ. Sample P2 (full circles) and sample P3 (open stars) of pure NaCl. The diffracted angle is 2θ.

The reflexes (200) and (420) of the pure NaCl for the samples P2 and P3 are illustrated in Fig. 3.3. The Full Width of Half Maximum (FWHM) increases with increasing Bragg angle θ. The FWHM is given as the width of the diffraction peaks in radians, at a height half-way between background and the peak maximum. In sample P2 (full circles), a broadening of the peaks was observed. This broadening characterizes the state of the NaCl immediately after the pulverizing, when the stored strain was induced into the NaCl powder. In the preparing technique by "pestle-in-a-mortar", the grains suffer deformations

and these deformations can be observed in the broadening of the reflection peaks. The annealing effect in sample P3 (opens stars) leads to a narrowing of the reflex peaks. Obviously, this illustrates a relaxation of the in-built strain induced by the preparation.

The line widths of the P1 sample shows a significant broadening, which is found to be between those of sample P2 and P3. In addition to different line widths, we observe a small relative shift in the central peak position of the Bragg angles between the P1 and P3 samples. Solid lines are fits by Gaussian functions-all peaks and by a Lorentzian functions-only open stars(narrow peaks). The Gaussian curves are more narrow at the peak foot and show a smaller maximum intensity as compared to the Lorentz curves.

Fig. 3.4 is a comparison of the (420) reflexes in pure and doped NaCl in two pairs of samples: (a)(P1–HD) and (b)(P2–HD). Open symbols show the results of Gauss fits as well as Lorentzian curves. The two narrow lines (full symbols) were fitted by Lorentzian functions in (a) and by Gaussian functions in (b). In both cases the peaks of samples P1 and P2 (pure NaCl) are broader compared to the reflexes of HD (doped NaCl). In doped material, the peaks are well described by different functions, for instance by pseudo-Voigt fit functions. The pure NaCl powder samples show a strong broadening of the Bragg reflexes, due to plastic deformation in grains (see Fig. 3.4). The line widths depend on the diffraction angle as expected for strain stored in grains [CPR58]. The peak broadening in pure NaCl is accompanied by line shifts in the spectrum. The broadening effect of the peaks is completely absent in NaCl containing CuCl nanocrystals (see Fig. 3.5). Obviously, the observed quenching effect of strain storing by the nanocrysals is the first demonstration of a strong influence on micro-mechanical properties of crystals.

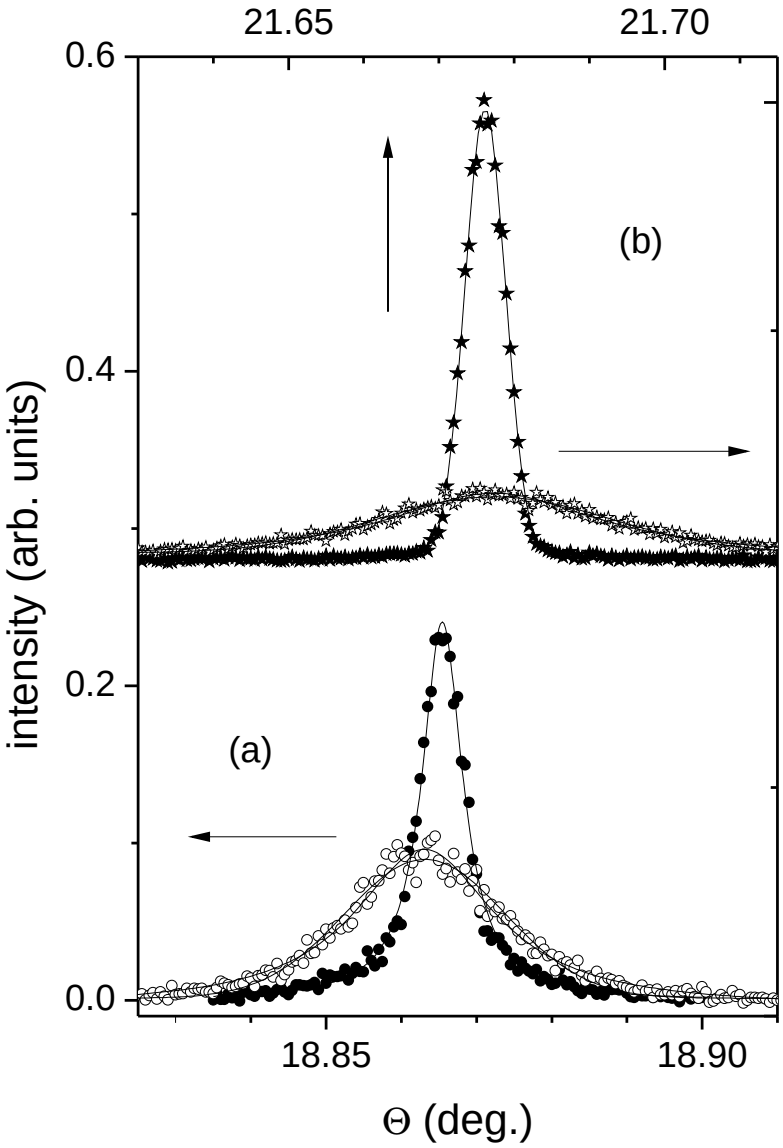

Figure 3.4: (a) Diffracted X-ray intensity of (400) reflexes in sample P1 (open circles) and in sample HD solid circles.(b) Diffracted X-ray intensity of the (420) reflexes in sample P2 (open stars) and in sample HD (solid stars).

The present measurements distinguish clearly between two types of materials, one shows broadening (see Fig. 3.5 (a)) and the other one shows nearly no broadening (see Fig. 3.5 (b)). This observation reduces the problems in the diffraction line profile analysis. Expanding the Bragg equation into a power series, due to small changes Δd of the lattice spacing (d) yields, leads to:

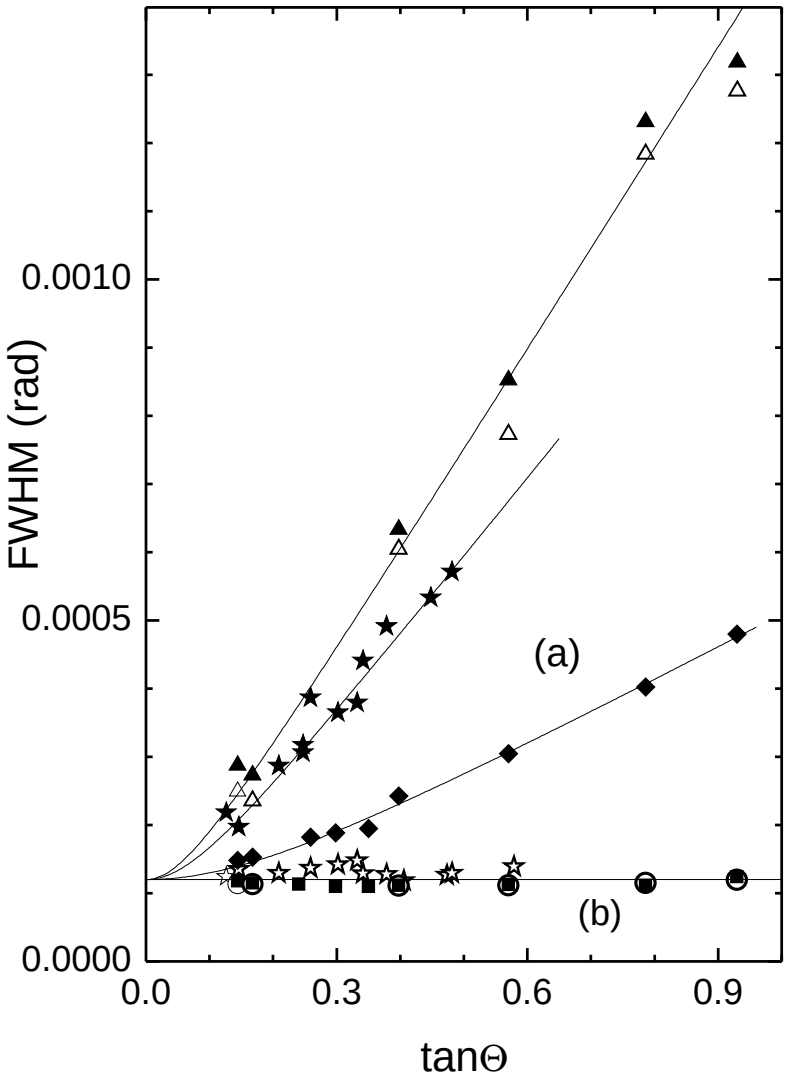

Figure 3.5: Full Width at Half Maximum (FWHM) in the θ representation as a function of $\tan\theta$. (a) Type-I material: solid lines represent fits according to Eq. 3.2. (full triangles) sample P2, (full stars) sample P1 and (diamonds) sample P3 .(b) Type-II material: solid lines represent $\Delta\theta_0 = 0.00012$ red: (circles) sample HD2, (open stars) sample HD1 and (squares) sample MD4. Open triangles in (a) are data of sample P2 analyzed on the basis of a Lorentzian fit function.

$$\theta = \theta_0 - tan\theta \cdot \left(\frac{\Delta d}{d}\right). \tag{3.1}$$

If $\left(\frac{\Delta d}{d}\right) = S_d$ contains the stored strain, (θ) and (θ_0) are the observed and the true Bragg angles. If the sample consists of homogeneously deformed volume parts of mesoscopic

size, S_d changes the shape of a reflection directly. This is the case if S_d is produced by dislocation gliding. The FWHM is used as a measure of the broadening of a reflection by S_d. Taking into account a constant contribution ($\Delta\theta$), the total line width in terms of a (θ)- dependence is described by:

$$FWHM(\theta) \;=\; \Delta\theta \;=\; \left((\Delta\theta_0)^2 + (S_d \cdot tan\theta)^2\right)^{\frac{1}{2}} \tag{3.2}$$

The parameter ($\Delta\theta_0$) describes the instrumental contribution to the total line width and the parameter S_d is used as a measure for the distribution of the stored strains. In the case of pure shear strains, S_d reflects a canting of lattice planes without a change of the volume. Both quantities are obtained by least squares fits. Eq. 3.2 is a reduced form of the general expression suggested in literature [UGRB01, BAD$^+$04, KS04, BP05]. Notice, that the value of S_d is independent of (θ) indicating the isotropy of the strains.

The FWHM of the line broadening with θ corroborates that two types of materials exist (see Fig. 3.5). Samples P1, P2, P3, P4, and sample LD belong to the type-I material. These types of material show a large amount of stored strains and the absence of CuCl nanocrystals. Samples HD, VD2, VD3, and (MD1,...,MD4) belong to the Type-II material and these contain a large amount of CuCl nanocrystals. Obviously, no strain stored can be detected. The reflexes from the type-I material show a line shape between a Gaussian and a Lorentzian function. Type-II materials, show a pronounced Lorentzian shape function. As illustrated in Fig. 3.5, Eq. 3.2 describes the line-broadening correctly with a θ-independent parameter S_d. In Type-II materials (see Fig. 3.5 b doped NaCl) it is found that the FWHM does not depend on θ , obviously a constant value is determined.

This effect is also missing in Type-I materials which agrees with the observation of individual grains under the optical microscope. Representing $\Delta\theta_0$ and S_d of Eq. 3.2 for all Type-II spectra yields the average value $\Delta\theta_0 \;=\; 1.20(5) \cdot 10^{-4}$ and this value is used as the instrumental component of the broadening also for Type-I materials which show line shapes between Gaussian and Lorentzian peaks as illustrated in Fig. 3.3. In Fig. 3.5, the measurements on sample P2 show that using one of two ways of analysis(Gaussian or Lorentzian function) does not change the value of the S_d significantly.

3.1.3 Final lattice parameter in pure and doped NaCl

The powder samples described in Table 3.2 were studied by X-ray diffraction scattering experiments. The stored strain effect in pure NaCl has an influence on the FWHM and the lattice parameter. Type-I material (pure NaCl) shows a linear dependence of the lattice parameter due to the stored strain effect in grains.

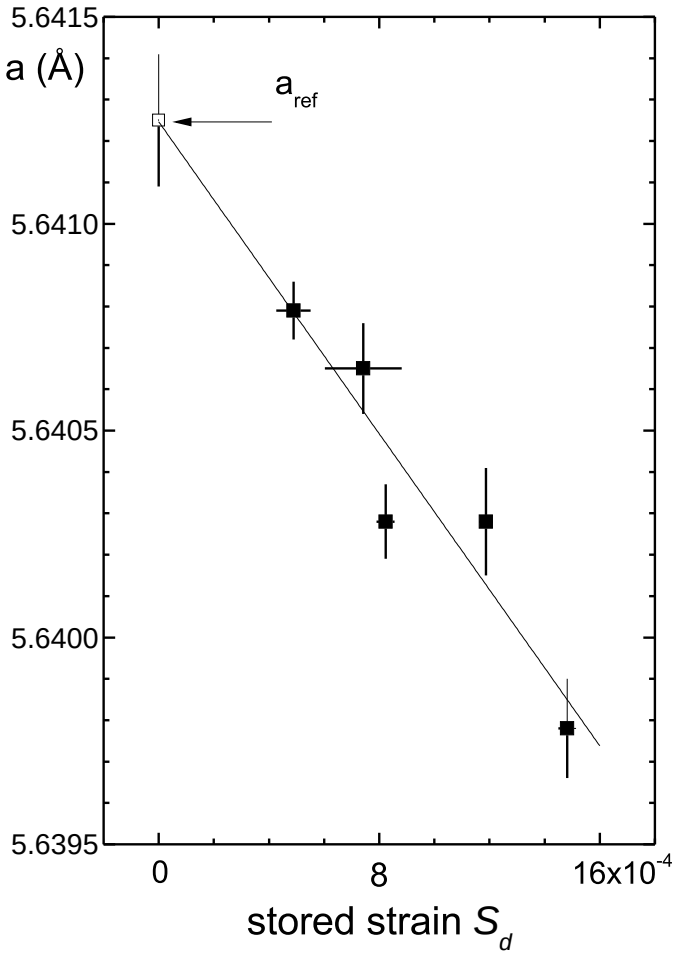

Figure 3.6: The lattice parameter a_{NaCl} as a function of stored strain S_d in type-I material. With increasing S_d the following samples are presented: P3, LD, P4, P1 and P2.

A small relative shift of the Bragg-angles between the samples P2 and P3 is observed in Fig. 3.3. This indicates the existence of an average strain according to Eq. 3.1.

The lattice parameter as a function of stored strain is given by:

$$a \;=\; a_{ref} \;+\; \left(\frac{\partial a}{\partial S_d}\right) \cdot S_d \tag{3.3}$$

As demonstrated in Fig. 3.6, the lattice parameter a_{NaCl} which is determined from the central positions of the Bragg peaks is a linear function of the stored strain S_d. Extrapolating the lattice parameter of the Type-I material to S_d gives the value $a_{ref} = 5.64125\mathring{A}$ and represents the lattice parameter in pure NaCl, which contains no internal strains.

The average strain in Type-I material is given by:

$$S_I = \left(\frac{a_{NaCl} - a_{ref}}{a_{ref}}\right) = \left(\frac{1}{a_{ref}}\right) \cdot \left(\frac{\partial a}{\partial S_d}\right) \cdot S_d, \tag{3.4}$$

where $\left(\frac{\partial a}{\partial S_d}\right)$ = -0.943 and reflects the change due to stored strain in pure NaCl. The relation between both strain types is given by $|\frac{S_I}{S_d}| = 0.173$. It is concluded, that in addition to S_d stored strain a second strain S_I should exist which is described by a volume contraction in the material. The small value indicates that the stored strain is mainly shear strain. Fig. 3.6 illustrates the lattice parameter dependence of the stored strain due to the pestle in a mortar technique. Sample P3 which is P2 annealed at 327° C, is found to show a simultaneous recovery of S_d after thermal treatment. Obviously, the

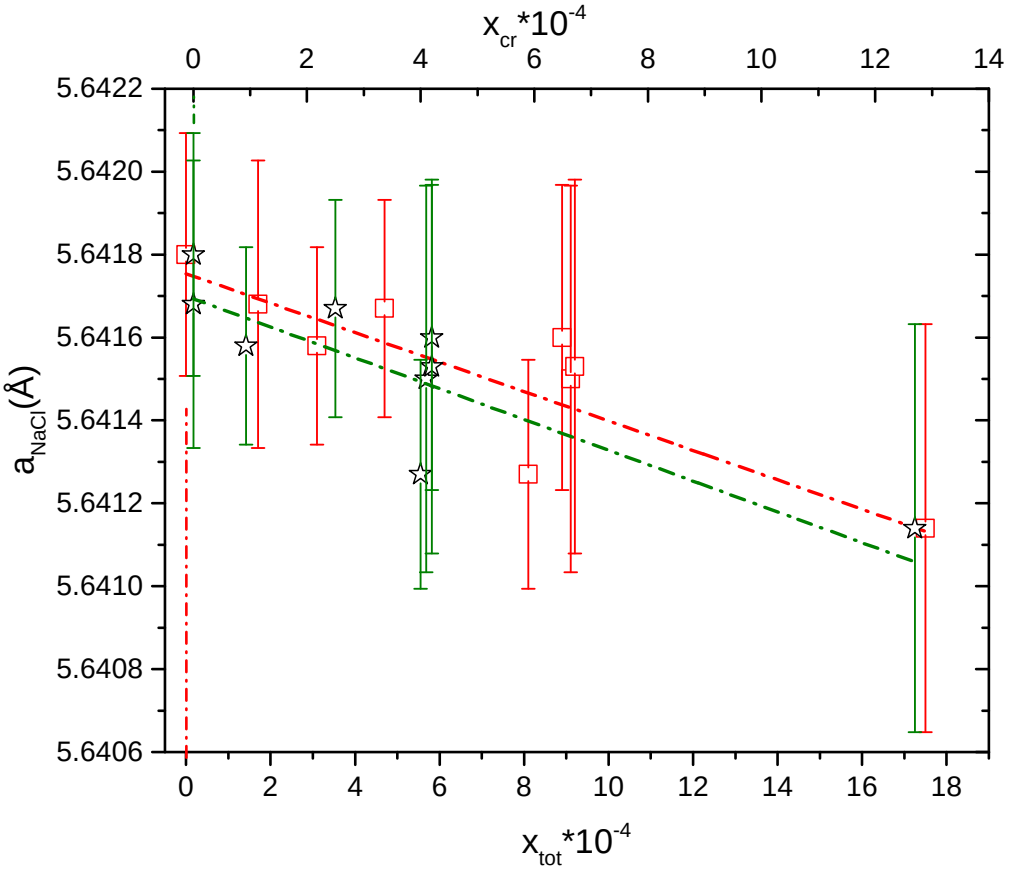

Figure 3.7: The lattice parameter a_{NaCl} as function of cristalline CuCl molecule concentration: (black open stars) x_{cr} concentration of CuCl nanocrystals, (red open squares) x_{tot} total concentration of CuCl in NaCl matrix.

lattice parameter a_{NaCl} shows a dependence of the chemical contamination by CuCl and this is illustrated in Fig 3.7. Extrapolating the lattice parameters of Type-II material to

zero value the following values are found: the lattice parameter in the absence of CuCl is $a_{ref}^{tot} = 5.64175\mathring{A}$ for x_{tot} and the stored strain due to chemical contamination is S_{II}^{tot} = -5.5 $\cdot 10^{-4}$. Considering the nanocrystal contribution, the lattice parameter is found to be $a_{ref}^{cr} = 5.64169\mathring{A}$ for x_{cr}, and this value defines the absence of nanocrystals in NaCl. The stored strain due to CuCl nanocrystals in NaCl matrix is $S_{II}^{cr} = -9.75 \cdot 10^{-5}$.

For the Type-II material a relation between the lattice parameter and the amount of $CuCl$ in the samples is defined.

$$(a_{x_{tot}} - a_{ref}) = \left(\frac{\partial a_{x_{tot}}}{\partial x_{tot}}\right) \cdot x_{tot} \text{ or } \left(\frac{a_{x_{tot}} - a_{ref}}{a_{ref}}\right) = \left(\frac{1}{a_{ref}}\right)\left(\frac{\partial a}{\partial x_{tot}}\right) \cdot x_{tot} \quad (3.5)$$

where i represents the total amount of CuCl crystalline molecules in NaCl (x_{tot}) or the amount of CuCl nanocrystals in the NaCl matrix (x_{cr}). $|\frac{S_{II}}{x_{cr}}| = 6.30 \cdot 10^{-6}$ and $|\frac{S_{II}}{x_{tot}}| = 8.86 \cdot 10^{-6}$ reflects some changes according to the chemical contamination due to CuCl nanocrystals and Cu^{+} ions in matrix.

At first one has to realize that the results illustrated in Fig. 3.7 cannot be compared with Fig. 3.6. Nevertheless, two different contribution can be distinguished in the experimental data. The first one is due to the embedding of CuCl nanocrystals in the material and the second one is due to the mechanical procedure to prepare the sample by pestle-in-a-mortar.

Elastic model–part 1

The experimental results obtained in samples with an internal stress level below the fracture stress show evidence for a stored strain mechanism. Thus, the pulverization procedure in combination with the measurement of stored strains can be used as a test for the existence of embedded nanocrystals. The interaction between the dislocations and the small obstacles given by the CuCl nanocrystals predicts the increase of glide forces. However, the observed quenching of strain storage by the nanocrystals must be a consequence of the propagation of dislocations in the material. The same considerations are made in the case of a fracture mechanism. The experimental conditions permit storing of strains only in samples with an internal stress below to a special value. It is suggested that the produced stress field surrounding the nanocrystals is the reason for the shear stress that a sliding dislocation is feeling, when it meets the surrounding field of the nanocrystals. The dependence of the stored strain S_d on the mole fraction of CuCl which is embedded as nanocrystals is presented in Fig. 3.8. $S_d^0 = 14.69 \cdot 10^{-4}$ has been used as a maximum value for the pure NaCl sample P2. (a) The black dotted line represents the pure NaCl samples (Type-I material). (b) represents the VD1 sample which contains a small amount of nanocrystals. (c) The residual strains of Type-II materials versus doping level x_{cr} (red dash dotted line). The observed dependence of the stored strain on doping rules out the explanation of its reduction by an usually strong effect of so called solution strengthening[Spr76]. To find an explanation, the shear stress which a sliding dislocation is feeling when the stress field surrounding a nanocrystal is met.

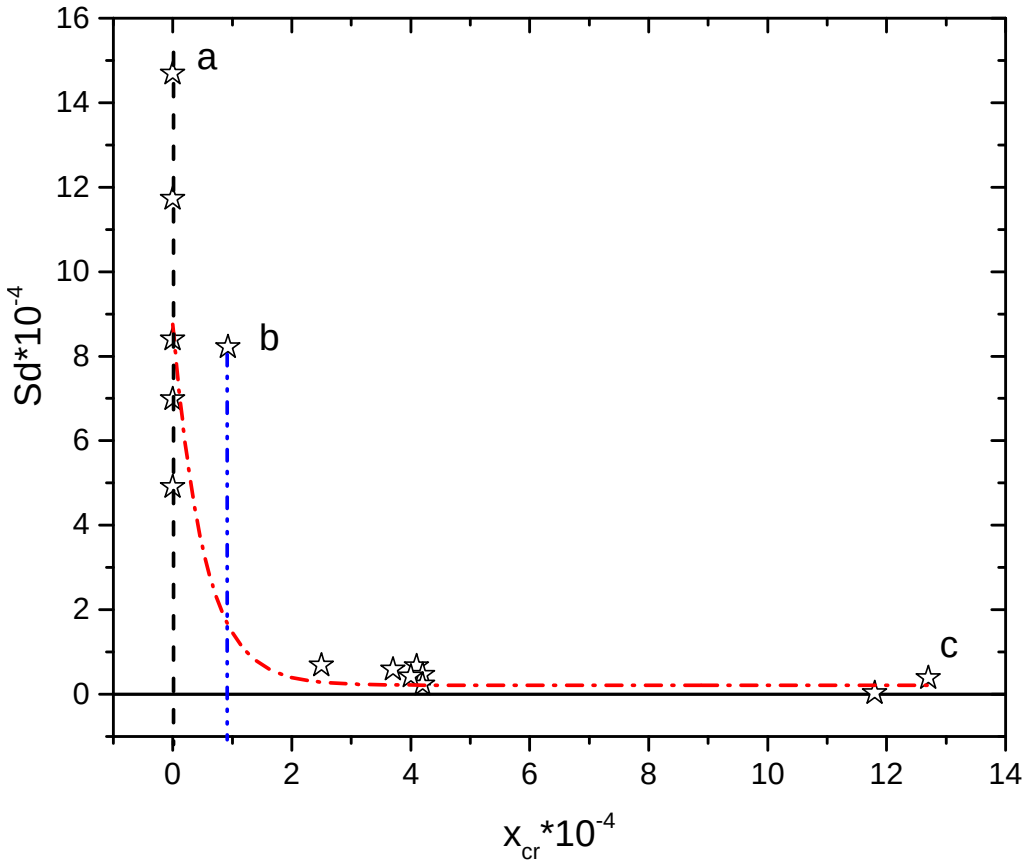

Figure 3.8: Stored strain as a function of nano-crystalline concentration x_{cr} for CuCl:NaCl. (a): (black dashed line) represents Type-I materials; (b): (blue dash dotted line) represents sample VD1 and (c): (red dash dotted line) represents Type-II materials.

A model which describe the elastic interaction between nanocrystals and matrix has been developed. Considering a spherical nanocrystal of radius R_0 surrounded by the NaCl matrix, two approximations have been assumed. First, the elastic tensor of the nanocrystals and the matrix is isotropic and secondly the relation

$$\left(\frac{R_0}{R_\alpha}\right)^3 = x_{cr} \tag{3.6}$$

holds. Equation 3.6 defines the effective average radii where the R_α is the radius of a spherical elastic model unit with a nanocrystal of the radius R_0 at the center. Without any relaxation the lattice mismatch, $\Delta R = \left(\frac{a_{NaCl}-a_{CuCl}}{a_{NaCl}}\right) = 0.041$, would produce a gap ΔR between the nanocrystals and its surrounding matrix. Obviously, an inter-facial force closes the gap by the radial displacement.

The radial displacement is described on the basis of the elastic continuum theory [LL70]:

$$u_r \;=\; a \cdot r + \frac{b}{r^2}, \tag{3.7}$$

where r describes the distance from the center of the nanocrystals which coincides with the origin of a local system of spherical coordinates. Eq. 3.7 is the general solution of the differential equation obtained for spherical symmetry from the conditions of the elastic equilibrium equation. It is valid for $r > R_0$ and $r < R_0$, where in the latter case b = 0 [SGB03]. In Equation 3.7, (a) and (b) are coefficients which are determined by the elastic boundary conditions. Taking into account the elastic model consideration, two boundary conditions have been applied:

i) The radial interfacial stress T_r^0 imposed on the matrix is balanced by the stress imposed on the nanocrystals,

ii) T_r^0 - closes the total gap ΔR.

In this case, one obtains the following stress field for the surrounding matrix[WSPV04]:

$$T_r \;=\; C_{01} S_0 + 2K \left(\frac{R_0^3}{r^3} \right). \tag{3.8}$$

The parameter (b) from Eq. 3.7 is included in relation of K from Eq. 3.8 and a complex combination of elastic constants. The strain S_0 = a is the homogeneous and isotropic strain of the whole sample and $C_{01} \;=\; c_{11} + 2 \cdot c_{12}$ is one of the the two scalar invariants of the elastic tensor. By use of a_{ref} presented in Fig. 3.6, we have determined S_0 of Type-II materials. It is obtained for the related homogeneous stress and the experimental magnitude is $T_0 \;=\; C_{01} S_0$ = -9 MPa and K = 920 MPa. Nevertheless, considering Fig. 3.6 and Fig. 3.8, two results of importance have been found.

I) The internal shear stresses are significantly larger than those needed for activating gliding or cleaving.

II) The deformation field around the nanocrystals contains the potential power to stop the propagation of sliding dislocation.

However, quantitative attempts failed to correlate the data for the residual S_d of Type-II material to the average radii R_0 obtained from optical measurements. The interaction between dislocation and small obstacles predict the increase of the glide forces. The strong effect in Type-II material can be considered as a consequence of the relatively large mismatch between the nanocrystals and the matrix. To exhaust the whole potential of internal forces, the inter-facial gap should be smaller than at least $\left(\frac{a_{NaCl}}{2}\right)$ which limits the radius of the embedded particles.

3.1.4 Summary

The experimental results obtained by uniaxial piezooptical and X-ray diffraction measurements show a difference between pure NaCl and doped NaCl. In pure and in doped NaCl strong differences due to sample preparation have been observed. A different structural relaxation in doped NaCl has been observed compared to a NaCl single crystal.

Pure NaCl presents a storage strain effect due to the existence of the dislocations. The stored strains effect is absent in doped NaCl. In an uniaxial experiment performed on CuCl:NaCl material it is observed that the optical anisotropy is undistorted and the birefringence bands are missing. Thus, the stored strain effect in doped NaCl is missing.

It is well known that a material fails because cracks are moving inside in the material. The uniaxial pressure effect will induce gliding in the pure but not in the doped material. The unstored strain effect in doped NaCl can be considered as a consequence of the stress fields produced by the nanocrystals-matrix elastic interaction. Nevertheless, the nanocrystals will stop the propagation of dislocations in the material.

Samples which are belonging to Type-I material are characterized by a large amount of stored strains and by the absence of CuCl nanocrystals. In pure NaCl a strong broadening of Bragg reflexes is observed. The broadening effect is induced by plastic deformation of the material. The line widths depend on the diffraction angle as expected for a distribution of isotropic stored strain in the grains. In the case when the FWHM is independent by θ this reflects the existence of Type-II material where the stored strain is absent.

Fortunately, the material itself provides a first estimate of the stress-strain field of elastic-plastic phenomena. The critical resolved shear stress T_{cr} indicates the magnitude of the shear stress which is needed to activate the easy glide system $[110]\{\bar{1}10\}$, and the fracture stress T_f is the tensile stress normal to a (100) plane.

CuCl:NaCl contains enough internal stress due to the incorporated nanocrystals in the matrix. Obviously, the nanocrystals stop the propagation of glide dislocations and thus can be assumed to be a prevent factor in the storage strain mechanisms. The experimental results show an unusual effect resulting in stored strain when the $NaCl$ is pulverized using a pestle in a mortar. The stored strain is missing stability against soft annealing conditions. The experimental conditions permit storage of strain only in samples with an internal stress level below the fracture stress. This result suggests that the pulverization procedure in combination with the measurement of stored strains can be used for testing the existence of embedded nanocrystals. The interaction between dislocations and small obstacles predicts the increase of the glide forces.

From a practical point of view the amplification of stored structural changes is attractive because it provides a simple and a quick test on the existence of plastic flow in a material. The storing strain and the fracture effects can be avoided by embedding of CuCl nanocrystals in the NaCl host material.

3.2 Optical birefringence measurements

Optical anomalies were observed by measurements in rectangular samples made from a single crystal of NaCl which contains a low concentration of CuCl in the sample SA. The embedded nanocrystals serve as source for volume forces which generate a spatial dependence. The dimensions of the sample are relatively large. During the experiments it happened that SA was cleaved. The biggest broken part will be called SB. The sample SB was prepared, including grinding and polishing, using the same mechanisms and an identical machine as for the sample SA.

The samples are fixed on a holder allowing movements along the horizontal and the vertical axes. Usually, in optical birefringence experiments the horizontal axis serves as scanning axis x_s. The copper concentration in the sample is given by $x_{ion} = 1.1 \cdot 10^{-4}$, and $x_{cr} = 4.3 \cdot 10^{-4}$. For the coordination of the system of the sample the following convention is chosen: $L_1 < L_2 < L_3$. The dimensions of the sample SA are given by: $L_1 = 6.99$ mm, $L_2 = 8.04$ mm and $L_3 = 10.21$ mm. Notice, that all x_i are parallel to the crystallographic axes.

The beam of a He-Ne laser transmits the sample perpendicular to x_s along the x_t axis. The horizontal beam is parallel to x_t, the horizontal scanning of the sample is along x_s and x_p is parallel to the vertical direction, perpendicular to x_t and x_s as presented in Fig. 3.9. A linearly polarized wave becomes elliptically polarized by an anisotropic sample. The ellipticity ϵ is determined with an accuracy of about 20 μrad.

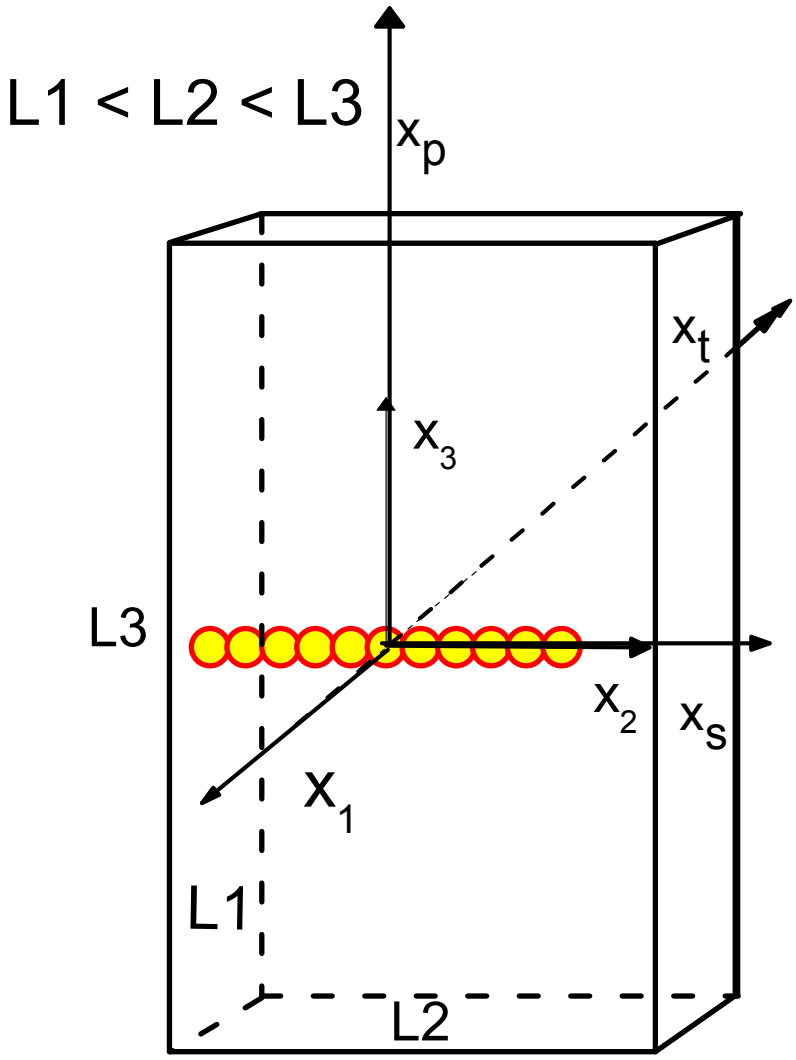

Figure 3.9: Illustration of used systems of coordination. The coordinates of the laboratory system are (x_t, x_s, x_p) and (x_1, x_2, x_3) are the coordinates of the sample system. The origin of the sample system is its center. The origin of the laboratory system is defined by the x_t axis which coincides with the laser beam scanning if $x_s = x_p = 0$.

3.2.1 Break of symmetry

The birefringence experiment has been accomplished for $\theta = 45°$ and $\theta = 0°$. $\theta_{(0)}$ and $\theta_{(45)}$ denote the azimuthal orientation of the polarizer and the compensator which is a quarter-wave plate that compensates the $(\frac{\pi}{2})$ phase difference of two main axes of the elliptically polarized waves leaving the sample. The Faraday cell is driven by an alternating current. If its signal vanishes by rotating the analyzer its position indicates the ellipticity induced by the sample.

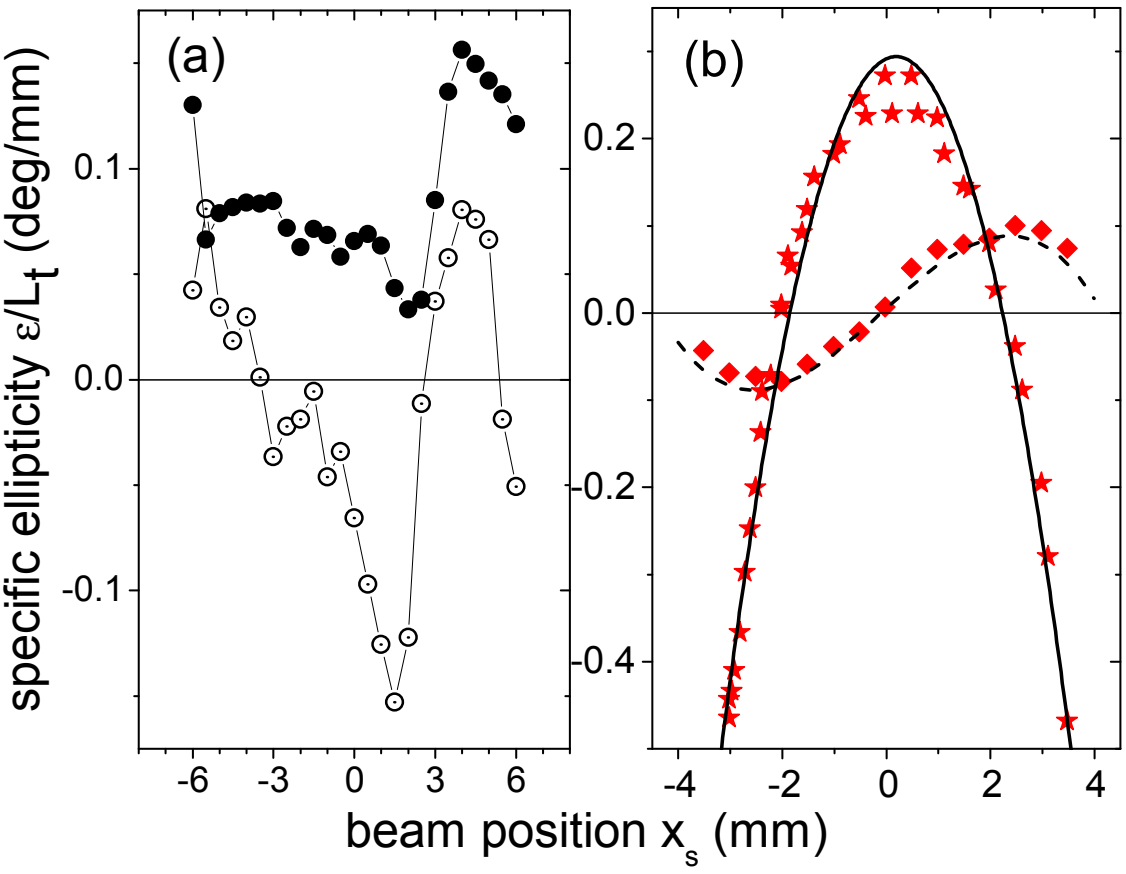

Figure 3.10: Indication of anomalous birefringence in pure and doped NaCl materials. (a) Specific ellipticity $\frac{\epsilon_{(0)}}{L_1}$ (solid circles) and $\frac{\epsilon_{(45)}}{L_1}$ (open circle) versus the position of the laser beam in pure NaCl for a horizontal scan. Lines are guides to the eye. (b) Specific ellipticity $\frac{\epsilon_{(0)}}{L_1}$ (full stars) and $\frac{\epsilon_{(45)}}{L_1}$ (solid diamonds) versus the position of the leaser beam in sample SA of CuCl:NaCl for a horizontal scan. Solid lines represent the fits as explained in the text. In both samples the vertical scan position is $x_p \approx 0$ for $\epsilon_{(0)}$ and $x_p = 2\,\mathrm{mm}$ for $\epsilon_{(45)}$.

The observed ellipticities for two angles are notated as $\epsilon_{(0)}$ for $\theta = 45°$ and $\epsilon_{(45)}$ for $\theta = 0°$. The ellipticity $\epsilon_{(0)}$ corresponds to the birefringence parallel to the x_p and x_s axes and it is proportional to the strain difference $\Delta S = S_{pp} - S_{ss}$. $\epsilon_{(0)}$ is represented by solid circles and solid stars in Fig. 3.10. In the case of $\epsilon_{(45)}$ the rotation of the analyzer is proportional to the shear strain S_{ps}.

In Figure 3.10 (b) the typical curves observed in the doped sample SA together with those in the nominal pure NaCl material are presented Fig. 3.10.(a). The magnitudes of the local birefringence data differ in both materials only by a factor of two. The more important and significant difference is the strong correlation of local birefringence data between two opposite faces in the CuCl:NaCl sample SA in contrast to the absence of

this type of correlation in the pure NaCl material. Obviously, a minimal concentration of identical sources of local stress is needed to develop the collective phenomenon which manifests itself as a systematic dependence of birefringence on the influence of opposite faces.

However, the ellipticities $\epsilon_{(0)}$ and $\epsilon_{(45)}$ characterize a volume effect. We like to note, that the measurements in Fig. 3.10.(a) were performed with a commercial sample without a special quality certification. Measurements performed on a pure home made sample which was made by supra-pure NaCl did show a birefringence which is significantly smaller compared to CuCl:NaCl. The ellipticity $\epsilon_{(0)}(\ \theta\ =\ 45°)$ was observed by scanning the sample at $x_p\ =\ 0$. Changing the height of the sample the effect does not change significantly. At the same position of sample ($x_p\ =\ 0$) no $\epsilon_{(45)}$ can be observed. The odd effect changes its sign at $x_p\ =\ 0$ and increases its magnitude for positive and negative x_p. In each position the value of n in $x^n\ \epsilon_{(45)}$ is maintained. Notice, that for $\epsilon_{(0)}$ the specific ellipticity shows a strain gradient.

Figure 3.11 exhibits a spatial dependence of $\epsilon_{(0)}$ in sample SB. In contrast to Fig. 3.10. (b) now the whole width of the sample has been exhausted for scanning. Small irregularities, in particular on the left side arise from the finite width of the laser beam which leads to uncontrolled interference phenomena. The collective character of both birefringences in Fig. 3.10 (b) again proves the existence of an internal strain field which connects the two opposite sides.

Most important for the whole sample is the birefringence $\epsilon_{(0)}$. It breaks the local centro-symmetry but not the global vertical mirror plane in Fig. 3.10 and in Fig. 3.11.

3.2.2 Frame effect

Changing the orientation of the sample, the same scheme of $\epsilon_{(0)}$ is observed for the following combination:

$[(x_s||x_1),(x_t||x_2)]$ and $[(x_s||x_2),(x_t||x_1)]$, in both cases $x_p\ =\ 0$.

Rotating the sample in Fig. 3.11 by $(\frac{\pi}{2})$ around x_2, the birefringence is proportional to $(n_1 - n_3)$. Now, the light is again parallel to x_2 and the scanning is parallel to x_3 $(x_s||x_3)$. The birefringence is $(n_p - n_s)\ =\ (n_1 - n_3)$. Scanning is performed for $x_1\ =\ 0$ and $x_s\ =\ x_3$. Now, the sign of $\epsilon_{(0)}$ is negative, its magnitude decreases in the positive as well as in the negative direction of the x_3 coordinate axis. However, on the way from the center to the left $-\frac{L_3}{2}\ \leq\ x_3 \leq 0$ and to the right side $(0 \leq x_3 \leq \frac{L_3}{2})$ a zero value of $\epsilon_{(0)}$ in Fig. 3.11 is observed.

Combining all those information, we obtained the scheme for a frame of birefrigence illustrated in Fig. 3.12. Most characteristic is the frame of the birefringence which is related to internal stress fields. The straight lines which indicate $\Delta n\ =\ 0$ have been obtained by direct orthoscopic observation under the polarization microscope. The latter technique works for sufficiently thick samples. In terms of the classical phenomenological photo-elastic theory the relations between birefringence and strain in the laboratory system are given by:

$$a_{pp} - a_{ss}\ =\ (p_{pppp} - p_{ppss})(S_{pp} - S_{ss}), \tag{3.9}$$

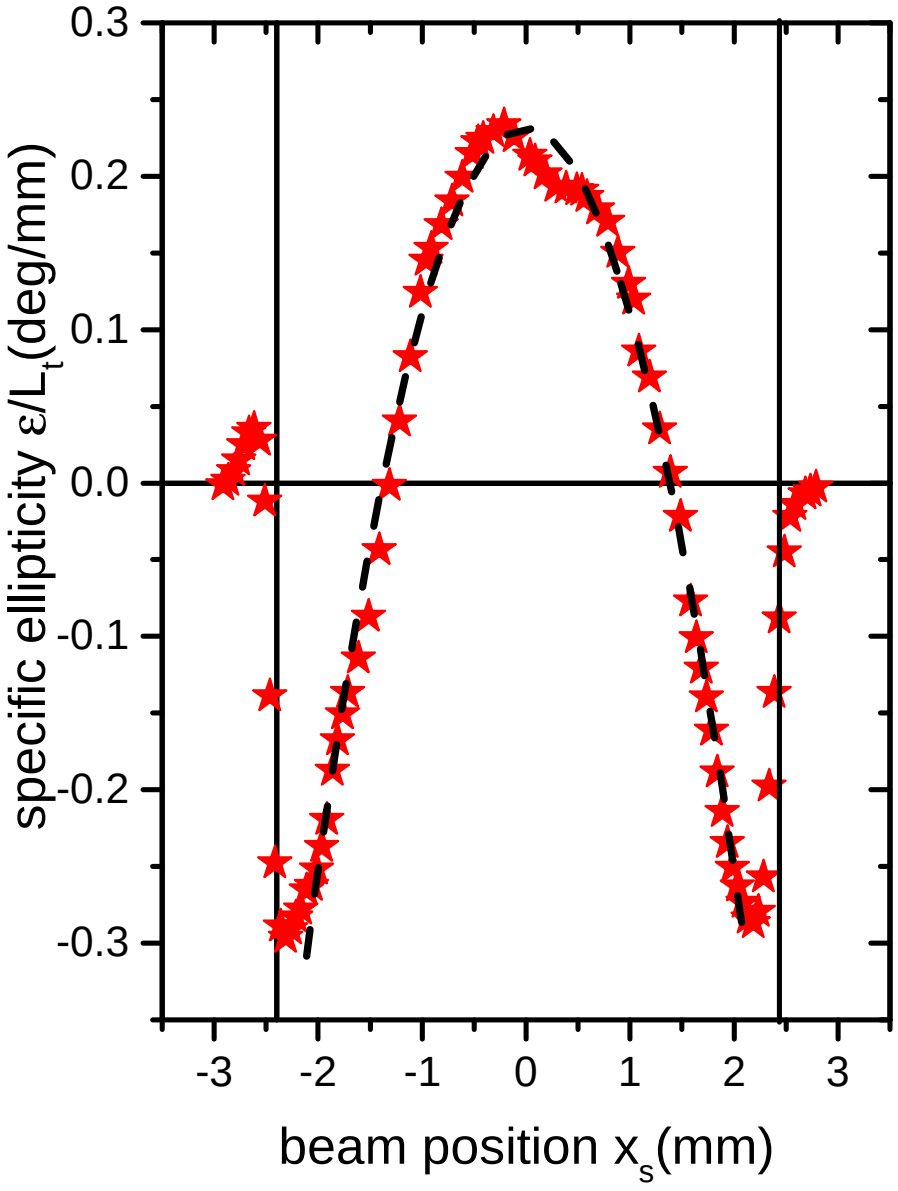

Figure 3.11: Specific ellipticity $\frac{\epsilon_{(0)}}{L_t}$ in sample SB. The L_i dimensions of the sample are $L_1 = 4.881\,(\mathrm{mm})$, $L_2 = 6.99\,(\mathrm{mm})$, $L_3 = 10.21\,(\mathrm{mm})$. The two vertical lines indicate the boundaries of the sample. Solid lines are fits of a quadratic x_s dependence.

where the a_{ij} denote the optical impermeability, the p_{ijkl} describe the photo-elastic constants and the S_{ik} denotes the elastic strain. In Eq. 3.9 the impact of cubic symmetry operations have been applied. The same relation in terms of the sample system of Fig. 3.12 reads

$$n_3 - n_1 \;=\; (p_{3333} - p_{3311})(S_{33} - S_{11}) \;=\; (p_{11} - p_{12})(S_3 - S_1) \tag{3.10}$$

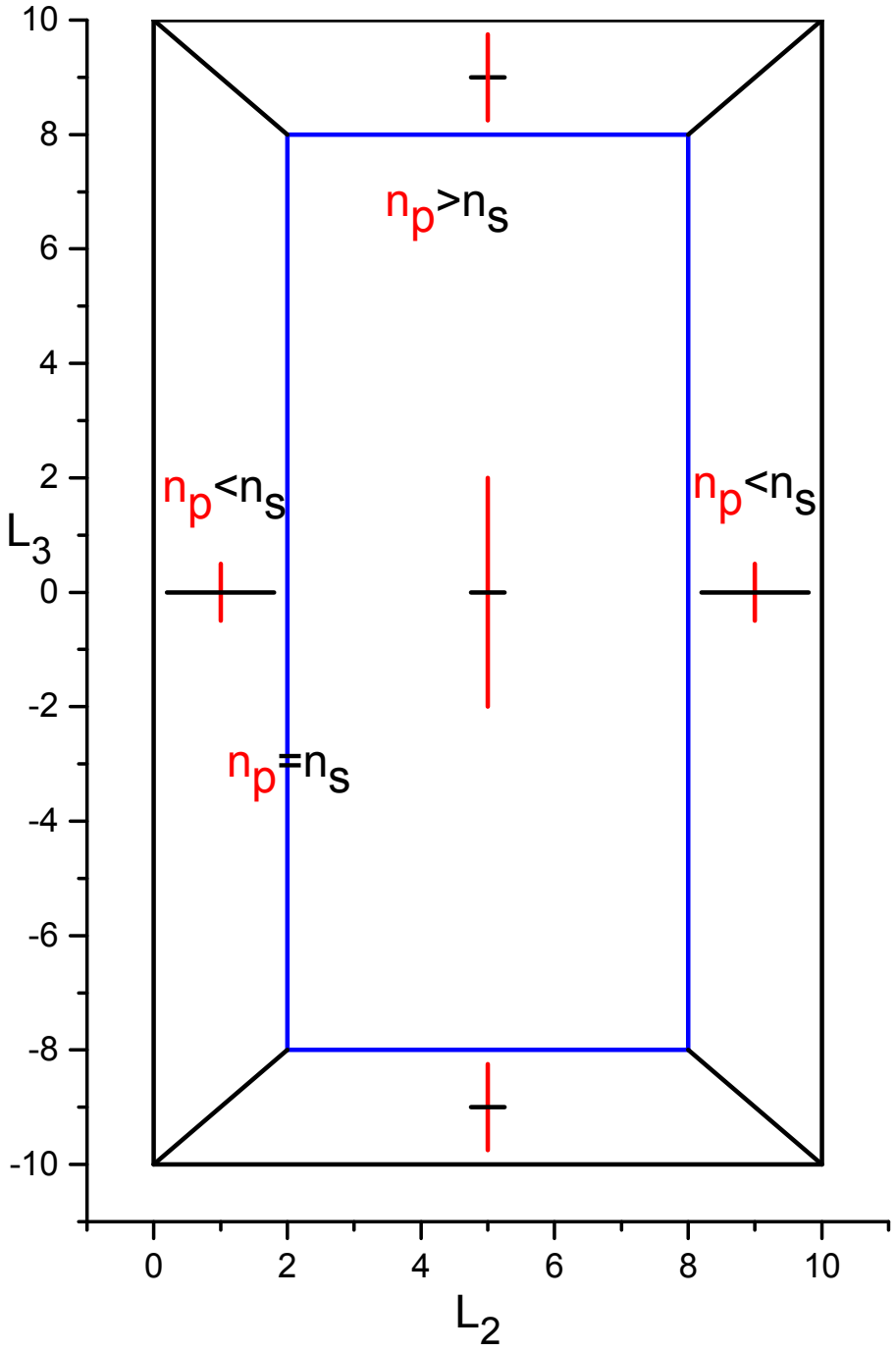

Figure 3.12: Sketch of the sample illustrates the frame effect in doped NaCl.

Here, in the last term of Eq. 3.10 the rules of short notation and the operations of cubic symmetry have been applied [LL70].

In NaCl, $\Delta p = p_{11} - p_{12}$, is negative. According to the results for the vertical fields on the left and right side of the sample $n_p - n_s = n_{33} - n_{11}$ is negative. Thus, $S_{33} - S_{11}$ must be positive, similar for the horizontal field on the top and bottom of the sample $n_p - n_s = n_{33} - n_{11}$ is positive. Thus, $S_{33} - S_{11}$ must be negative. Therefore, in all cases the force perpendicular to the surface is a tension.

It is interesting to note that the optical frame phenomenon shown in Fig. 3.12 is also observable in a rectangular glass sample which is heated for short time above the glass temperature. In course of cooling at first the surface region is solidified. When the residual body of the sample gets solid its shrinking induces dilatation forces onto the already cold and solid frame of the sample. Thus, the results are similarly as in Fig. 3.12.

3.2.3 Summary

In nominally pure NaCl a variation of birefringence has been found. The recorded $\epsilon_{(0)}(x)$ and $\epsilon_{(45)}(x)$ scans are presented in Fig. 3.10.(a). For the sake of comparison typical curves observed in the CuCl:NaCl sample SA are presented in Fig. 3.10.(b). The important and significant difference is the strong correlation of local birefringence data between two opposite faces in CuCl:NaCl and the missing of this kind of correlation in pure NaCl. Obviously, a minimal concentration of identical sources of local stresses is needed to develop the collective phenomena which manifest themselves as a systematic spatial dependence of birefringence. Both quantities $\epsilon_{(0)}(x)$ and $\epsilon_{(45)}(x)$ have been identified as volume effects by measurements in free standing and in doped samples. Fig. 3.11 presents data observed in sample SB, showing data observed for light propagation along x_2 and for scanning along x_1 of sample SB. Fig. 3.11 illustrates at once the absence of a center of symmetry. Without doubt the frame effect is the most interesting new phenomenon observed in the optical birefringence experiment(see Fig. 3.12). The optical birefringence of originally isotropic objects indicate the existence of uniaxial stresses which break the isotropy of the crystallographic unit cells.

An unexpected effect is the non-vanishing of $\epsilon_{(0)}(x)$ when approaching the surfaces as illustrated in Fig. 3.10.(b). In CuCl:NaCl the CuCl nanocrystals are local forces of stresses. By use of the values for x_{cr} and r_0 the average of 64.4 nm between nanocrystals is obtained. Nevertheless, a direct impact of the interfacial stress on the surrounding matrix is restricted to a cell with the average volume $V_c = (64.4\,nm)^3$ and the number of cells seen by the light beam is lying between 10^5 and 10^6 in the studied sample. This number suggests that details which are specific for a surface layer cannot be resolved experimentally.

3.3 Z_3 and $Z_{1,2}$ as detectors for embedded sources of local forces.

The exciton spectroscopy technique is used to study thermodynamic and kinetic phenomena in the course of phase separation processes [HW98]. The absorption measurements were carried out used a standard Spectrophotometer Cary 2300. The samples for optical analysis are listed below in Table 3.3.

Table 3.3: Characterization of samples investigated by UV-VIS Spectroscopy. First column: name of samples: LD,...,S17. Second column: x_m concentration of CuCl in the melt. Third column: d thickness of the samples. Fourth column: r mean radius of $CuCl$ nanocrystals determined at low temperature. Fifth column - Remarks: $T_{an} = 130^\circ$ C annealing temperature, $t_{an} = 24$ hours annealing time, T_H heating temperature, $t_h = 30$ minutes heating time.

S	x_m	$d[mm]$	$r[nm]$	**Remarks**
LD/ MD2	2.5	0.58/ 0.73	2.8	two different samples
S2	1	0.316	1.6	
S3	1	0.760	4.2	
S4	2	0.570	1.6	
S5	1	0.300	6.3	
S6	2.5	0.528	5.3	
S7	2.5	0.078	5.4	
S8	2.5	0.490	16.2	[110] direction
S9	2.5	0.145	16	[110] direction
S10	1	0.115	9.4	
S11	1	0.260	3.5	$T_{an} = 77^\circ$ C, $t_{an} = 2$ months
S12	1	0.609	7.3	$T_{an} = 112^\circ$ C, $t_{an} = 24$ hours
S13	3	0.891	2.8	$T_H = 300^\circ$ C,t_H, T_{an}, t_{an}
S14	3	0.757	4.8	$T_H = 400^\circ$ C ,t_H, T_{an}, t_{an}
S15	3	0.975	4	$T_H = 500^\circ$ C ,t_H, T_{an}, t_{an}
S16	3	1.062	4.2	$T_H = 600^\circ$ C, t_H, T_{an}, t_{an}
S17	3	0.679	5.8	$T_H = 700^\circ$ C, t_H, T_{an}, t_{an}

Optical absorption measurements were accomplished in samples LD, MD(see Table 3.3) in order to identify several contributions of $CuCl$ in $NaCl$. The absorption spectrum is decomposed into two contributions as illustrated in Fig. 3.13.

I) crystalline or nanocrystal line signature of $CuCl$ are characterized by two exciton resonance lines Z_3 and $Z_{1,2}$ and the absorption coefficient will be abbreviated as α_{exc},

II) Cu^+ ions contribution in spectra. The absorption coefficient is abbreviated as α_{ion} [Fus69].

The absorption measurements were carried out between 20 K and 300 K, in 20 K steps. Optical absorption spectra are recorded in a large range of wavelenghts, including the crystalline CuCl contributions and the noncrystalline part Cu^+ ions [HW98, Fus69], corresponding to (3 - 6) eV photon energy range.

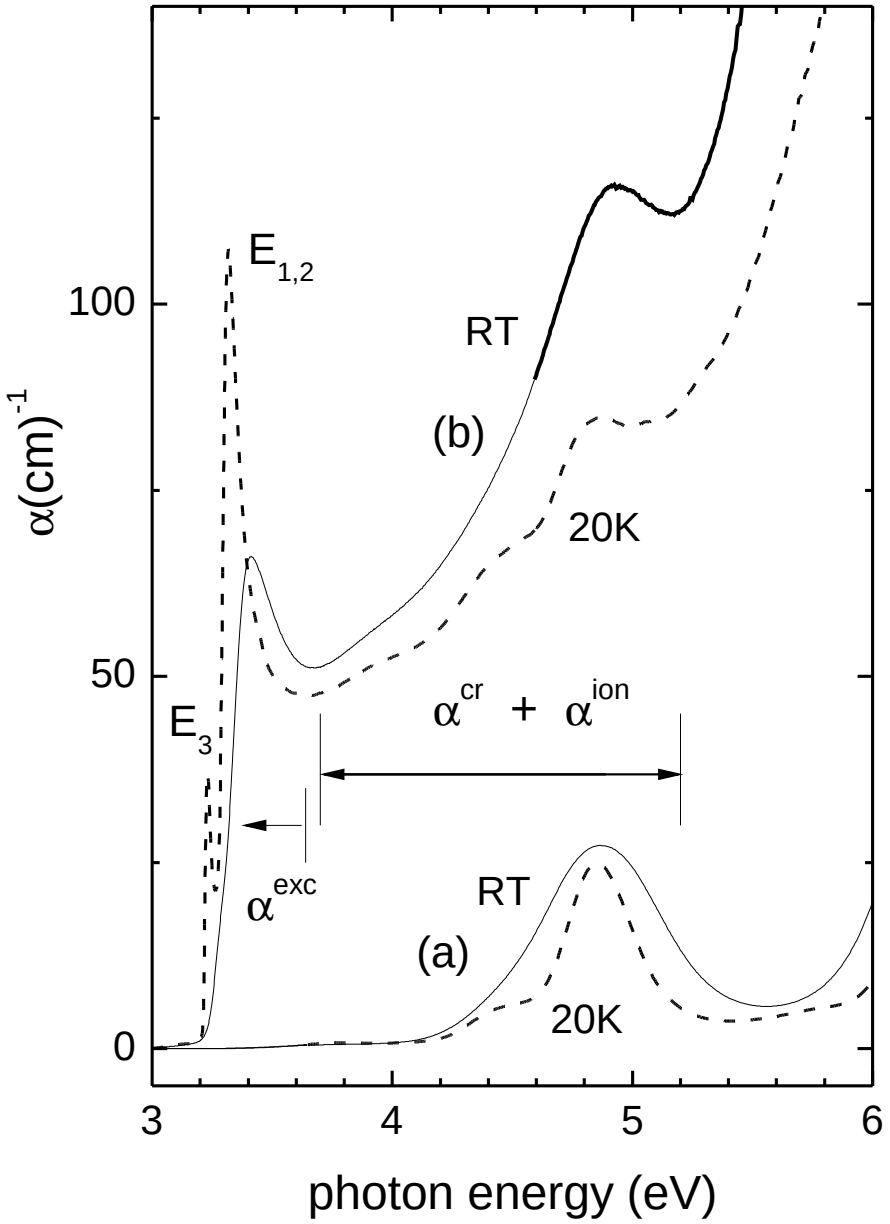

Figure 3.13: Absorption spectra of (a) sample LD and (b) sample MD2 recorded at room temperature and at 20 K.

As illustrated by the spectra of sample MD2(b) in Fig. 3.13, the existence of crystalline CuCl molecules is demonstrated by two spectral contributions.

I.) Two exciton peaks Z_3 and $Z_{1,2}$ for $E < 3.6$ eV, show a strong narrowing at low temperature. Horizontal arrows depicted in Fig. 3.13) indicate the spectral ranges which have been used to determine the oscillator strength of the excitons α^{exc} and of the inter-band transitions in crystalline CuCl, abbreviated as α^{ion}. The mean radius of the embedded nanocrystals is determined as $r_{20}^{MD2} = 2.8\,\text{nm}$ in sample MD2 at 20 K. The integrated absorption for the exciton component is described by:

$$\alpha^{exc} = \int_3^{3.6} \alpha(E)dE, \tag{3.11}$$

which is proportional to α^{cr}. It is used to determine the concentration x_{cr} of CuCl nanocrystals as $4.2 \cdot 10^{-4}$ in sample MD2. In sample LD the crystalline component is absent.

II.) Continuum absorption measured in the photon energy range $3.7\,\text{eV} < \text{E} < 5.2\,\text{eV}$. The component α^{cr} is superimposed by the absorption of the residual Cu^+ in the NaCl matrix. Using the results obtained in CuCl films deposited on different substrate types [KK71, RMGN67, GRC$^+$98], the integrated absorption is giving by:

$$\alpha^{ion} = \int_{3.7}^{5.2} \alpha dE \tag{3.12}$$

The ionic contribution is $x_{ion} = 5 \cdot 10^{-4}$ in sample MD2 and $x_{ion} = 1.7 \cdot 10^{-4}$ in sample LD, respectively. The total copper amount is $x = 9.2 \cdot 10^{-4}$ in sample MD2.

The broad bands at the photon energy $E_D = 4.85\,\text{eV}$ together with the more narrow ones at 4.4 eV are due to Cu^+ ions in an octahedral crystal field [Fus69, Dul69, PGM84]. The oscillator strength increases with temperature and indicates the influence of odd displacements by phonons. The CuCl concentration in sample LD is so small that the material remains a homogeneous solid solution. Phase separation of the solid solution into a matrix and embedded nanocrystals appears if the CuCl concentration in the melt is about 0.04 and more.

3.3.1 Summary

Exciton Spectroscopy is a sensitive experimental technique, therefore it can be used in order to determine the CuCl crystalline state in the NaCl matrix. A common procedure to incorporate nanocrystals into the matrix consists of heating as-grown crystals at different temperatures until the whole copper exists in the form of Cu^+ ions. Obviously, it is assumed that the ions are statistically distributed at octahedral positions of Na^+ in the NaCl structure. In the photon energy range between 3 eV and 5.2 eV several exciton lines are detected. The exciton lines reflect different signatures of crystalline CuCl molecules in NaCl matrix. The absorption spectra on CuCl:NaCl can be decomposed in two different contributions. The first part is due to CuCl nanocrystals incorporated in the CuCl matrix and the second part represents the Cu^+ ion signature.

The characteristic features in the optical absorption spectra are two exciton resonance lines Z_3 and $Z_{1,2}$ close to 3 eV. These lines stem from CuCl nanocrystals embedded in the NaCl matrix. In contrast to bulk CuCl, the excitons are shifted towards higher energy due to the small size effect of the absorbing nanocrystals. In the exciton spectra a broadening due to the size distribution effect can be observed. The spectral positions E_3 and $E_{1,2}$ show a dependence on the temperature and on the size of the nanocrystals. The central position of Z_3 exciton line is used for determination of the mean radius of the nanocrystals embedded in NaCl, according to Eq. 1.16.

3.4 Anomalies at and below T = 100 K

3.4.1 Phenomenon

The solid green line in Fig. 3.14 represents the reference data in CuCl films deposed on vitreous substrates. They are obtained as a mean value E_3 by collecting data from different sources [KK71, RMGN67, GRC+98]. Notice, that the straight green line is fitted for the temperature range between 25 K and 175 K.

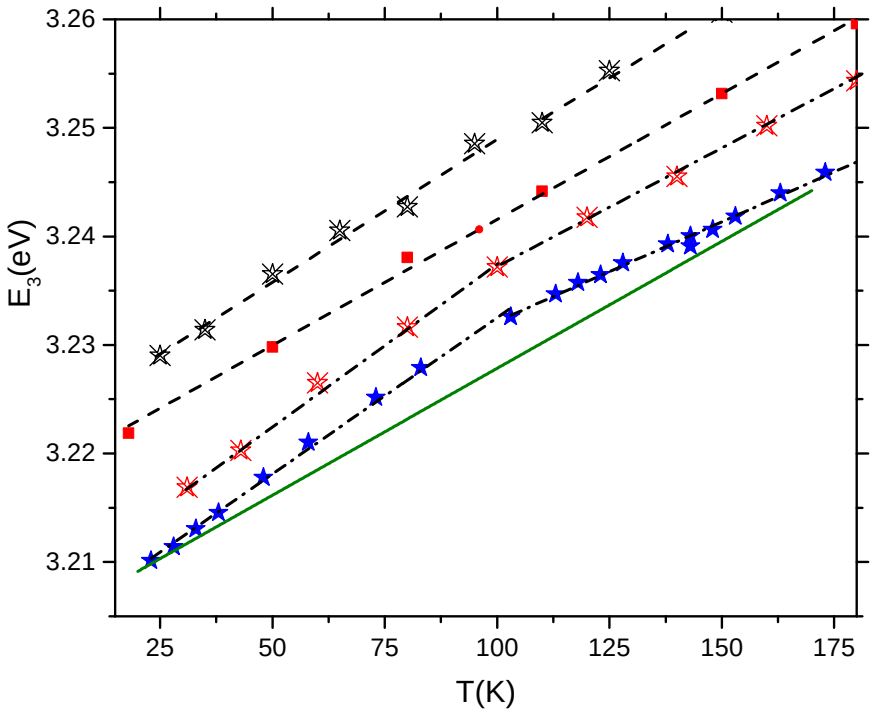

Figure 3.14: Spectral positions of the Z_3 exciton line as a function of temperature. Sample S11 (solid red squares). Sample S10 (solid blue stars). Sample S13 (black open stars). Sample S17 (red bar stars). Additionally, (solid green line) describes the reference data [KK71, RMGN67, GRC+98].

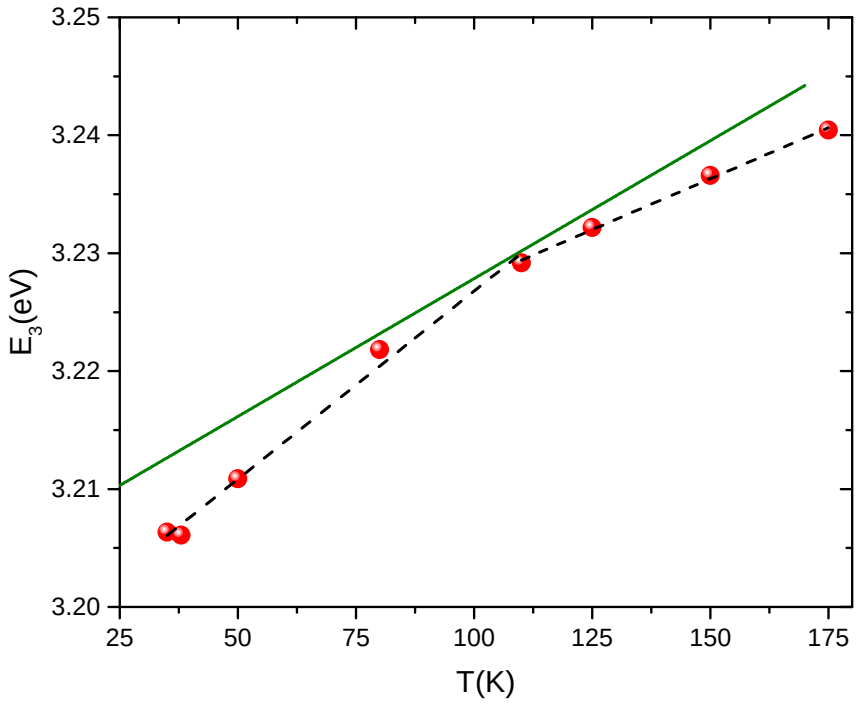

Figure 3.15: Spectral positions of the Z_3 exciton line in CuCl:KCl as a function of temperature. Solid green line represents literature data, in CuCl films deposed on quartz substrate [KK71, GRC$^+$98].

In Sample S11, the exciton resonance line of Z_3 is shifted to higher photon energy (see Fig. 3.14 - red squares). The shift of the resonance lines of Z_3, and of $Z_{1,2}$, to higher photon energy is appointed to the quantum confinement effect, and this reflects the effect of small nanocrystals. It is observed, that the size of the nanocrystals in sample S11 is smaller compared to the size of the nanocrystals embedded in sample S10. Nevertheless, the reference data shows that the position of the resonance line E_3 describes a linear dependence with increasing temperature [KK71]. However, a constant slope in the whole range is also demonstrated by the samples S10 (blue solid stars) and S11 (red solid squares). The distance to the reference line (solid green line) is a measure of the size of nanocrystals. An anomalous effect is identified at T = 100 K. At this temperature the central position of the resonance line E_3 changes the slope with increase of the temperature. This discontinuity is observed in the samples S17, S10 and also in KCl as illustrated in Fig. 3.15.

By a direct comparison between the reference data, the slope is found as $\left(\frac{\partial E_3}{\partial T}\right) = 2.34 \cdot 10^{-4}$ eV/K (solid green line)[KK71, GRC$^+$98] and the experimental results (blue dash line) indicates $\left(\frac{\partial E_3}{\partial T}\right) = 2.88 \cdot 10^{-4}$ eV/K. In the second temperature range 100 K and 175 K the slope is found to be $\left(\frac{\partial E_3}{\partial T}\right) = 1.84 \cdot 10^{-4}$ eV/K. The discontinuity of the slope $\left(\frac{\partial E_3}{\partial T}\right)$ is preferred by the large nanocrystals.

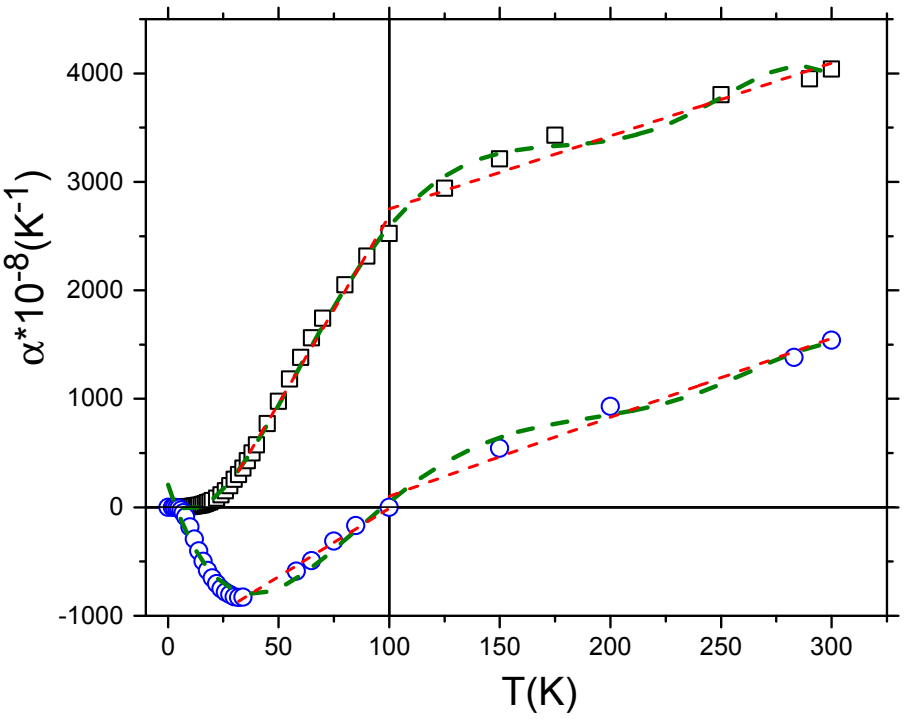

Figure 3.16: Thermal expansion $\alpha(K^{-1})$ as a function of temperature. Pure NaCl data (open squares) have been taken from literature [MG65]. Pure CuCl data (open circles) have been collected from literature [BBW77, SBS79] .

In general, it is expected that the radius of the nanocrystals can be influenced by the quantum confinement effect and that there is no impact of the thermal behavior of the CuCl nanocrystal temperature. This is considered to reflect the variation of the band gap energy. The situation in CuCl:NaCl is even more complex.

Usually, at ambient conditions the lattice parameters of the nanocrystals and the matrix are related by the ratio $\left(\frac{a_{CuCl}}{a_{NaCl}}\right) = 0.901$. Specially in the cooling process of a CuCl:NaCl sample the radius R_0 of the nanocrystal as well as the volume of the matrix shrink. As illustrated by Fig. 3.16, the thermal expansion of NaCl and CuCl differ strongly. In particular the zero value of α for CuCl points towards the discontinuity of the slope $\left(\frac{\partial E_3}{\partial T}\right)$ in Fig. 3.14.

3.4.2 An elastic model–part 2

CuCl is a semiconductor with a large amount of anomalous proprerties which are not well understood. This is true for details of its crystallographic structure in particular below 100 K. There is a general agreement that the anomalies originate from structural disorder which is stronger and more static at low temperature and becomes dynamical with increasing temperature. Theorists have pointed out two different schemes which are

involved in the structural disorder. These are the anharmonic coupling of phonons and off-center positions of Cu along the [111] axis [MTK03, PC96, WYK94].

The straight green line $E_3(T)$ in Fig.3.14 indicates that structural disorder is absent in embedded CuCl nanocrystals, which is not surprising due to their small volume. Even more, the good agreement of the exciton spectrum of CuCl:NaCl with that of bulk CuCl suggests the existence of well-developed properties of pure CuCl crystals. A property of this kind is the thermal expansion α. The change of sign at 100 K without a discontinuity indicates a significant but not necessarily a strong change of the CuCl structure. In CuCl:NaCl, the change of $\left(\frac{\partial E_3}{\partial T}\right)$ at 100 K is small but discontinuous. The question arises whether the different thermal expansions lead to an interaction between nanocrystals and the matrix. In order to study this problem it is assumed that a sample can be divided into spheres which consist of a spherical nanocrystal of mean size at its centre and the corresponding NaCl fills the volume of the sphere with exception of a small gap between nanocrystals and matrix which corresponds to the lattice mismatch. For the sake of simplicity the excess NaCl between the spheres is neglected. R_α and R_0 are connected by the concentration of CuCl molecules in the crystalline state as already shown above in Eq. 3.6.

The used radii are defined in Fig. 3.17.

The unit cells of CuCl and NaCl are oriented parallel to each other as is well known from a two-photon absorption experiment [FHR95]. The maximal value for the gap at room temperature is giving by:

$$\Delta R \;=\; R_0^M - R_0^{NC} \;=\; 0.041 \cdot R_0^{NC}. \tag{3.13}$$

In the following the effect of thermal expansion is consideredfor the cooling procedure, and this starts at 300 K. As shown in Fig. 3.16 the most important thermal expansion happens by NaCl which in addition occupies the largest volume. Thus, for the first step from 300 K to 175 K the influence of CuCl can be neglected. The change of volume is given by:

$$\Delta V \;=\; V^* - V_0 \;=\; -\,3 \cdot V_0 \cdot \alpha \cdot \Delta T, \tag{3.14}$$

where α denotes the linear thermal expansion and $V_0 \;=\; \frac{4}{3} \cdot \pi \cdot \left(R_\alpha^3 - (R_0^M)^3\right)$ is the volume of the matrix at 300 K before elastic relaxation appears. The negative sign on the right of Eq. 3.14 takes into account the cooling process. For 175 K the matrix volume is described by V^* and the relevant radii are R_α^* and R_0^{M*}. Taking into account changes of the boundaries by introducing the changes ΔR_i and Eq. 3.14 for NaCl may be written as below:

$$3 \cdot R_\alpha^2 \cdot (\Delta R_\alpha + \alpha \cdot \Delta T \cdot R_\alpha) - 3\left(R_0^M\right)^2 \cdot \left(\Delta R_0^M + \alpha \cdot \Delta T \cdot \left(R_0^M\right)\right) \;=\; 0. \tag{3.15}$$

Assuming a model - nanocrystal for $x_{cr} \;=\; 4 \cdot 10^{-4}$ and $R_0 \;=\; 5\,\text{nm}$, Eq. 3.13 and 3.15 yield $R_\alpha \;=\; 67.9\,\text{nm}$ and $\Delta R \;=\; 0.205\,\text{nm}$ at room temperature.

For 175 K a trivial solution of Eq. 3.15 are obtained if both terms vanish which yields at $\Delta R_\alpha \;=\; -\,0.317\,\text{nm}$ and the value of ΔR_0^M remains an open question because of

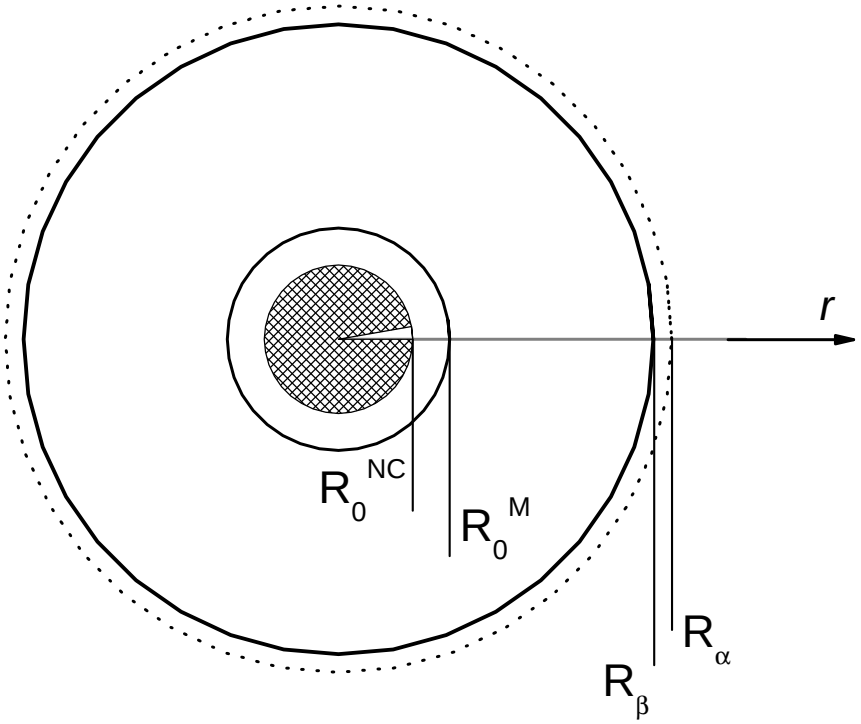

Figure 3.17: Model of a finite nanocrysal-matrix system before elastic relaxation: R_0^{NC} radius of the nanocrystal; R_0^M inner radius of the matrix; R_α outer radius of the matrix. After relaxation the interfacial gap vanishes and R_α reduces to R_β.

reasons discussed later. For the contraction of the nanocrystal one obtains $\Delta R_0^{NC} = -0.0071\,\text{nm}$. Obviously, the neglect of thermal contraction of the nanocrystal is justified. The contraction of the matrix signalizes enough potential for the thermal expansion to close the gap ΔR without any support by another force. However, such a force is obviously existing. Experimental proofs for the collective internal stress fields at room temperature are the birefringence of Fig. 3.11 and the contraction of the NaCl lattice parameter in Fig. 3.7. The latter effect demonstrates the existence of an internal stress field of (-2.3) MPa for $x_{cr} = 4 \cdot 10^{-4}$.

As demonstrated in Fig. 3.14 the E_3-position in sample S10 coincides with the bulk value. It is assumed that in this case no external forces act on the nanocrystals. Thus, 175 K can be used as an elastically neutral reference point. Two-photon absorption measurements did show an increase of E_3 by 7.65 meV/GPa[Ro94]. Using this relationship, the discontinuity of the blue-shift at 100 K represents a pressure of 0.63 GPa. Summarizing the above considerations one has to conclude that two different types of forces drive structural changes during cooling from 300 K to 175 K. Fig. 3.15 supports this interpretation. In KCl the misfit between CuCl and KCl is much bigger than in NaCl . As a consequence the gap is bigger in KCl and it is more difficult to close it completely in KCl. In Fig. 3.15

the photon energy E_3 of the CuCl exciton in KCl is smaller compared to bulk value.

Summarizing the above considerations one has to conclude that two different types of forces drive structural changes during the cooling process:

(I.) Contractive radial forces between nanocrystal and matrix which originate mainly in the common substructure of the anions. One may call them "anion-forces".

(II.) "Thermal forces" which are responsible for thermal expansion.

Most likely, during cooling both mechanisms operate simultaneously in the sense of a mutual support of effective structural displacements. Fig. 3.15 supports this interpretation. In KCl the misfit between CuCl and KCl is much bigger than in NaCl. Thus, as a consequence the gap is bigger in KCl and it is more difficult to close it completely in KCl. In Fig. 3.15, E_3 of the CuCl exciton in KCl is smaller than the bulk value. This red shift needs the impact of a positive stress on the nanocrystal. Following the prediction of the elastic-domain model which has been already introduced in Section: 3.1.3, such a tension on the nanocrystal is produced when the anion forces close the gap [FHR95].

Let us assume that for sample S10 at 175 the anion-forces and the thermal forces are in structural equilibrium. This means that with respect to both operating mechanisms no further structural displacements are needed. However, cooling is continued and the deviation of E_3 of sample S10 with a blue-shift needs a more quantitative consideration of the mutual interaction between the two mechanisms. Nevertheless, before this will be done three further examples of low-temperature measurements are presented. The results are so strong that without the operation of two types of forces a reliable interpretation seems to be impossible.

3.4.3 [110] edge directions in doped NaCl

A single crystal of doped NaCl has been used to prepare four different samples S6, S7, S8, S9. Samples S6 and S7 have been prepared with 100 faces and samples S8 and S9 with $(110)(\bar{1}10)$ faces. The experiment has been performed using a two-sample holder. Obviously, this procedure avoids as far as possible temperature gradients between the two samples.

At T = 37 K the resonance lines have been fitted by Gaussian functions. The positions of the exciton lines $E_3^{S6} = 3.21904\,\text{eV}$ and $E_3^{S7} = 3.2189\,\text{eV}$ have been determined. At this temperature the mean radii of the nanocrystals are found to be $r_{S6} = 5.37\,\text{nm}$ and $r_{S7} = 5.4\,\text{nm}$. The slope $\left(\frac{\partial E_3}{\partial T}\right) = 2.64 \cdot 10^{-4}(5.2 \cdot 10^{-6})\,\text{eV/K}$ in sample S6 and S7 between 37 K and 180 K has been determined. Samples S8 and S9 have been prepared with [110] edge direction and orientations in sample. The experiment in S8 and S9 has been performed respecting the same condition such as in the previous one.

At low temperature T = 52 K the positions of the exciton line $E_3 = 3.21823\,\text{eV}$ and the size of the nanocrystals $r = 16\,\text{nm}$ are determined. In S8 and S9 a discontinuity at T=100 K of the exciton positions is observed, thus two ranges with different slopes can be distinguished. Below 100 K, the slope is determined as $\left(\frac{\partial E_3}{\partial T}\right) = 3.86 \cdot 10^{-4}$ $(1.6 \cdot 10^{-5})\,\text{eV/K}$, and between 100 K and 180 K the slope is described as $\left(\frac{\partial E_3}{\partial T}\right) = 2.43 \cdot 10^{-4}(6.5 \cdot 10^{-6})\,\text{eV/K}$.

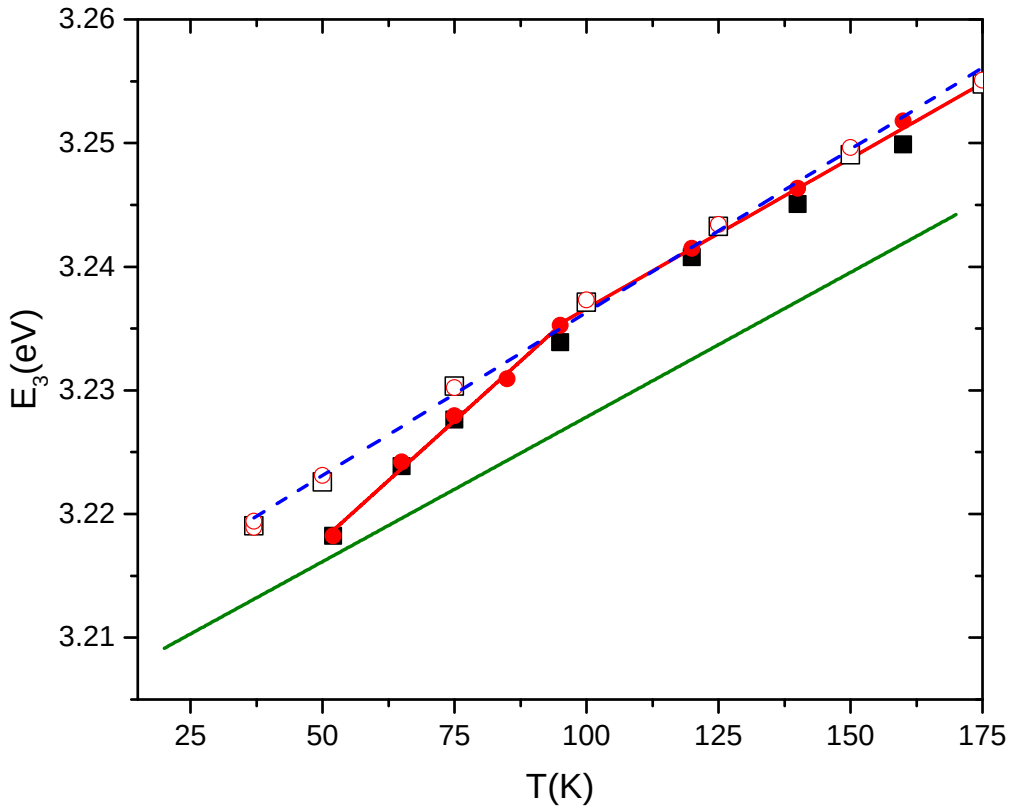

Figure 3.18: Spectral positions E_3 at different temperatures. Solid black squares-sample S8. Sample S9 (solid red circles).Sample S6 (open black squares).Sample S7 (open red circles). Notice, that the straight green line represents literature data [KK71, RMGN67, GRC$^+$98]

Nearly no differences have been observed for both samples (see Table 3.3). The size of the CuCl nanocrystals in samples S8, S9 have been found to be rather different compared to the nanocrystals embedded in samples S6, S7: as $r^{S8,S9} \gg r^{S6,S7}$

Figure 3.18 shows for each temperature above T = 100 K practically the same E_3-values for all four crystals. Below T = 100 K, $E_3(T)$ is strongly anisotropic. It is rather improbable that this anisotropy is related directly to a typical exciton parameter. Notice, that below 100 K the exciton linewidth is the same for both directions of the lightwave(see Fig. 3.19). Another way to introduce anisotropy is a direct stress. To produce at 50 K the red-shift which is demonstrated in Fig. 3.18 between [100] and [110] a tension of 0.64 GPa is needed. Such an effect is easily possible if a direct axial connection between nanocrystal and matrix exists. It is observed in Fig. 3.19, that the usual linear dependence of the linewidth of T^2 above T = 200 K in samples with (110) faces is not respected [KK71].

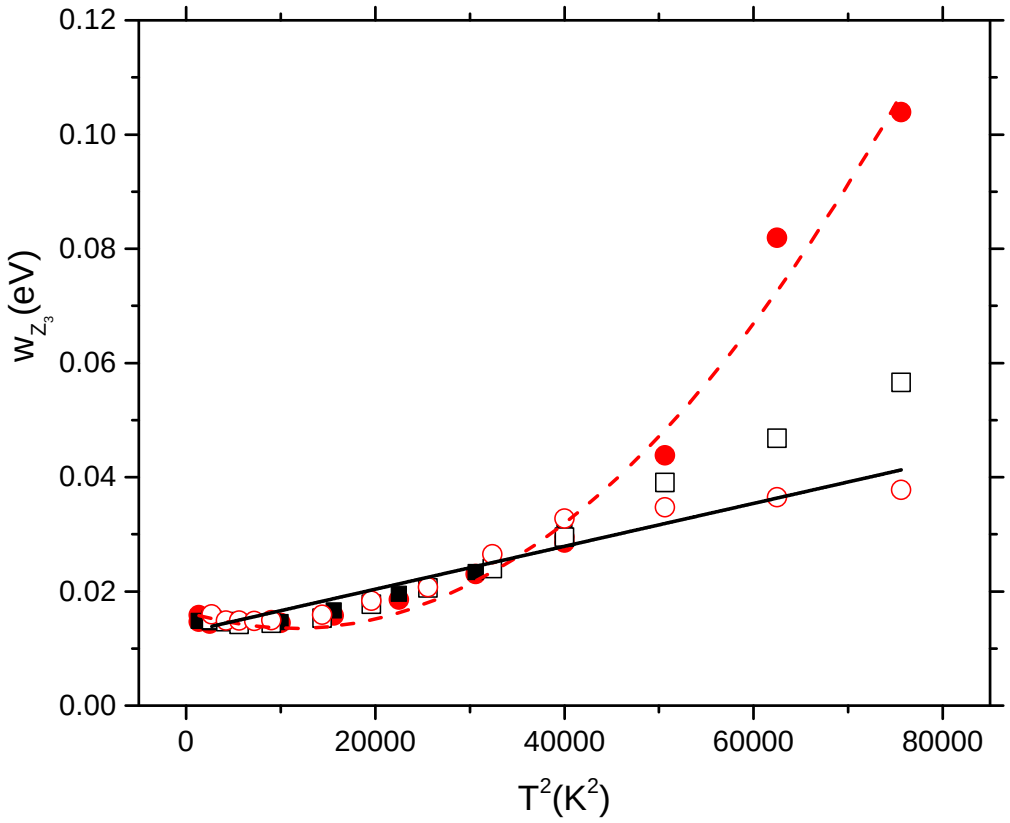

Figure 3.19: The linewidth of exciton resonance lines Z_3 in samples S6, S7, S8 and S9 as a function of T^2.

3.4.4 Step-wise temperature dependence

A thin rectangular plate is prepared from a single crystal of CuCl doped NaCl(see Table 3.3). This sample will be called S12. A thermal treatment at T = 112° C is applied for 24 hours. The blue-shift in CuCl:NaCl is used to determine at T = 20 K the size of the CuCl nanocrystals to be $r_{12} = 7.3$ nm.

Figure 3.20 demonstrates an anomalous expanding effect from the E_3 positions. They do not respect a linear increase but a step-wise one. In the case of Fig. 3.20 it seems to be natural to consider the effect with increasing temperature. The sign and the magnitude of the total thermal effect is used similar to the result of Fig. 3.18 and of the Sample S10 in Fig. 3.14. The existence of two types of mechanisms is obvious for Fig. 3.20. Most likely, at temperatures which are connected by solid lines thermal expansion is acting. The accompanying structural changes produce internal stress which in turn changes E_3. Thus, the stresses are pressure on heating and tension on cooling. The gaps between nanocrystals and matrix are used by the anion-forces to optimize the stress fields.

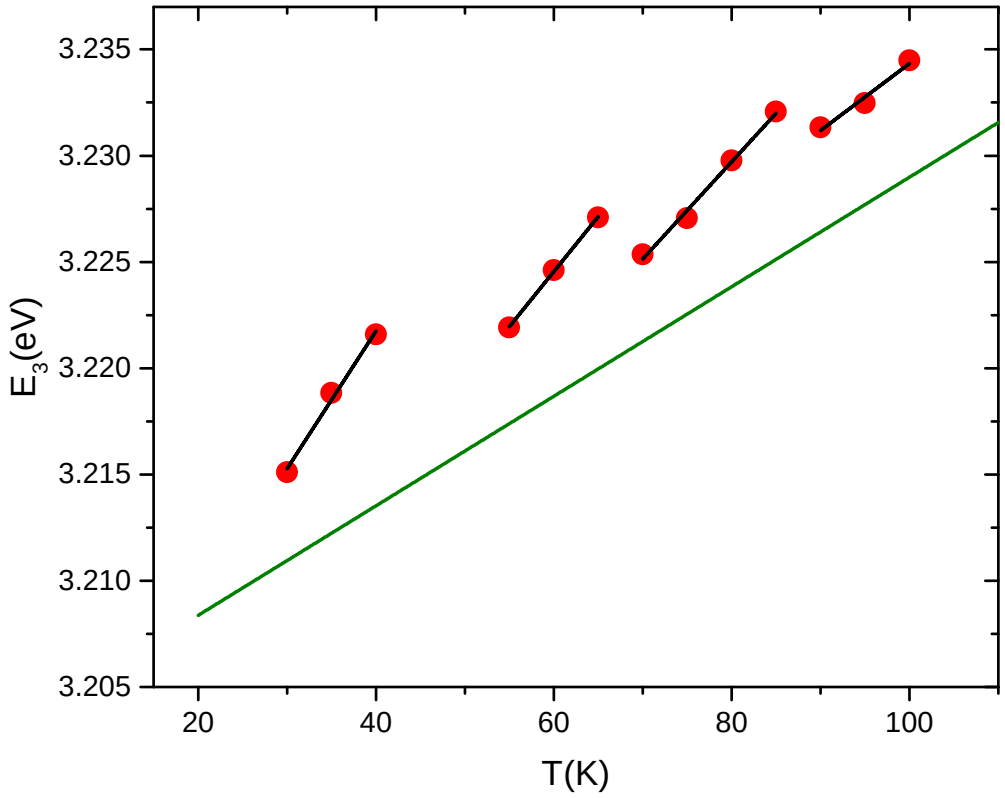

Figure 3.20: Spectral position of $Z3$ exciton as a function of temperature in sample S12.

3.4.5 Thickness effect at low temperature

An optical experiment was accomplished in a thin sample. In this experiment the morphology of the surface is considered to be a source of an anomalous effect observed at low temperature in optical measurements. A thin sample was prepared from a single crystal of CuCl:NaCl. Optical absorption measurements were carried out between 20 K and 300 K and the experimental results are presented in Table 3.4.

The nomenclature used in the experiment is described as: sample S (black triangles), sample Sa (red triangles), sample Sb (green circles) and sample Sc (blue stars) (see Fig. 3.21). The optical experiment starts with a thin plate of CuCl:NaCl sample S and this is the original sample. At low temperature T = 30 K the exciton positions of Z_3 and $Z_{1,2}$ in sample S and the mean radius of the nanocrystals r = 2.5 nm are determined. A thickness reduction is performed from d = 280 μm to d = 175 μm. The central positions of the exciton resonance lines Z_3 do not change and also the new size of the nanocrystals r = 2.24 nm is nearly the same as before. A second thickness reduction is achieved from 175 μm to 120 μm. Here a shift in the resonance lines has been detected from 3.2392 eV to 3.226 eV, and the size of the nanocrystals is r = 3.23 nm. A final thickness reduction to 85 μm shifted the E_3 energy position only marginally. Due to the quantum-confinement

Table 3.4: Characterization of samples. First column: name of samples—S, Sa, Sb, and Sc. Second column: the thickness of the samples a$d[\mu m]$. Third column: the size of the nanocrystals $r[nm]$. Fourth column: the position of the first resonance line—E_3 [eV]. Fifth column: position of the second exciton peak—$E_{1,2}$ [eV]. Sixth column: $\Delta E = E_{1,2} - E_3$ [eV].

Sample	**d** $[\mu m]$	**r [nm]**	E_3 **[eV]**	$E_{1,2}$ **[eV]**	$\Delta E = E_{1,2} - E_3$ **[eV]**
S	280	2.5	3.2385	3.3248	0.0863
Sa	175	2.24	3.2423	3.3300	0.0877
Sb	120	3.23	3.2272 - redshift	3.3100	0.0828
Sc	85	3.4	3.22605 - redshift	3.30811	0.08206

effect the exciton lines are shifted to higher photon energies. Usually, a blue-shift with decreasing size of the nanocrystals can be observed. A blue-shift can be produced by the small sizes effect but can be also a pressure effect [Ro94]. Figure 3.21 shows a red-shift during the thickness reduction procedures. The difference between the position of Z_3 exciton lines before and after the second thickness reduction is $\Delta E_3 = 0.0132\,\text{eV}$. This corresponds to a hydrostatic pressure of 1.2 GPa but with opposite sign [Ro94].

Figure 3.22 shows the positions of Z_3 as a function of temperature after each thickness reduction procedure: S $\rightarrow$ Sa $\rightarrow$ Sb $\rightarrow$ Sc. The exciton line Z_3 in sample S and Sa after the first reduction of the sample thickness indicate nearly the same value 3.22). The resonance line E_3 after second thickness reduction is shifted to lower photon energy and the same effect is observed in the last sample Sc. The orange squares describe the position of Z_3 in bulk CuCl combined with optical absorption in CuCl films deposited on fused quartz substrates. A shift of the exciton lines towards low photon energy occurs due to large nanocrystals embedded in the matrix. The blue curve shows the exciton spectra after the last thickness reduction (sample Sc), the exciton lines are shifted in the same direction as in the previous sample Sb, at T = 30 K. The size of the nanocrystals r = 3.4 nm is determined.

Figure 3.22 illustrates the basic stress effect according to the elastic domain model. Due to this model internal stress is produced by the attraction between nanocrystal and matrix which applies a tension on each nanocrystal. In first approximation the local forces are added and the result is divided by the area perpendicular to the three surface normals. Thus, the global tensional stress components parallel to the plate increase by reduction of its thickness which in turn produces a red-shift of the exciton.

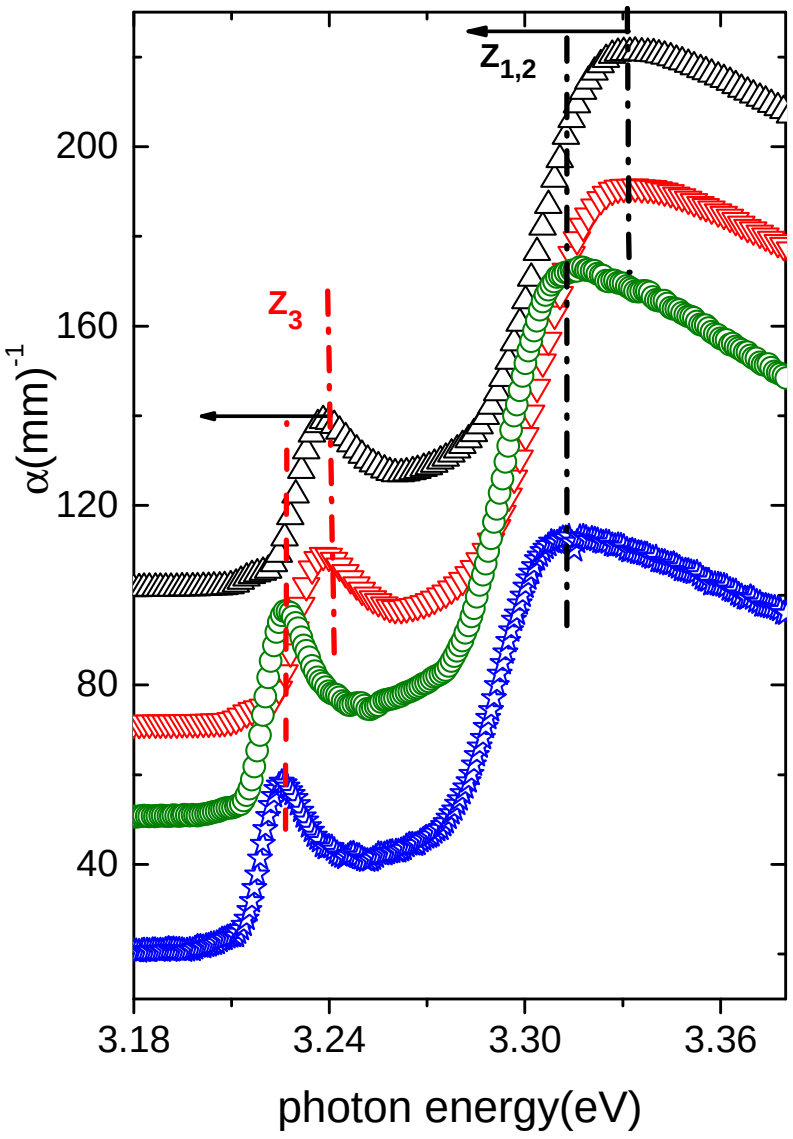

Figure 3.21: Absorption spectra of NaCl containing CuCl nanocrystals at 30 K in S, Sa, Sb, Sc
[WKLPV05].

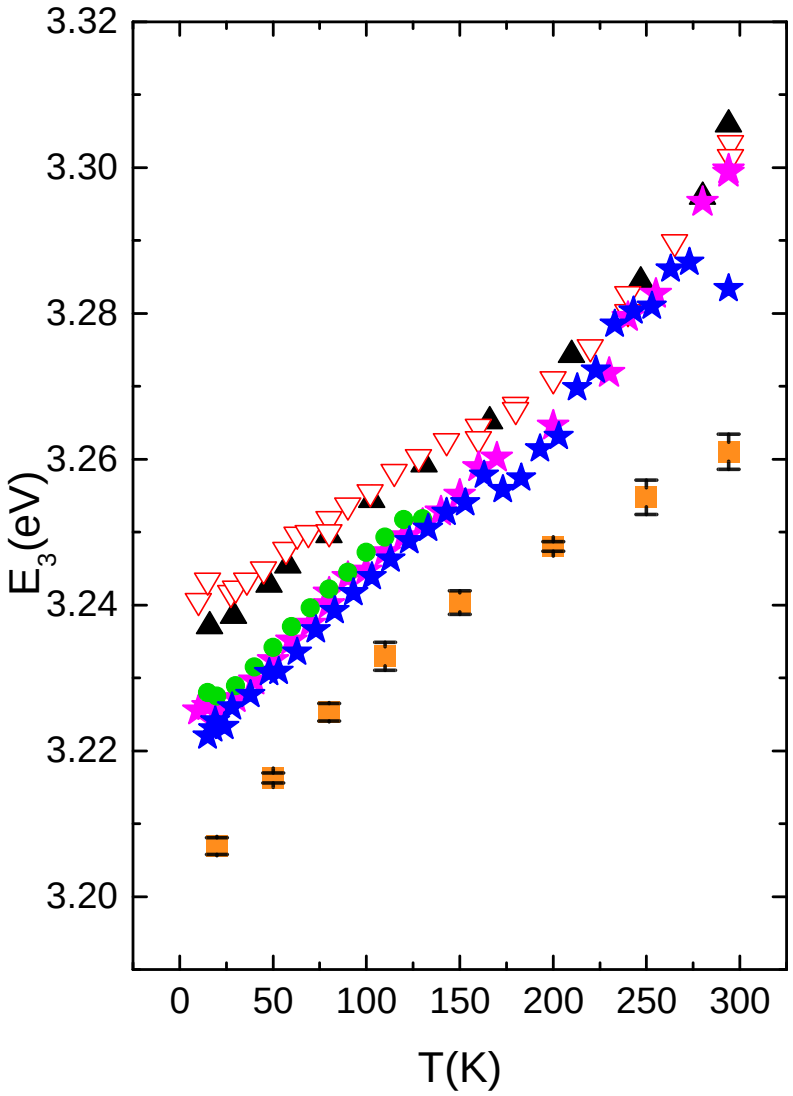

Figure 3.22: Spectral position of Z_3 exciton in different samples S, Sa, Sb and Sc as a function of temperature in the thickness reduction procedure. Orange squares give the reference data combined with data from a CuCl film deposed on fused quartz.

3.5 Elastic fluid

In the CuCl:NaCl system, the small concentration and the small sizes of the nanocrystals make difficult the detection of the elastic interaction between CuCl nanocrystals and NaCl matrix. Evidence for elastic interaction between CuCl nanocrystals and NaCl matrix have been obtained by Resonant-Ultrasound-Spectroscopy (RUS) measurements [WSPV04]. RUS probes the mechanical resonance of a rectangular sample. Those experiments also revealed the influence of sample imperfections which even may prevent the evaluation of reliable results.

The elastic measurements have been performed for two samples with different thermal history. The first sample S1 was heated to 650 K, then it was annealed for 48 hours at 376 K. The second sample S2 had no thermal treatment. Optical measurements approved the absence of the CuCl in crystalline state. An important result is the observation of real elastic anomalies in comparison to the elasticity of pure NaCl. Roughly speaking, the elastic constants of pure CuCl were observed.

As demonstrated in Fig. 3.23 and in Fig. 3.24, the elastic constants Δc_{11} and Δc_{12} show a statistical scattering. Nevertheless, in S2 sample (see Fig. 3.24) these fluctuations Δc_{11} and Δc_{12} are stronger compared to the S1 values (see Fig. 3.23). Δc_{ij} denote the differences between the experimental values of the doped material and the values of pure $NaCl$ taken from literature [YOA87], $\Delta c_{ij} = c_{ij}^{experimental}$ - $c_{ij}^{reference}$. The temperature dependence of the elastic constants show that the effect which produces the fluctuations of the elastic constants is similar in Δc_{11} and Δc_{12}. Δc_{44} is approximately equal to zero in the whole temperature range, thus the effect is absent. This type of symmetry where the elastic constant are identical describes fluid media or "elastic - fluid".

The difference $\Delta c = \Delta c_{11}$ - Δc_{12} describes a clear linear dependence in both samples E1 (with thermal treatment) and E2 (without thermal treatment) above and below the critical temperature $T_c \approx 333$ K. In these differences, the contribution of an additional effect is absent. The different slopes above and below T_c indicate different states of the nanocrystals [WSPV04, WKLPV05]. For this experiment the linear dependence of Δc on temperature is of importance. In both samples the deviations from linearity are less than 0.05 GPa and this is just the limit of reliability of RUS [MS97]. Nevertheless, this difference demonstrates that the effect which causes the relatively strong variations is numerical equal in Δc_{11} and Δc_{12}. In addition, this effect is absent in Δc_{44}.

The existence of an "elastic - fluid" contribution is mainly restricted to the temperature range T $< T_c$ in sample S1 and to T $> T_c$ in sample S2. Sample S2 (see Fig. 3.24) shows a maximum at T_c which decreases rapidly with increasing temperature. It is difficult or even impossible to separate this effect quantitatively from contributions produced by individual defects of the sample. The changes of $\Delta(\Delta c) = \left(\frac{\partial \Delta c}{\partial T}\right) \cdot (T - T_c)$ with $\left(\frac{\partial \Delta c}{\partial T}\right) = -6.7 \cdot 10^{-3}$ GPa/K and $T_c = 330$ K in sample S1, and in sample S2 it is found to be $\left(\frac{\partial \Delta c}{\partial T}\right) = 7.1 \cdot 10^{-3}$ GPa/K and $T_c = 337$ K. For T $> T_c$ (see Fig. 3.23 and Fig. 3.24) two contributions are found, a negative one in sample S1 and a positive one in sample S2. The latter increases strongly nonlinearly with temperature. The negative

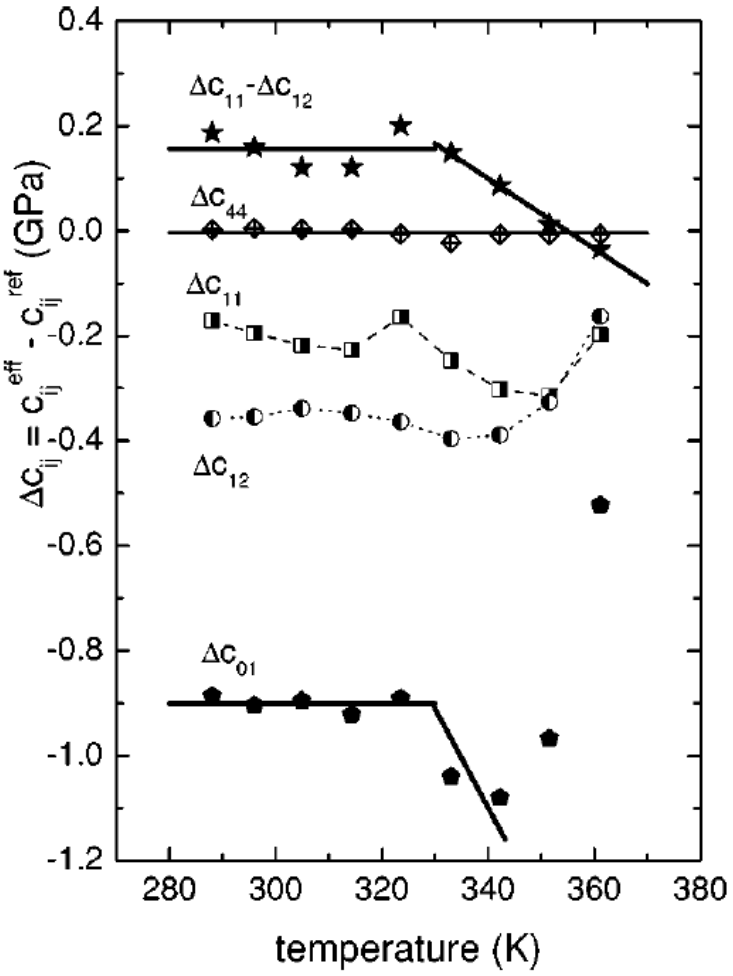

Figure 3.23: Difference of elastic constants as a function of temperature for sample S1. $\Delta c_{ij} = c_{ij}^{exp} - c_{ij}^{ref}$, the difference shows a linear dependence on temperature and the slope is changed at $T_c = 330\,\mathrm{K}$. (Squares) Δc_{11}, Δc_{12} (circles), Δc_{44} (diamonds), (stars) $\Delta c_{11} - \Delta c_{12}$, and ΔC_{01} (hexagons), according to [WSPV04].

contributions are approximated as $\left(\frac{\partial C_{01}}{\partial T}\right)$ = -0.016 GPa.

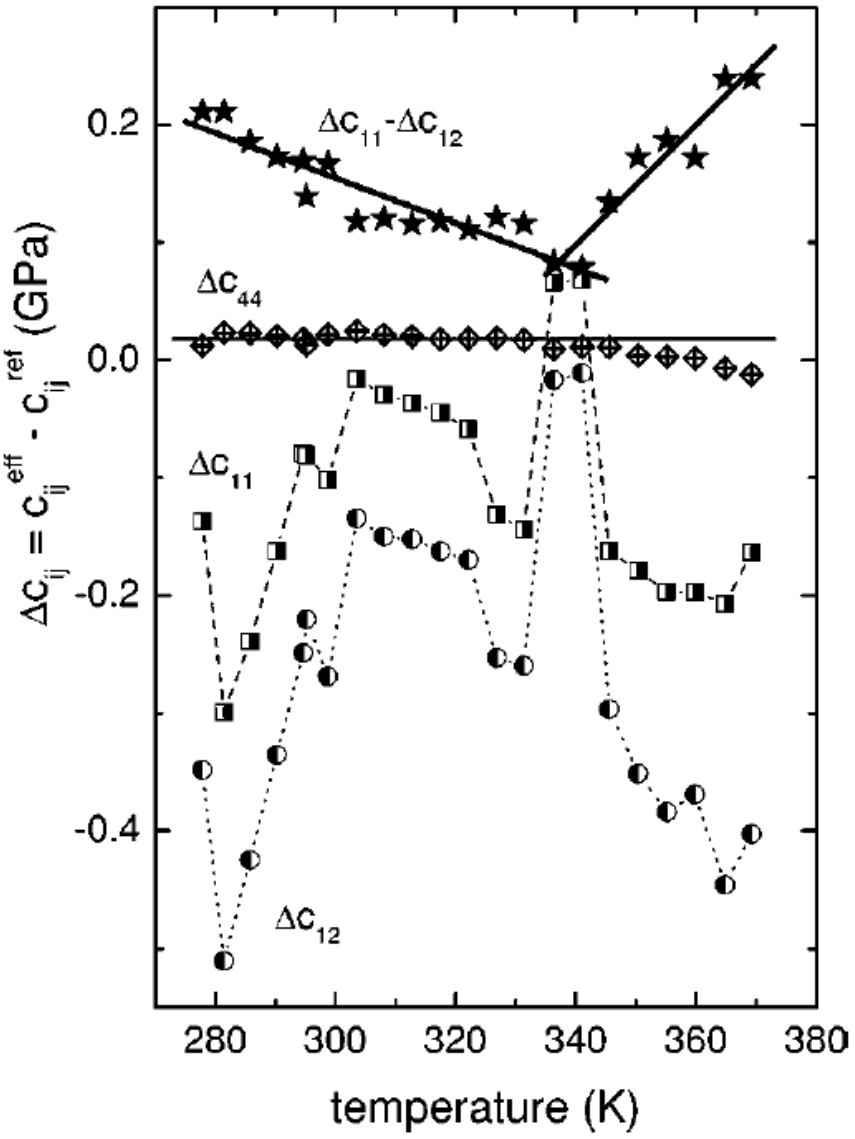

Figure 3.24: Difference of elastic constant as a function of temperature in sample S2. $\Delta c_{ij} = c_{ij}^{exp} - c_{ij}^{ref}$. The difference $\Delta c_{11} - \Delta c_{12}$ describes a linear dependence with a different slope below and above $T_c = 337\,\mathrm{K}$, according to [WSPV04].

3.5.1 Summary

Utilizing a thermal anomaly of CuCl:NaCl system at T$\approx$ 333 K it was possible to improve the reliability of the (RUS) to a level which enabled the detection of changes in the elastic interaction between CuCl nanocrystals and NaCl matrix, even for concentration of CuCl

smaller than $5 \cdot 10^{-4}$. Obviously, the results show the existence of an additional effect in CuCl:NaCl, this effect is absent in pure NaCl. This effect is related to a characteristic temperature T_c. Thus, in the new effect two different contributions in the elastic constants are included. The first one shows the signature of an elastic - fluid, this appears as a precursor effect indicating the imminent nucleation or dissolution of nanocrystals. The second one is a change of elastic constants above T_c.

3.6 Grains under pressure

The experiments on pure and doped KCl were carried out mainly for clarifying whether the anomalous effects observed in NaCl indicate a general or a singular phenomenon. As already mentioned above, the appearance of a birefringence frame as in CuCl:NaCl (see Fig. 3.10) was also observed in a big sample of CuCl:KCl. If an interaction between CuCl and KCl really exists there should exist also a contraction of the lattice parameter of KCl. Beside a pure KCl crystal four crystals with different CuCl concentration in the melt weren prepared by the Czochralski technique and the size difference between $Cu^+ < K^+$ is significantly bigger than expected for a less effective embedding of CuCl in KCl. A quantitative chemical analysis was renounced in favor of a wide CuCl amount in the melt of $0.8\%, 3\%, 6\%$ and 12%. The single crystals were reduced to grains in the same way as described for CuCl:NaCl. The first X-ray measurements were done by use of the high-sensitive apparatus of the Synchrotron of the University Dortmund. In contrast to the measurements on CuCl:NaCl no clear difference between pure and doped KCl was observed. A reason for bigger errors in KCl samples may be the missing differentiation between samples which contain arrested dislocations and which are seemingly free from these defects. External stress should be able to remove disorder of internal stress. Therefore, the influence of hydrostatic pressure has been tested by the Energy-Dispersive Powder Diffraction.

3.6.1 Pure and doped KCl

In the MAX80 system at HASYLAB-DESY, the grains fill a small vertical graphite tube. Usually, the graphite tube is divided into sub-volumina which are separated by a layer of Boron-Nitride between the upper and the lower part. The graphite tube is positioned just in the center of the six anvils (see Fig. 2.4). The anvils produce loads in steps of 1 t (ton). The local pressure is usually determined by filling one sub-volumina with NaCl as a reference material and scaling its strain-stress relation by use of Decker's Equation [Dec71]. Previously, it was demonstrated that this procedure works only approximately, even if the improved version of the equation is applied [WKLPV05]. A special problem is the reliable determination of the photon energy $E^*_{hkl}(0)$ of the (hkl) reflexes at the load F = 0(t). For a cubic crystal the definition of E^*_{hkl} is given by:

$$E^*_{hkl} = \frac{E}{(h^2 + k^2 + l^2)^{1/2}} \tag{3.16}$$

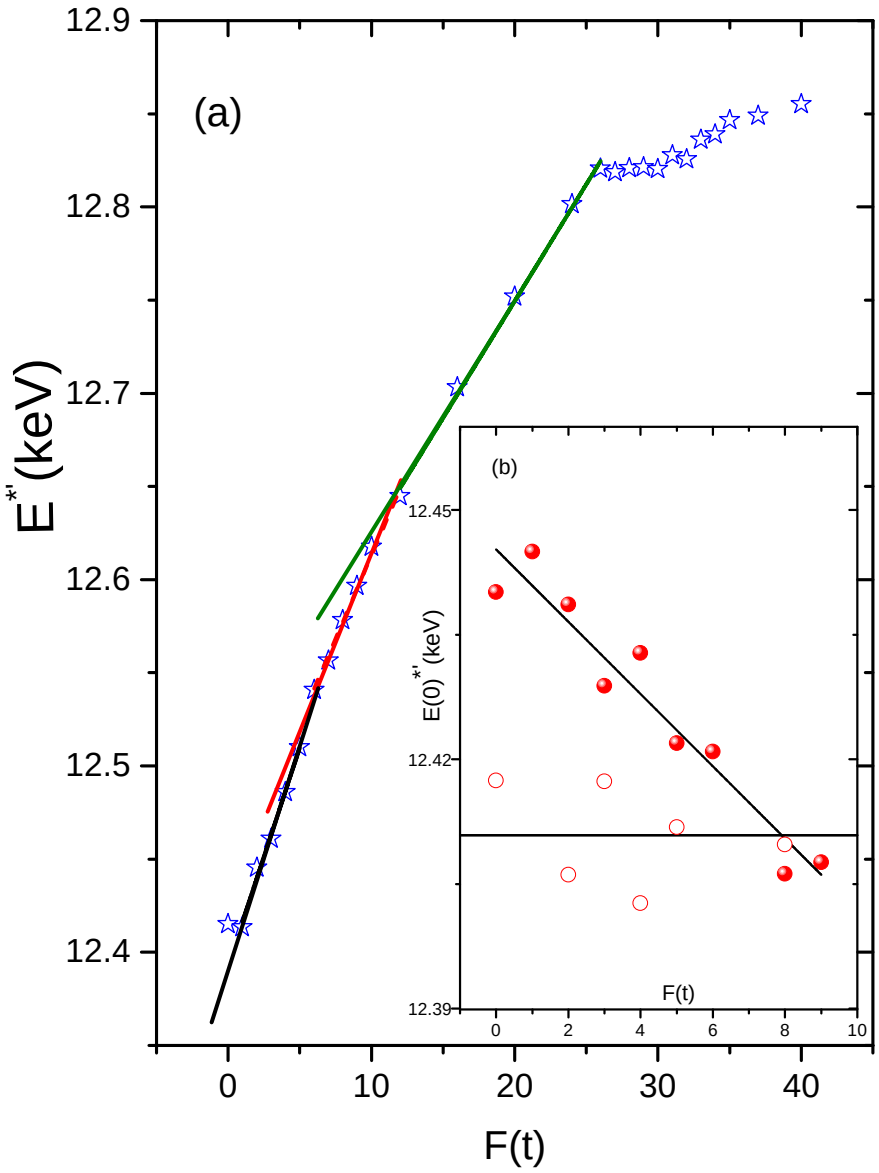

Figure 3.25: (a) Nominal diffraction energies as a function of F(t) in CuCl (12%):KCl (open stars).(b) Normalized diffraction energies as a function of F(t) in pure KCl (open spheres) and in CuCl (12%):KCl (solid circles). The results (see (a) fits) are split in three linear ranges.

Equation 3.16 describes the photon energy at which the reflection (hkl) appears in the energy spectrum.

In NaCl one observes, usually, a rather strong scattering for the first reflexes $E^*(0), ...,$ $E^*(F)$ in the first range of external forces between F = 0 (t) and F = 4 (t) or F = 5 (t).

With increasing F the data show a straight line which is extrapolated to F = 0 (t) to yield a reasonable value for $E^*(0)$. As illustrated in Fig. 3.25 the situation is a little bit different in KCl. Usually, two or sometimes three straight lines may be used for extrapolation. In addition the B1-B2 phase transition of KCl happens at comparatively low pressure. It is indicated in Fig. 3.25 by a sudden change of the slope at about F = 26 (t). One may speculate whether the line in front of 26 (t) indicates the correct strain-stress curve of the KCl rock-salt structure or whether it is an indicator of the following transition at F > 26 (t). The definition

$$S_0 \;=\; \frac{a_F}{a_0} - 1 \;=\; \frac{E^*(0)}{E^*(F)} - 1 \tag{3.17}$$

of the hydrostatic strain S_0 shows the importance of knowing the value for $E^*(0)$ as precisely as possible. On the other hand the present results show that the treatment of the material by preparing a grain sample is able to modify the lattice parameter, in particular of pure NaCl.

Also an alternative method of determining the value of $E^*(0)$ has been developed. One sub-volumen has been filled with KCl and the second one with pure NaCl. As in Eq. 3.17, a_0 and a_F represent the lattice parameters at ambient pressure and under load F. Corresponding notations are $E^*(0)$ and $E^*(F)$. Furthermore, in the following the notations: $(a^{'}, T^{'}, E^{'})$ and $(a^{''}, T^{''}, E^{''})$ are used for KCl and for NaCl, respectively. The lattice parameters are connected according to:

$$\frac{E^{*'}(0)}{E^{*''}(0)} \;=\; \frac{a_0^{(NaCl)}}{a_0^{(KCl)}} \;=\; \frac{a_0^{''}}{a_0^{'}} \text{ for } T_0 \;=\; 0. \tag{3.18}$$

Due to the construction of the apparatus the hydrostatic stresses are the same in both sub-volumina:

$$T_0^{'} \;=\; T_0^{''}. \tag{3.19}$$

Finally, Hook's Law holds for averaged stress and strain:

$$T_0^{'} \;=\; C_{01}^{'} S_0^{'} \text{ and } T_0^{''} \;=\; C_{01}^{''} S_0^{''}, \tag{3.20}$$

where $C_{01}^{'}$ represents the first elastic tensor invariant for KCl and $C_{01}^{''}$ for NaCl. Combining Eq. (3.17-3.20) one obtains:

$$E^{*'}(0) \;=\; \frac{(1 - C_{01}^{''}/C_{01}^{'})E^{*'}(F)}{1 - G(\frac{a'}{a''})}, \tag{3.21}$$

where $G \;=\; \frac{C_{01}^{''}}{C_{01}^{'}} \frac{E^{*'}(F)}{E^{*''}(F)}$. Equation 3.21 can be used to determine $E^{*'}(0)$ on the basis of two photo energies that have been detected for KCl and NaCl at the same external force.

The results for two measurements are presented in the inset of Fig. 3.25. The $E^*(0)$ values for pure KCl (open circles) are independent from the applied load F which indicates that the conditions Eq.(3.18 - 3.20) are working well. The $E^{*'}(0)$ values for the doped

material CuCl(12%) : KCl (solid circles) for F = 0 t are 0.032 keV bigger than for pure KCl which indicates a reduction of the lattice parameter by doping. Extremely anomalous is the decrease of $E^{*'}(0)$ with the increase of F which corresponds to an external pressure. Thus, in both experiments the doping of NaCl and KCl by CuCl should be made responsible for the observed phenomenon. This view is supported by the three measurements performed in CuCl(0.8%):KCl—pure KCl, CuCl(3%):KCl—pure KCl and CuCl(6%):KCl—pure KCl. In all three cases the sum of the differences of doped KCl to pure KCl for F$\leq$ 10 (t) is positive and this supports the result of a contractive effect by the doping.

3.6.2 Phase transition in KCl under pressure

In order to investigate phase transition in KCl under external forces, two different samples have been considered. The first one represents CuCl(12%):KCl and the second one is pure KCl. Both samples have been (the samples are identical as in the previous Subsection: 3.6.1) measured with NaCl as a reference material. The diffracted intensity has been recorded as a function of the photon energies E in the range between 15 keV $<$ E $<$ 75 keV. The applied external force F drives the polymorphic phase transition in KCl from the B1 phase (NaCl structure) towards the B2 phase (CsCl structure). In the B1 (NaCl structure) phase the Bragg reflexes (200), (220), (222), (400), (420) and (422) have been detected. In the new phase B2 (CsCl structure) in KCl the reflexes (100), (110), (111), (200) and (210) have been recorded.

The photon energy E^*_{hkl} has been described in Eq. 3.16. In order to describe the transformation from the NaCl-structure to CsCl-structure, the anisotropic strain ΔS_{hkl} is used as experimental result in addition to the average compressive strain S.

$$-S \;=\; \frac{\overline{E^*_{hkl}}(F) - \overline{E^*_{hkl}}(0)}{\overline{E^*_{hkl}}(F)}, \tag{3.22}$$

where $\overline{E^*_{hkl}}(F)$ and $\overline{E^*_{hkl}}(0)$ are weighted averages of several photon energies E^*_{hkl} of the Bragg reflexes (hkl) observed at applied F forces and at ambient pressure F = 0 (t). The anisotropic strain is given by:

$$-\Delta S_{hkl} \;=\; \frac{E^*_{hkl}(F) - E^*_{200}(0)}{E^*_{hkl}(F) E^*_{200}(0)} E^*_{200}(0), \tag{3.23}$$

Figures 3.26 and 3.27 describe (-S) and $(-\Delta S)$ of pure and doped KCl as a function of applied external forces. Due to well-known hysteresis the observed phase transition appears at F_{obs} (see Fig. 3.26). The F_{obs} is significantly larger compared to the true transitions F_{tr}(see Fig. 3.27). The F_{tr} = 24 (t) represents the external applied forces. Usually, this is determined by observing the transition on increasing and decreasing $(-\Delta S)$ and assuming that the average represents the correct value. Fig. 3.26 also shows that the low pressure B1 phase in KCl does not vanish suddenly at F_{obs} = 29 (t) in KCl. Fig.3.26 shows that the new B2 phase in KCl can be felt in the second sub-volumina by NaCl (see open squares). Nevertheless, at F_{obs} = 29 t a slight change of the slope of NaCl is observed. A change of the sign suggests, that the observed anisotropy is at least not completely a

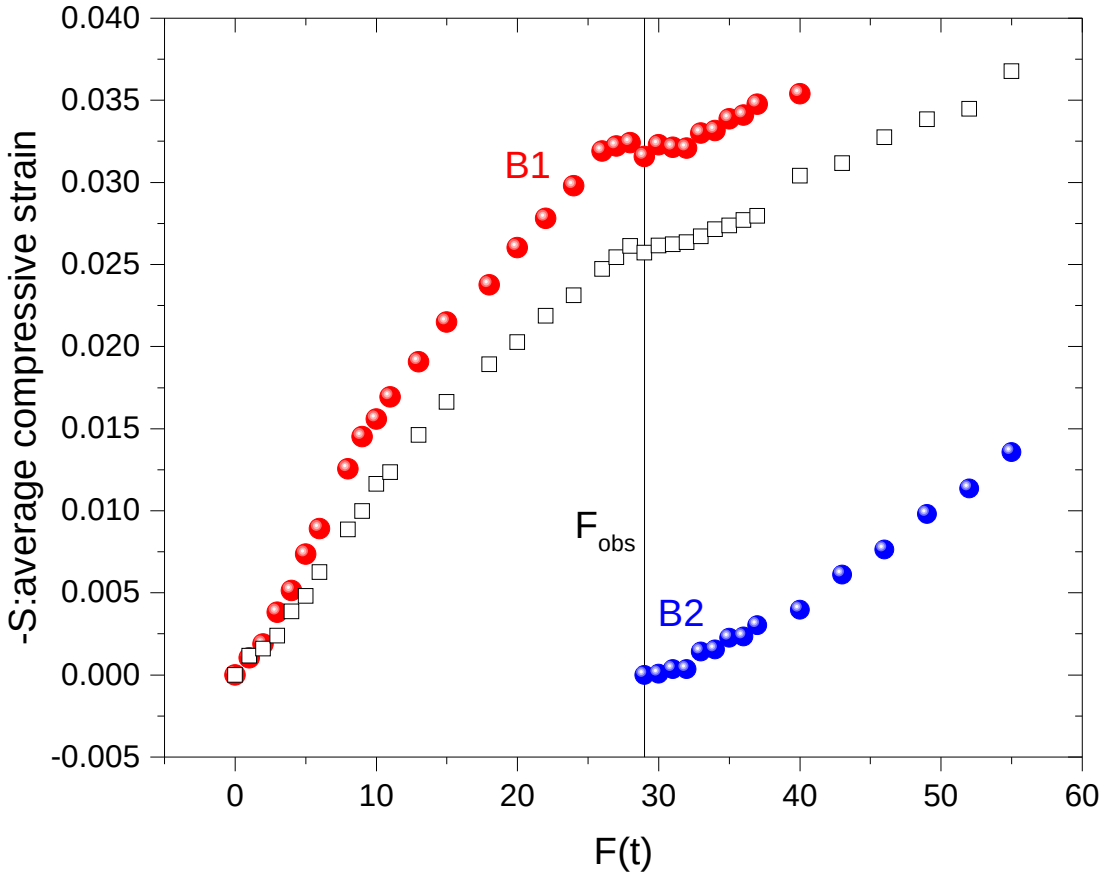

Figure 3.26: Average compressive strain:a)(red solid spheres) B1-phase in KCl and (blue solid spheres) B2 phase in KCl. (black open squares)-NaCl as a function of F.

misleading failure of the experimental setup (see Fig. 3.27). The anisotropic strain ΔS is determined in several samples (different CuCl amount) so that we can conclude that the friction and the plastic flow are also involved in the appearance of ΔS in KCl-powder.

Figure 3.28 shows the B1-B2 phase in pure and doped KCl. The B1 phase (NaCl structure) is characterized in both materials by a scattering effect and a small difference between these is observed. The scattering effect is defined as an anisotropic effect and this effect can be as a consequence of external applied pressure which generates a disorder in the grains structure. Nevertheless, the new phase B2 appears first in pure KCl (see Fig. 3.28 open red squares) and later in doped KCl. The B2 phase (CsCl-structure) in KCl seems to be the more stable structure and when increasing of external forces remains nearly constant. Obviously, in doped KCl the intensity of the Bragg reflex (100) is much higher compared to pure KCl. Thus, CuCl can amplify the effects in the B2 phase (CsCl structure) which belong to the (100) reflex.

A strong impact of doping has been observed at the phase transitions B1-B2 in KCl.

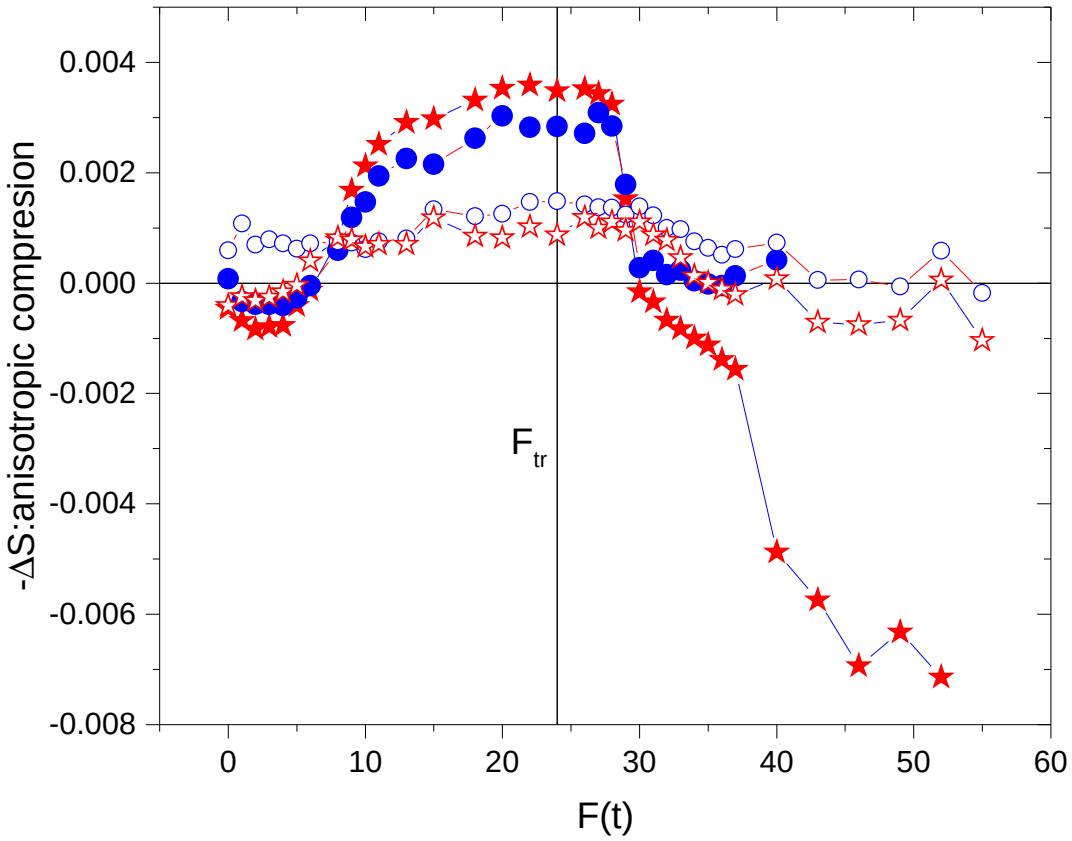

Figure 3.27: Anisotropic compression in CuCl:KCl: ΔS_{220} (solid red stars), ΔS_{420} (solid blue circles) and NaCl: ΔS_{220} (open red stars) and ΔS_{420} (open blue circles).

Up to F = 25 (t) a strong scattering effect has been found. As demonstrated in Fig. 3.28 the following differences in pure and in doped KCl have been detected.

I. The old phase B1 "vanishes" in pure KCl 5 t before it happened in the doped sample.

II. The onset of the new phase B2 in pure KCl is 3 t before it happened in the doped KCl.

III. The most interesting and strongest difference concerns the relative intensity of Bragg reflexes in doped KCl which is more than a factor two larger as in pure KCl.

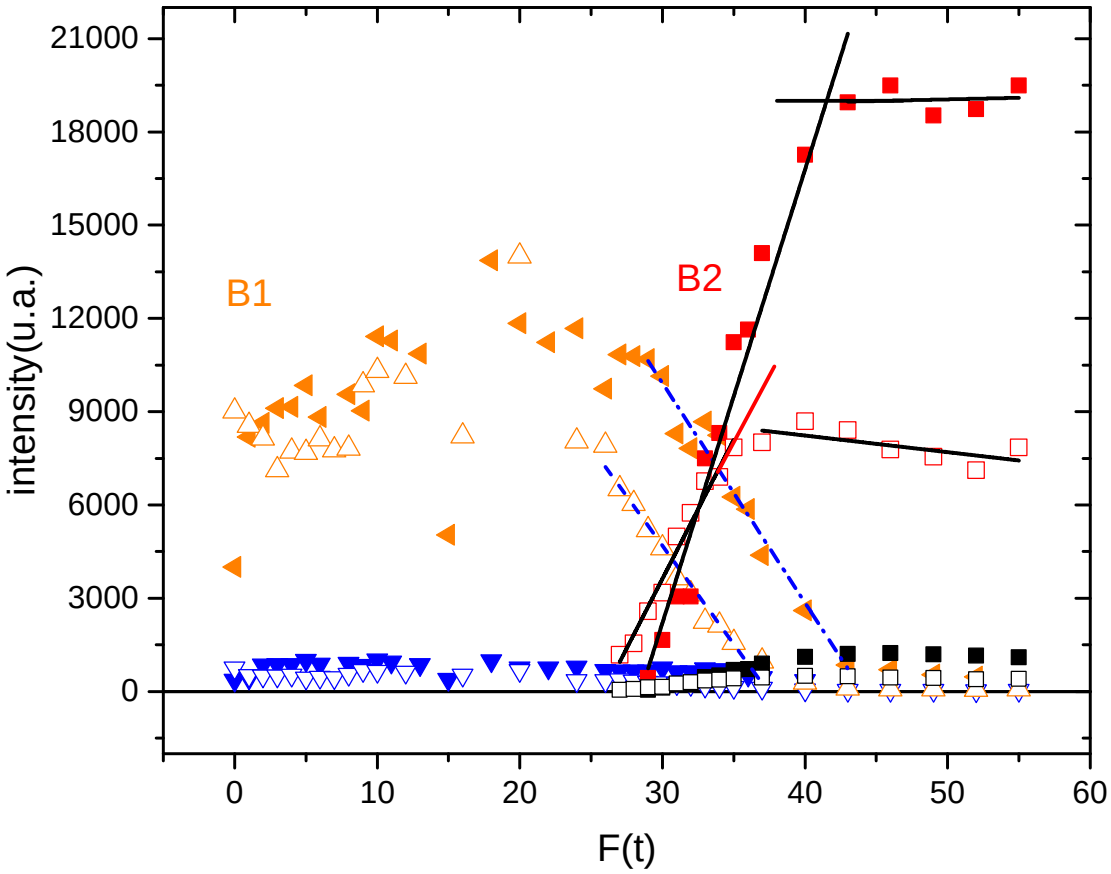

Figure 3.28: The intensities of the reflexes as a function of external force F(t). B1 phase:(200) and (220) as average (solid orange triangles) in CuCl(12%):KCl and (blue solid triangles) represent the average of the reflexes: (222), (400), (420) and (422) in CuCl(12%):KCl. Orange open triangles represent the average of the reflexes (200) and (220) in pure KCl and (blue open triangles) represent the average of the reflexes: (222), (400), (420) and (422) in KCl. B2 phase: (red solid squares) represent the reflex (100) in CuCl(12%):KCl and (black solid squares) represent the average of the reflexes (110), (111), (200) and (210). Red open squares represent the reflex (100) in pure KCl and (open black squares) represent the average of the reflexes (110), (111), (200) and (210) in pure KCl.

3.7 Method to manipulate the size of the nanocrystals

Optical absorption measurements in CuCl:NaCl provide the possibility to investigate the dissolution and the nucleation mechanisms of the nanocrystals in the NaCl matrix. The most important information are collected at low temperature, when the exciton resonance lines are determined. The experiments were performed in order to find a selection criterion

for the size of CuCl nanocrystals. An experimental procedure to select the size of CuCl nanocrystals embedded in NaCl matrix is given by cycle cooling combined with a warming process. Thermal treatment by heating and annealing represent anothers procedure to select the size of the nanocrystals. The heating procedure is applied for a short time to the sample at high temperature and the annealing procedure is described as an thermal process in the sample for a long time at lower temperature.

3.7.1 Subsequent cycle experiment

Subsequent temperature cycle experiments are performed in order to employ the size of CuCl nanocrystals. Those experiments were performed in one or two subsequent temperature cycles. A correlation between the size of the nanocrystals and the melting temperature of the nanocrystals has been found. Figure 3.29 shows the absorption spectra recorded at different temperatures in sample S2. The absorption spectrum (1) describes the first measurement and (4) the final one. A comparison of spectra (1) and (4) reveals a difference in the exciton positions Z_3 and $Z_{1,2}$. In spectrum (4) the positions of exciton lines Z_3 and $Z_{1,2}$ are shifted to lower photon energies. Using Eq. 1.16, the size of CuCl nanocrystals at low temperature 80 K from spectra (1) has been determined to be r = 1.6 nm [EE82]. The size of CuCl nanocrystals in the last cooling process (spectra (4)) is found to be r = 4.5 nm. The absorption coefficient illustrated in Fig 3.30 decreases continuously from T = 80 K (α_1) to T_1 = 380 K (α_2), and the slope is found as $\left(\frac{\partial\alpha}{\partial T}\right) = -0.0025\ (9.2 \cdot 10^{-5})\,(\mathrm{mm\,K})^{-1}$. This effect is attributed to the blue shift, broadening and thermal annihilation of excitons. At T_1 (α_2) small CuCl nanocrystals with a mean radius of r = 1.6 nm start to dissolve and the dissolution mechanism continues up to T_2 = 429 K (α_3). The slope between data points α_2 and α_3 is determined as $\left(\frac{\partial\alpha}{\partial T}\right) = -0.02\ (0.0016)\,(\mathrm{mm\,K})^{-1}$. The slope reflects the amount of the nanocrystals and the broadening of the exciton resonance lines Z_3 and $Z_{1,2}$ (see Fig. 3.29) when the absorption coefficient is changed. However, the nanocrystals with as large a size as determined at α_4 are considered to be the stable structures in the sample. The slope in the last cooling process is determined as $\left(\frac{\partial\alpha}{\partial T}\right) = -0.0015\,(\mathrm{mm\,K})^{-1}$, and the total amount of CuCl nanocrystals in S2 due to the dissolution process decreases (see Fig. 3.30).

Figure 3.31 describes the absorption coefficient in sample S3 during warming process. At 80 K (α) gives a mean radius of the nanocrystals r = 4.2 nm and the slope in the first heating stage is found to be $\left(\frac{\partial\alpha_1}{\partial T}\right) = -0.004\ (1.1 \cdot 10^{-5})\,(\mathrm{mm\,K})^{-1}$. Between $\beta \rightarrow \gamma$, the slope is found as $\left(\frac{\partial\alpha_2}{\partial T}\right) = -0.013\ (0.004)\,(\mathrm{mm\,K})^{-1}$. S4 is characterized by several temperature ranges (different linear fits) and obviously each temperature range describes a new dissolution process. In Fig. 3.32 three dissolution processes ((2), (3) and (4)) are illustrated. The slope is found to be $\left(\frac{\partial\alpha_1}{\partial T}\right) = -0.0011(5.1 \cdot 10^{-4})\,(\mathrm{mm\,K})^{-1}$. The linear fits are described by: (2) – $\left(\frac{\partial\alpha_3}{\partial T}\right) = -0.003\ (2.1 \cdot 10^{-4})\,(\mathrm{mm\,K})^{-1}$. (4) – $\left(\frac{\partial\alpha_4}{\partial T}\right) = -0.0014\ (4.10^{-4})\,(\mathrm{mm\,K})^{-1}$ and (5) – $\left(\frac{\partial\alpha_5}{\partial T}\right) = -7.74 \cdot 10^{-5}\,(\mathrm{mm\,K})^{-1}$.

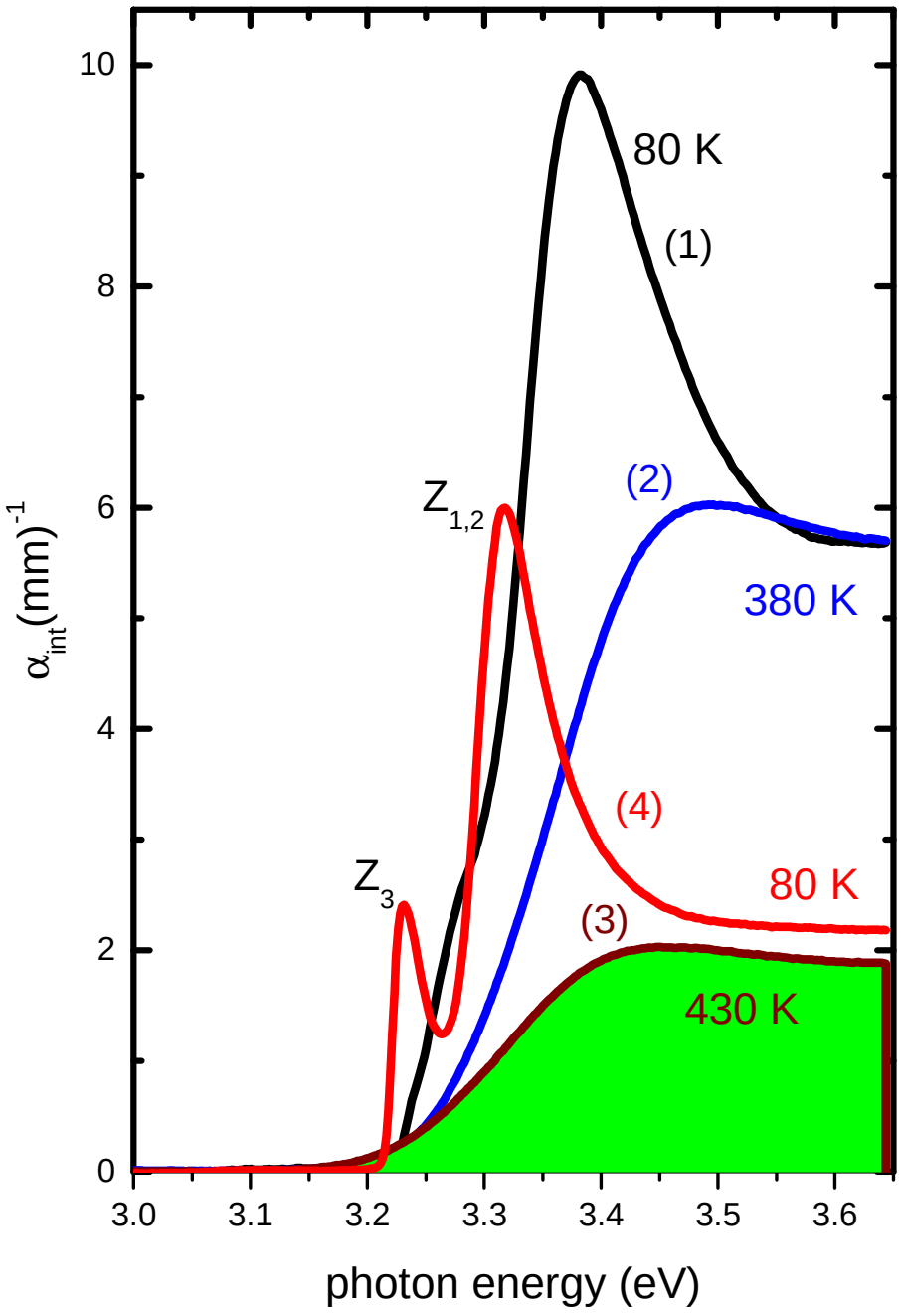

Figure 3.29: Absorption coefficient versus photon energy in sample S2. The absorption spectra were recorded in steps of 20 K degree during warming up.

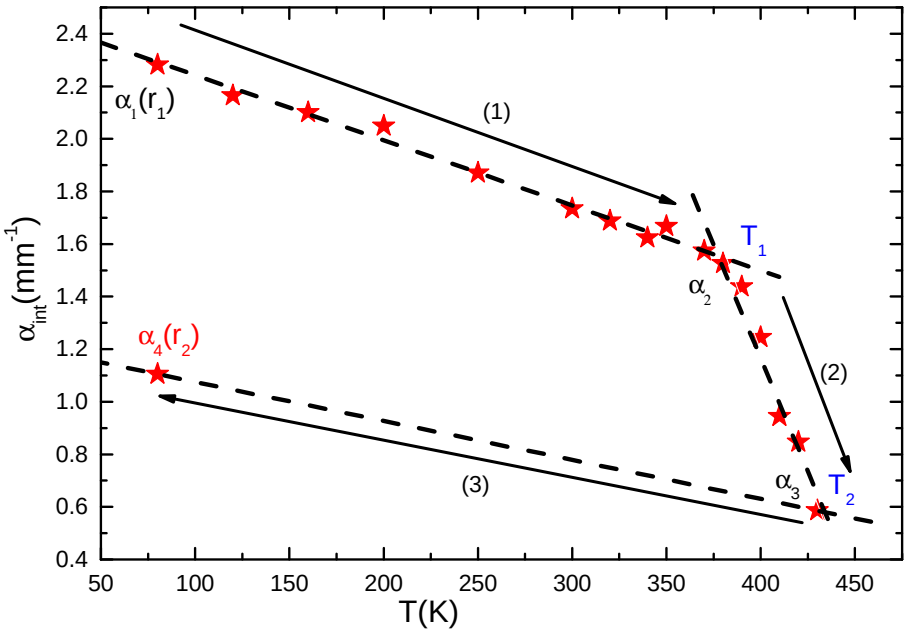

Figure 3.30: Integrated absorption of sample S2 measured in the temperature cycle presented in Fig 3.29. Data points α_1 and α_4 correspond to curves (1) and (4) recorded at 80 K. Between arrows (1)–(2) a warm-up process to 430 K is performed and (3) describes a cooling process to 80 K. $T_1 = 380$ K and $T_2 = 429$ K.

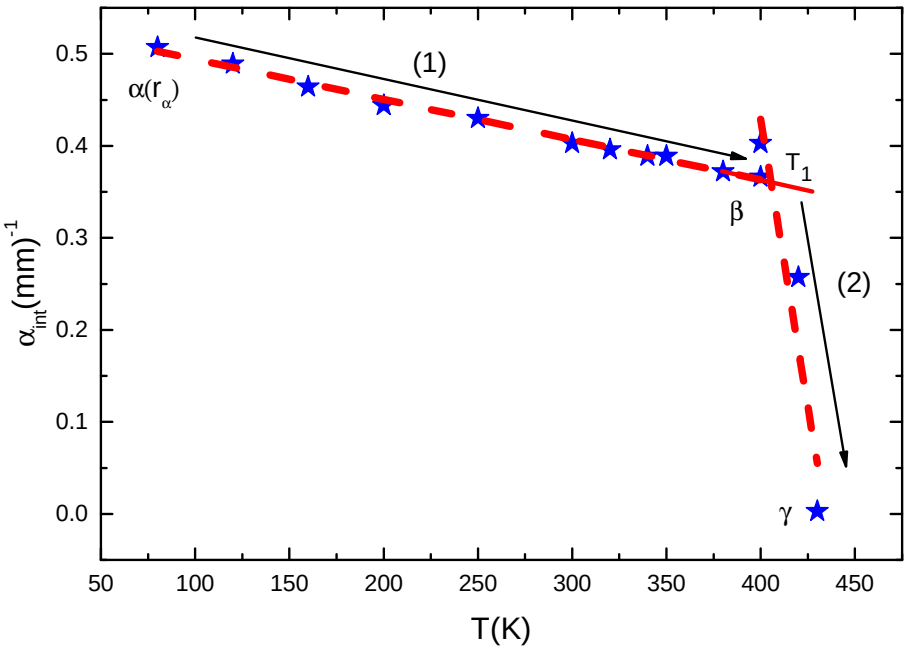

Figure 3.31: Integrated absorption in sample S3 measured during warming up process. The characteristic points are $\alpha = 80$ K , $\beta = 407$ K and $\gamma = 430$ K.

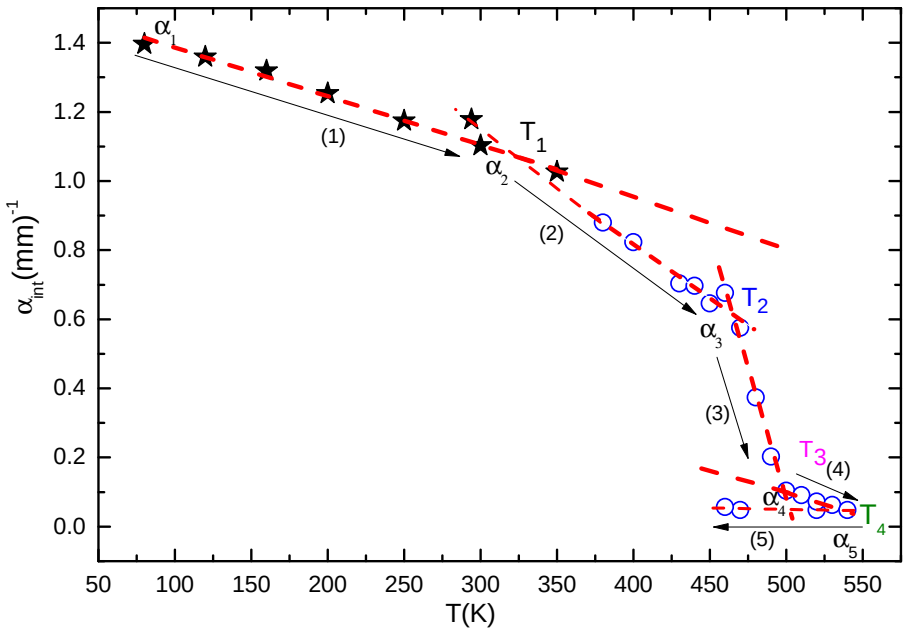

Figure 3.32: Integrated absorption of sample S4 measured during warming up. The same procedure as described in Fig. 3.31 and Fig. 3.30 has been applied. T_1 = 314 K, T_2 = 465 K, T_3 = 499 K and T_4 = 540 K.

In sample S5, the experiment is performed in two subsequent temperature cycles. The optical absorption measurements are performed during four days. The following nomenclatures have been used: 1^{st} measurement day (solid squares), 2^{nd} day (solid circles), 3^{rd} day (open stars) and the 4^{th} days (solid triangles). On the first day, the absorption measurements between 300 K $\rightarrow$ 80 K $\rightarrow$ 140 K are performed. At 80 K the mean radius of the nanocrystals is determined as r = 8.89 nm. A strong scattering in the cooling process is observed. On the 2^{nd} day, the measurements are performed between 80 K $\rightarrow$ 425 K. The mean radius of CuCl nanocrystals is determined at T = 200 K as r = 6.314 nm. The slope which describes curve (1) is $\left(\frac{\partial\alpha}{\partial T}\right)$ = -0.038 (0,00161) (mm K)$^{-1}$. The 3^{rd} day, the optical measurements have been recorded between 300 K$\rightarrow$ 481 K and the slope which describes curve (2) is $\left(\frac{\partial\alpha}{\partial T}\right)$ = -0.13 (0.008) (mm K)$^{-1}$; 80 K$\rightarrow$300 K. The slope which describes curve (3) is $\left(\frac{\partial\alpha}{\partial T}\right)$ = -0.026. In the last day, the measurements have been performed between 300 K$\rightarrow$470 K. The slope which describes curve (4) is $\left(\frac{\partial\alpha}{\partial T}\right)$ = -0.37 (0.0091) and 525 K$\rightarrow$80 K, $\left(\frac{\partial\alpha}{\partial T}\right)$ = -0.027.

The subsequent cycle experiment performed in sample S5 includes two dissolution processes:

1.) $\alpha_2 \rightarrow \alpha_3$, 2) $\alpha_3 \rightarrow \alpha_5$. Between α_1—α_2 a warming process is applied. The α_2 coincides with T = 425 K and CuCl nanocrystals (corresponding to α_1) with r = 6.3 nm have started to dissolve and the dissolution process continues up to α_3 corresponding with

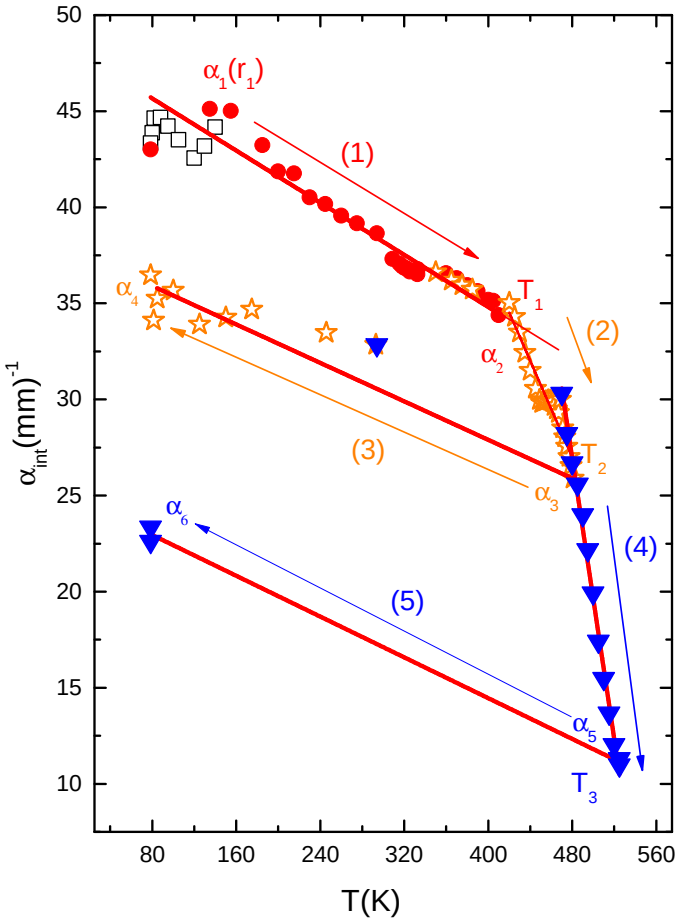

Figure 3.33: Integrated absorption of crystalline contribution in sample S5 measured in two subsequent temperature cycles. $T_1 = 314\,\mathrm{K}$, $T_2 = 465\,\mathrm{K}$, $T_3 = 499\,\mathrm{K}$ and $T_4 = 530\,\mathrm{K}$.

$T_2 = 491\,\mathrm{K}$. Between $\alpha_3 \rightarrow \alpha_4$ a cooling process is applied. Finally, in the subsequent experiment the size of the CuCl nanocrystals (corresponding to α_6) has been proved and the mean radius is determined at T = 80 K as r = 9.01 nm. However, the amount of CuCl nanocrystals in the dissolution processes decreases, though nanocrystals can be still be found in sample.

3.7.2 Thermal treatment: heating–annealing procedures

A doped NaCl crystal was cleaved into several thin plates, notated as S13, S14, S15, S16 and S17 (see Table 3.3). In each sample a different thermal treatment is applied in order to achieve nanocrystals of certain sizes. The thermal treatment is another possibility to select the sizes of the nanocrystals. The experimental samples have been thermal treated in two stages.

(I) First thermal stage is characterized by a heating process for 30 minutes at temperatures between 300° C and 700° C.

(II) The second thermal stage is characterized by an annealing process for 24 hours at 130° C. The annealing process will stimulate the growing process of the nanocrystals in matrix.

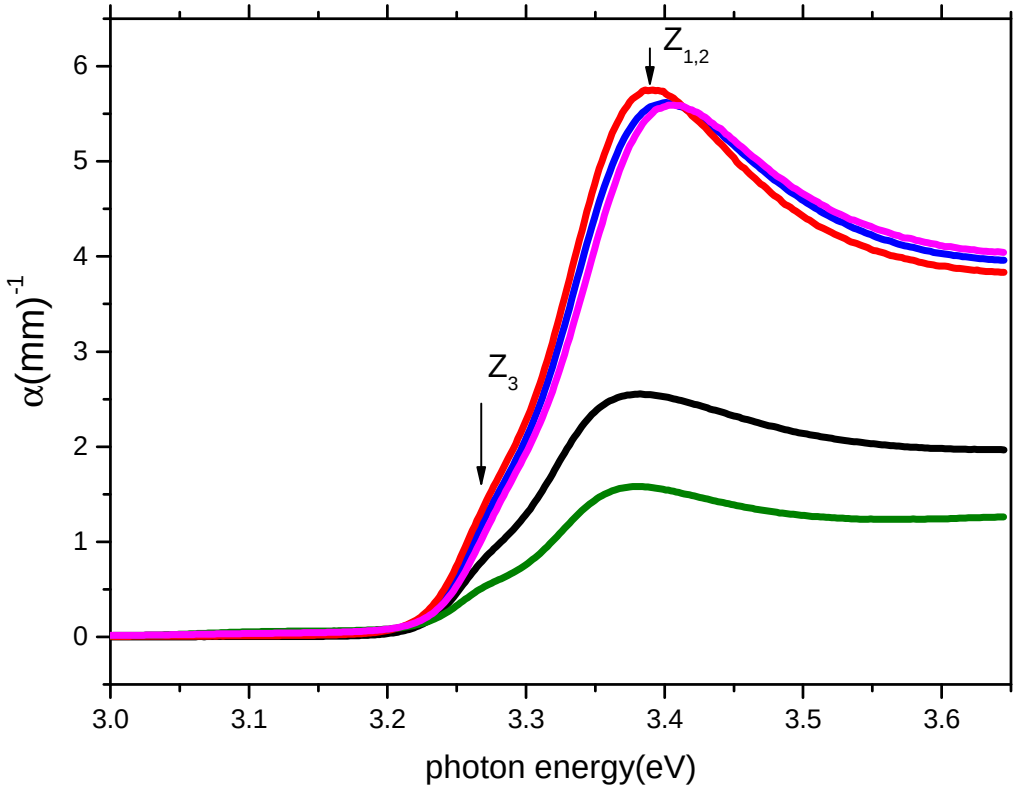

Figure 3.34: Absorption coefficient α versus photon energy E of CuCl:NaCl at room temperature in samples S13 (pink curve), S14 (blue curve), S15 (red curve), S16 (black curve) and S17 (olive curve). The thick arrows indicate the resonance lines Z_3 and $Z_{1,2}$.

The features of the optical spectra recorded at room temperature are illustrated in Fig. 3.34. At room temperature a broadening of the exciton lines Z_3 and $Z_{1,2}$ is observed and the exciton resonance lines are not resolved. At low temperature, the resonance lines are well separated and can be easily identified due to narrowing and the small linewidth.

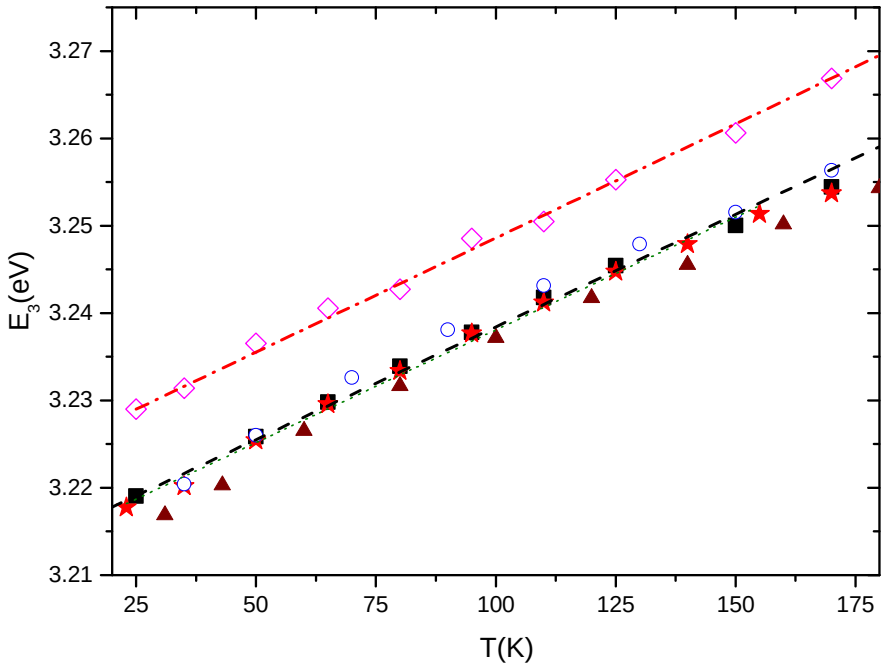

Figure 3.35: Spectral position of Z_3 exciton as a function of temperature in samples S13 (open diamonds), S14 (full squares), S15 (open circles), S16 (full stars), S17 (full triangles).

Even at room temperature, one can clearly see that the exciton lines are shifted towards higher energies compared to bulk CuCl, especially in samples S13 and S14. In samples S15, S16 and S17, the optical spectra recorded at room temperature are shifted to lower photon energies compared to S13 and S14. For sample S14 heated at $T_H = 400^\circ$ C a shift compared to the absorption spectra in S13 which was heated at $T_H = 300^\circ$ C is observed . At T = 25 K, the position of the Z_3 exciton line in sample S13 is determined as $E_3^{S13} = 3.22902$ eV and the size of $CuCl$ nanocrystals is determined as $r^{S13} = 2.84$,nm. The exciton line in sample S14 at T = 35 K is determined as $E_3^{S14} = 3.2204$ eV; the size of nanocrystals in sample S14 at 35 K is $r^{S14} = 4.8$ nm and $\Delta E_3 = E_3^{S14} - E_3^{13} = 0.0086$ eV. In sample S15 at T = 25 K the position of the exciton line $E_3^{S15} = 3.2189$ eV has been determinedand the size of CuCl nanocrystals is $r^{S15} = 4$ nm. In sample S16 at T = 23 K the position of the exciton is $E_3^{S16} = 3.2181,$eV and $r^{16} = 4.2$ nm, in sample S17 the central position of exciton resonance line Z_3 is $E_3^{S17} = 3.2169$ eV and the size of CuCl nanocrystals at T = 35 K is found to be $r^{17} = 5.8$ nm. Samples S13, S14, and S15 show nearly the same amount of CuCl nanocrystals even though the thermal procedures were different and the slope is determined as $\left(\frac{\partial\alpha}{\partial T}\right)$ = -0.001 $(4.4\cdot 10^{-5})\,(\mathrm{mm\,K})^{-1}$. In sample S16, the amount of CuCl nanocrystals is reduced by $\sim$ 15% compared to samples S13, S14, S15, and the slope is $\left(\frac{\partial\alpha}{\partial T}\right) = -0.0056\ (4.9\cdot 10^{-5})\,(\mathrm{mm\,K})^{-1}$. In sample S17 a strong reduction of CuCl nanocrystals by $\sim$ 55% is observed compared to samples S13,

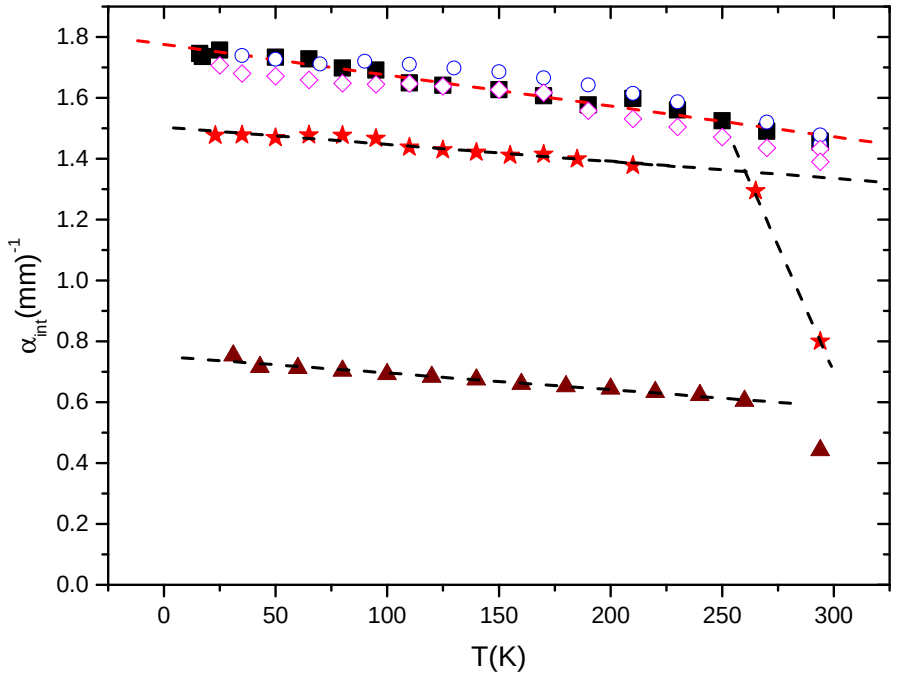

Figure 3.36: Integrated absorption of CuCl nanocrystals in the NaCl matrix in samples S13 (open diamonds), S14 (solid squares), S15 (open circles), S16 (solid stars), S17 (solid triangles).

S14, S15. The heating treatment in S17 is at higher temperature compared to the other samples. The slope (solid red triangles) is $\left(\frac{\partial\alpha}{\partial T}\right)$ = -0.0055 $(2.8{\cdot}10^{-5})$ $(\mathrm{mm\,K})^{-1}$.

3.7.3 Summary

The blue-shift in doped NaCl is used to estimate the average radii of the nanocrystals in sample. Comparing the positions of the exciton resonance lines in bulk *CuCl* with the positions of the exciton lines in doped NaCl, they are shifted to higher energies. Due to the Gibbs-Thomson effect, the thermal treatment or subsequent temperature cycle will reduce the stability of the nanocrystals in the matrix. Obviously, the Gibbs-Thomson effect predicts for nanocrystals with a small size a reduced melting temperature. In dissolution or melting processes, at first mainly the small particles are dissolved and the bigger nanocrystals are considered to be stable structures in the system. Information about the nucleation and growing processes of crystalline CuCl in NaCl structures are obtained when the crystal is rested for a well defined time at a certain growing temperature. In doped NaCl crystals a variety of nanocrystas sizes can be generated in samples due to different thermal conditions. The amount of CuCl nanocrystals depends on the thermal history of the sample. A thermal treatment performed at higher temperature allows one to obtaine big nanocrystals even though the amount of CuCl crystalline state in samples is reduced.

Chapter 4

Conclusion

The present work contributes to the search of anomalous effects in ionic crystals, and possible explications of those effects observed in pure NaCl and CuCl:NaCl. In general, the low doping effect of CuCl nanocrystals in NaCl matrix makes the detection of those anomalies very difficult and in a few cases nearly impossible to be observe. Usually, an anomalous effect is defined as a break of the opinions established so far or an effect which generally is not expected to be observed. It is well known, that in some crystals, the dislocations may have an important role on the physical properties of crystals. From one point of view the dislocations are considered to be an anomaly, those defects break the symmetry in the crystal.

Performing several experiments on pure and doped NaCl with different techniques, different distribution effects of dislocations have been detected. In many cases, the signature of the crystalline state of CuCl becomes more detectable by optical absorption measurements. In this work, CuCl nanocrystals are treated as quasi-stable elements which are embedded in the NaCl matrix. Due to the strong narrowing of the exciton resonance lines at low temperature, the size of the CuCl nanocrystals can be determined. In Section 3.7 several figures (see Fig. 3.30, Fig. 3.31, Fig. 3.32, Fig. 3.33, Fig. 3.36) demonstrate a stable behavior of nanocrystals before the melting process starts. The phenomenon has been used to produce samples with different distributions of sizes of the nanocrystals.

Most astonishing was observation that the widths of Bragg reflexes decreases with increasing CuCl concentration. This effect is a true anomaly for each crystal growth process. As the origin of the phenomenon the existence of the nanocrystals at the sample surfaces has been revealed. Their impact is considered as a pinning effect of dislocations, when they try to enter the material. The effect is of high importance for the continuation of experimental research in this type of material.

As illustrated in Fig. 3.6 and Fig. 3.7, the impacts of dislocations and the doping material on the lattice parameter are rather similar and of nearly the same order of magnitude in both type of materials. Therefore, it would have been difficult or even impossible to separate the influence of dislocations from true impacts of CuCl doping material. This statement is also true for optical birferingence measurements.

An unusual structural change has been observed in CuCl:NaCl at low temperatures.

In several experiments performed in different samples, a break of the normal linear dependence of E_3 as a function of temperature is observed. Considering the temperature dependence in detail, it is necessary to take into account the thermal expansion as a second source that activates structural changes. They are acting in addition to the elastic forces which stem from interaction between nanocrystals and matrix. The latter force is considered to be responsible for closing the original gap ΔR between nanocrystal and matrix at room temperature.

For analyzing more complex situations, a temperature range between 25 K and 175 K has been chosen as an appropriate linear range as illustrated in Fig. 3.14. Obviously, of a special interest is the 100 K point which shows a discontinuity in the slope. Figure 3.14 shows gradual realization of a discontinuity towards a simple linearity parallel to the reference line. The distances from the reference line are a measure of the nanocrystal size. Such a discontinuity of the slope appears very often in context of a phase transition. It is also important to note that a discontinuity of the slope have been observed in several samples as shown in Fig. 3.14, Fig. 3.15, Fig. 3.18, Fig. 3.20 and Fig. 3.21.

Obviously, there is a connection between the 100 K anomaly and the thermal expansion of CuCl (see Fig. 3.16). The quantitative strain analysis shows differences between CuCl and NaCl and discloses that the impact of thermal expansion of NaCl is more important. The observation at and below 100 K strongly suggests that at lest two different forces are needed for reliable interpretation. In addition, the reaction of the exciton E_3 below 100 K is known from Two-Photon-Absorption[Ro94, HW98]. An additional indicator which helps to analyze the anomaly and the observation that mainly relative big nanocrystals are involved and the ability of the strain between nanocrystals and matrix from the thermal expansion data. Taking into account all these ingredients, it became obvious that an explanation of the observed anomalies needs more experimental data.

The prediction formulated as a consequence of equilibrium Eq. 1 contained the body-forces by doping and this was realized in optical birefringence measurements. Figure 3.11 shows a zero value of ellipticity $\epsilon_{(0)}$ in the right and in the left side before the laser met the surface of the samples. The later effect was predicted by Eq. 1. Nevertheless, $\epsilon_{(0)}(x_s)$ adopts in both sides the predicted zero values. In fact, all measurements exhibited zero values of birefringence inside the sample but not necessarily at the both surfaces. This behavior is consistent with the model of elastic domains presented in Fig. 3.17. It demands the vanishing of normal stress at the surface of the samples if a non-elastic connection to the surrounding exists. Approximately, this happened for all domains at the surface region. Attempts to develop the structure of internal stress field have to consider the displacement tensor with addition of a strain gradient and by taking into account the symmetry elements of the samples. These attempts are missing.

Finally, the search for self-organized internal stress resulted in the construction of the frame effect illustrated in Fig. 3.12. The frame effect observed in optical birefringence measurements (see Fig. 3.12) has been described by a negative value of the elasto-optical coefficient $(p_{11} - p_{12})$ of NaCl. It should be noticed that such a frame has been observed in a doped KCl sample and the $(p_{11} - p_{12})$ of KCl is positive. Thus, the birefringent frame should be considered as a more general phenomenon in low doped ionic crystals. These

results tell us that the self-organization of the stress field is not easily obtained by simply adding the effects of inter-domain forces. Another proof of the importance of the frame effect is the observation of the elastic-fluid effect in RUS experiments described in Fig. 3.23 and Fig. 3.24.

An anomalous increase of the lattice parameter by external pressure has been observed. Most likely, this effect is explainable by a reaction of an elastic screening to external pressure as is demonstrated by the frame effect. On the other hand, the existence of internal stress in doped material is demonstrated in Fig. 3.25 by the KCl inset. An anomalous effect is observed by a weak pressure up to 10 t.

Acknowledgments

I am lucky in having benefited from the support, teaching and guidance of some truly excellent people during the time taken for this PhD. It is a pleasure, therefor, to accord those involved (directly and otherwise) a grateful and heartfelt acknowledgment.

I would like to express my deepest graduate to my supervisor Prof. Dr. Manfred Bayer, for giving me the opportunity to work on this research project, for his cordiality and all his continuous support. Thank you kindly for all the great support, advice and supervision over the time.

Prof. Dr. Hans-Jürgen Weber deserves my sincere thanks for reviewing of this work and for may fruitful discussions. Thank you for all advises and estimable help and especially for contributing his expertise to this work.

Furthermore, I would like to thank Prof. Dr. Dietmar Fröhlich for insightful discussion and encouragement.

Also thanks are expressed to all members of the Experimentalle Physik E II and my office mates for making me feel welcome and their myriad of helpful hints for survival in- and outside the work environment.

Special thanks go to Dr. Marc Aßmann, Dr. Jörg Debus and Dr. Sergiu Anghel for their constructive criticisms and helpful corrections. Thank you for all this time.

I would like to thank my colleagues: Johannes Mund, Fabian Heisterkamp, Julian Heckoetter for their constructive discussion.

To my family; my sister Dana for her support and love. Last but not least, this work would not have been possible without the relentless support and love of my mother Doina and the continuous inspiration drawn from my son and my daughter, Maximilian and Emma, who through patience and understanding proved again to be my life's driving force. Their unwavering support, encouragement and love has been foundation for all endeavors. To them, I dedicate this thesis.

Bibliography

[Abr03] Farid F. Abraham*. How fast can cracks move? A research adventure in materials failure using millions of atoms and big computers. *Advances in Physics*, 52(8):727–790, December 2003.

[ABT+06] B. Amrani, T. Benmessabih, M. Tahiri, I. Chiboub, S. Hiadsi, and F. Hamdache. First principles study of structural, elastic, electronic and optical properties of CuCl, CuBr and CuI compounds under hydrostatic pressure. *Physica B: Condensed Matter*, 381(1-2):179–186, May 2006.

[AG93] Hillar Aben and Claude Guillemet. *Photoelasticity of Glass*. Springer Berlin Heidelberg, Berlin, Heidelberg, 1993.

[Ame58] S. Amelinckx. Dislocations in ionic crystals. *Nuovo Cimento Suppl.*, 7:569–99, 1958.

[And66] O.L. Anderson. The use of ultrasonic measurements under modest pressure to estimate compression at high pressure. *J.Phys.Chem.Solids*, 27:547–565, 1966.

[BAD+04] D. Balzar, N. Audebrand, M. R. Daymond, A. Fitch, A. Hewat, J. I. Langford, A. Le Bail, D. Louër, O. Masson, C. N. McCowan, N. C. Popa, P. W. Stephens, and B. H. Toby. Size–strain line-broadening analysis of the ceria round-robin sample. *Journal of Applied Crystallography*, 37(6):911–924, December 2004.

[Baj74] K. K. Bajaj. Fine Structure of Excitonic Lines in Cuprous Chloride. *physica status solidi (b)*, 64(2):K107–K110, August 1974.

[Bas68] William A. Bassett. Pressure-Induced Phase Transformation in NaCl. *Journal of Applied Physics*, 39(1):319, 1968.

[BBW77] T. H. K. Barron, J. A. Birch, and G. K. White. Thermal expansion and heat capacity of cuprous chloride at low temperatures. *Journal of Physics C: Solid State Physics*, 10(10):1617, 1977.

[BCC86] A. Blacha, N. E. Christensen, and M. Cardona. Electronic structure of the high-pressure modifications of CuCl, CuBr, and CuI. *Physical Review B*, 33(4):2413, 1986.

[BEI96] L. E. Brus, A.L. Efros, and T. Itoh. Spectroscopy of Isolated and Assembled Semiconductors Nanocrystals. *Special Issus of J. of Luminescence*, 69(North-Holland), 1996.

[BK93] Ladislaus Bányai and Stephan W. Koch. *Semiconductor Quantum Dots*. World Scientific, 1993. Google-Books-ID: JdjVkrCsL8gC.

[BL73] A. Baldereschi and Nunzio O. Lipari. Spherical model of shallow acceptor states in semiconductors. *Physical Review B*, 8(6):2697, 1973.

[BP05] DAVOR Balzar and NICOLAE C. Popa. Analyzing microstructure by Rietveld refinement. *The Rigaku Journal*, 22(1):16, 2005.

[BRB97] Reinhard Boehler, Marvin Ross, and David B. Boercker. Melting of LiF and NaCl to 1 Mbar: Systematics of ionic solids at extreme conditions. *Physical Review Letters*, 78(24):4589, 1997.

[Bri40] P.W. Brigdman. The compression of 46 substances to 50,000 kg/cm 2. *Proc.Am.Acad.Arts Sci.*, 74:21–51, 1940.

[Bri45] P.W. Brigdman. The compression of twenty-one halogen compounds and eleven other simple substances to 100,000 kg/cm 2. *Proc.Am.Acad.Arts Sci.*, 76:1–7, 1945.

[Bru83] L. E. Brus. A simple model for the ionization potential, electron affinity, and aqueous redox potentials of small semiconductor crystallites. *The Journal of Chemical Physics*, 79(11):5566–5571, December 1983.

[Bue30] M.J. Buerger. Translation-Gliding in Crystals. *American Mineralogist*, 15:45, 1930.

[BZ68] E.V. Burisan and O.I. Zaikowski. Changes in the curvature of a ferroelectric film due to polarization. *Sov.Phys.Solid State*, 10:1121–24, 1968.

[Car63] Manuel Cardona. Optical properties of the silver and cuprous halides. *Physical Review*, 129(1):69, 1963.

[CG75] Alan J. Cohen and Roy G. Gordon. Theory of the lattice energy, equilibrium structure, elastic constants, and pressure-induced phase transitions in alkali-halide crystals. *Physical Review B*, 12(8):3228, 1975.

[CPR58] G. Caglioti, A. Paoletti, and F. Ricci. Choice of colimators for a crystal spectrometer for neutron diffraction. *Nuclear Instrument*, 3:223–228, 1958.

[Cro06] L. Eric Cross. Flexoelectric effects: Charge separation in insulating solids subjected to elastic strain gradients. *Journal of Materials Science*, 41(1):53–63, 2006.

[CSG04] G. Catalan, L. J. Sinnamon, and J. M. Gregg. The effect of flexoelectricity on the dielectric properties of inhomogeneously strained ferroelectric thin films. *Journal of Physics: Condensed Matter*, 16(13):2253, 2004.

[CST85] A. A. Cafolla, S. E. Schnatterly, and C. Tarrio. Translational Mass of an Exciton. *Physical Review Letters*, 55(25):2818–2821, December 1985.

[Dec71] D. L. Decker. High-Pressure Equation of State for NaCl, KCl, and CsCl. *Journal of Applied Physics*, 42(8):3239, 1971.

[DHRW98] A. Diegeler, M. Haselhoff, W. Rammensee, and H.-J. Weber. Observation of CuCl Clusters in NaCl By SCANNING NEAR-FIELD OPTICAL MICROSCOPY. *Solid State Communications*, 105:269–272, 1998.

[Dom34] S. Dommerich. Kritische Schubspannung des Würfelflächentranslationssystems NaCl. *Z.Phys.*, 90:189, 1934.

[DPP65] A.N. Dremin, S.V. Pershin, and V.F. Pogorelov. Structure of shock waves in KCl and KBr under compression to 200 000 atm. *Combustion, Explosion, and Shock Waves*, Vol.1, No.4:3–9, 1965.

[Dul69] W. Dultz. Uniaxial Stress Effects on Parity-forbidden Transitions in NaCl:Cu+ and KCl:Ag+. *physica status solidi (b)*, 34(1):95–104, January 1969.

[DW79] N. J. Doran and A. M. Woolley. The band structure of CuCl. *Journal of Physics C: Solid State Physics*, 12(8):L321, 1979.

[EE82] Al L. Efros and A.L. Efros. Interband absorption of light in a semiconductor sphere. *Sov.Phys.Semicond.*, 1982.

[EE91] A. I. Ekimov and Al L. Efros. Optics of Zero Dimensional Semiconductor Systems. *Acta Physica Polonica A*, 79(1):5–14, 1991.

[EEO85] Alexey I. Ekimov, Al L. Efros, and Alexei A. Onushchenko. Quantum size effect in semiconductor microcrystals. *Solid State Communications*, 56(11):921–924, 1985.

[Ell57] R. J. Elliott. Intensity of optical absorption by excitons. *Physical Review*, 108(6):1384, 1957.

[EO81] A. I. Ekimov and A. A. Onushchenko. Quantum size effect in three-dimensional microscopic semiconductor crystals. *JETP Lett*, 34:345–349, 1981.

[FCL99] J. Fousek, L. E. Cross, and D. B. Litvin. Possible piezoelectric composites based on the flexoelectric effect. *Materials Letters*, 39(5):287–291, June 1999.

[FHR95] D. Fröhlich, M. Haselhoff, and K. Reimann. Determination of the Orientation of CuCl Nanocrystals in a NaCl Matrix. *Solid State Communications*, 94, 1995.

[Fus69] K. Fussgaenger. On the UV Absorption of Heavy Metal Ions in Alkali Halide Crystals I. Experimental Results. *physica status solidi (b)*, 34(1):157–169, January 1969.

[FZL+07] J.Y. Fu, W.Y. Zhu, N. Li, N.B. Smith, and L. E. Cross. Gradient scaling phenomenon in microsize flexoelectricit piezoelectric composite. *Appl.Phys.Lett.*, 91, 2007.

[GCSC90] A. R. Goñi, A. Cantarero, K. Syassen, and M. Cardona. Effect of pressure on the low-temperature exciton absorption in GaAs. *Physical Review B*, 41(14):10111, 1990.

[Gil59] J.J. Gillmann. Plastic Anisotopy of LiF and Other Rock Salt Type Crystals. *Acta.Metall.*, 7:608, 1959.

[GN70] E.Yu Gutmanas and E.M. Nadgorny. Dislocation Motion in SEcondary Slip PLanes in Alkali Halide Crystals at Room Temperature. *Phys.Stat.Sol (A)*, 38, 1970.

[Gol77] A. Goldmann. Band Structure and Optical Properties of Tetrahedrally Coordinated Cu- and Ag-Halides. *physica status solidi (b)*, 81(1):9–47, May 1977.

[GRC+98] A. Göbel, T. Ruf, M. Cardona, C. T. Lin, J. Wrzesinski, M. Steube, K. Reimann, J.-C. Merle, and M. Joucla. Effects of the isotopic composition on the fundamental gap of CuCl. *Physical Review B*, 57(24):15183–15190, June 1998.

[GW83] A. Goldmann and D. Westphal. Band structure and optical properties of CuCl: an angle-resolved study of secondary electron emission. *Journal of Physics C: Solid State Physics*, 16(7):1335, 1983.

[Hay74] D. B. Hayes. Polymorphic phase transformation rates in shock-loaded potassium chloride. *Journal of Applied Physics*, 45(3):1208, 1974.

[Hes65] J. Hesse. Die plastische Verformung von Natriumchlorid Von. *physica status solidi (b)*, 9(1):209–230, January 1965.

[Hul75] D. Hull. *Introduction to Dislocation*, volume Volume 16. Pergamon Press, Pergaon International Librar, 1975.

[HV11] Jiawang Hong and David Vanderbilt. First-principles theory of frozen-ion flexoelectricity. *Physical Review B*, 84(18):180101, November 2011.

[HW98] M. Haselhoff and H.-J. Weber. Nanocrystal growth in alkali halides observed by exciton spectroscopy. *Physical Review B*, 58(8):5052, 1998.

[IIK88] T. Itoh, Y. Iwabuchi, and M. Kataoka. Study on the Size and Shape of CuCl Microcrystals Embedded in Alkali-Chloride Matrices and Their Correlation with Exciton Confinement. *physica status solidi (b)*, 145(2):567–577, February 1988.

[JKL24] A. Joffe, M.W. Kniripitschewa, and M.A. Lewitsky. Röntgenographische Bestimmung des Platizitätsbeginns und seiner Temperaturabhängigkeit. Temperaturabhänigkeit der Reißfestigkeit. *Z.Physik Bd.*, 22:286, 1924.

[KDWS63] George F. Koster, John O. Dimmock, Robert G. Wheeler, and Hermann Statz. *The Properties of the Thirty-Two Point Groups*. MIT Press, Cambridge (Mass.), December 1963.

[KGFU74] Y. Kato, T. Goto, T. Fujii, and M. Ueta. The effect of High Density Excitons on the Exciton Bands in CuCl. *J.Phys.Soc.Jpn.*, 36:169, 1974.

[KK71] Y. Kaifu and T. Komatsu. Exciton line-width and exciton-phonon interaction in CuCl. *physica status solidi (b)*, 48(2):K125–K128, December 1971.

[KKN74] Georgii Vyacheslavovich Kurdyumov and N. V. Klassen-Neklyudova. Progress in the theory of strength and plasticity of solids (A review of AV Stepanov's works). *Soviet Physics Uspekhi*, 16(6):828, 1974.

[KKT06] S. V. Karpenko, A. Kh Kyarov, and A. I. Temrokov. Structural phase transitions of the B1–B2 type in small-sized ionic crystals. *Physics of the Solid State*, 48(3):570–576, 2006.

[Kli01] C. Klingshirn. 4 III-V Semiconductors. In C. Klingshirn, editor, *Optical Properties. Part 1*, number 34C1 in Landolt-Börnstein - Group III Condensed Matter, pages 96–96. Springer Berlin Heidelberg, 2001. DOI: 10.1007/10479578_14.

[KM92] Bart Kahr and J. Michael McBride. Optically Anomalous Crystals. *Angewandte Chemie International Edition in English*, 31(1):1–26, January 1992.

[KMK05] Takahiro Kinoshita, Tsutomu Mashimo, and Katsuyuki Kawamura. The mechanism and effect of defects in the B1–B2 phase transition of KCl under high pressure: molecular dynamics simulation. *Journal of Physics: Condensed Matter*, 17(6):1027–1035, February 2005.

[Kog64] S.M. Kogan. Piezoelectric effect during inhomogeneous deformation and acoustic scattering of carriers in crystals. *Sov. Phys. Solid State*, 5(10), 1964.

[KPS+06] Christof Krywka, Michael Paulus, Christian Sternemann, Martin Volmer, Arndt Remhof, Gregor Nowak, Alexei Nefedov, Birgit Pöter, Michael Spiegel, and Metin Tolan. The new diffractometer for surface X-ray diffraction at beamline BL9 of DELTA. *Journal of Synchrotron Radiation*, 13(1):8–13, January 2006.

[KR74] A. Kuske and C. Robertson. *Photoelastic Stress Analysis*. John Wiley & Sons Ltd, London; New York, January 1974.

[KS04] J.-D. Kamminga and L. J. Seijbel. Diffraction Line Broadening Analysis if Broadening Is Caused by Both Dislocations and Limited Crystallite Size. *Journal of Research of the National Institute of Standards and Technology*, 109(1):65–74, 2004.

[LB89] Landolt-Börnstein. *Zahlenwerte unf Funktionen aus Naturwissenschaft und Technick , Neue Serie*, volume III/23a. Springer-Verlag,Berlin, 1989.

[LL70] L.D Landau and E.M Lifsvhitz. *Theory of Elasticity*, volume VII. Berlin, Mittler, 1970.

[Lut56] J. M. Luttinger. Quantum theory of cyclotron resonance in semiconductors: General theory. *Physical Review*, 102(4):1030, 1956.

[LW97] R.G. Leisure and F.A. Willis. Resonant ultrasound spectroscopy. *J.Phys.Condes.Matter*, 9:6001–6029, 1997.

[Mad12] Otfried Madelung. *Semiconductors: Data Handbook*. Springer Science & Business Media, December 2012. Google-Books-ID: R0rmCAAAQBAJ.

[Mah29] A Mac Mahon. Zur Kenntnisder Alkalihalogenidphosphoren mit Kupferzusatz. *Z.Phys.*, 52:336, 1929.

[MC01] Wenhui Ma and L. Eric Cross. Observation of the flexoelectric effect in relaxor Pb(Mg1/3nb2/3)O3 ceramics. *Applied Physics Letters*, 78(19):2920–2921, May 2001.

[MC02] Wenhui Ma and L. Eric Cross. Flexoelectric polarization of barium strontium titanate in the paraelectric state. *Applied Physics Letters*, 81(18):3440–3442, October 2002.

[MC03] Wenhui Ma and L. Eric Cross. Strain-gradient-induced electric polarization in lead zirconate titanate ceramics. *Applied Physics Letters*, 82(19):3293–3295, May 2003.

[MC05] Wenhui Ma and L. Eric Cross. Flexoelectric effect in ceramic lead zirconate titanate. *Applied Physics Letters*, 86(7):072905, February 2005.

[MC06] Wenhui Ma and L. Eric Cross. Flexoelectricity of barium titanate. *Applied Physics Letters*, 88(23):232902, June 2006.

[MG65] P.P.M Meincke and G.M. Graham. The Thermal Expansion of Alkali Halides. *Canadian Journal of Physics*, 43, 1965.

[MI67] V. Meisalo and O. Inkinen. An X-ray diffraction analysis of potassium bromide. *Acta Crystallographica*, 22(1):58–65, 1967.

[MKK95] Yasuaki Masumoto, Kanae Kawabata, and Tadashi Kawazoe. Quantum size effect and persistent hole burning of CuI nanocrystals. *Physical review B*, 52(11):7834, 1995.

[MNT+02] Tsutomu Mashimo, K. Nakamura, K. Tsumoto, Y. Zhang, Shinji Ando, and H. Tonda. Phase transition of KCl under shock compression. *Journal of Physics: Condensed Matter*, 14(44):10783, 2002.

[MS97] Albert Migliori and John L. Sarrao. *Resonant Ultrasound Spectroscopy*. John Wiley & Sons Ltd, 1997.

[MS09] R. Maranganti and P. Sharma. Atomistic determination of flexoelectric properties of crystalline dielectrics. *Physical Review B*, 80(5):054109, August 2009.

[MSW+93] R. Matzdorf, J. Skonieczny, J. Westhof, H. Engelhard, and A. Goldmann. Band structure and optical properties of CuBr: new photoemission results. *Journal of Physics: Condensed Matter*, 5(23):3827, 1993.

[MT57] V.S. Maskevich and K.B. Tolpygo. Electrical, optical andelastic properties of diamond type crystals. *Sov.Phys.JETP*, 5:435–439, 1957.

[MTK03] Yanming Ma, John S. Tse, and Dennis D. Klug. Pressure-induced phonon instabilities in copper chloride. *Physical Review B*, 67(14), April 2003.

[MWK92] Yasuaki Masumoto, Tetsuro Wamura, and Tomohiro Kawamura. Size selective nonlinear optical spectroscopy of excitons in CuCl quantum dots. *Surface science*, 267(1):315–318, 1992.

[Neu23] F. E. (Franz Ernst) Neumann. *Beiträge zur Krystallonomie*. Berlin, Mittler, 1823.

[Nik80] S. Nikitine. Exciton spectroscopy and polariton dispersion. *Journal of Molecular Structure*, 59:273–289, 1980.

[NTH02] N. Narita, Y. Takahara, and K. Higashida. Brittle-to-ductile transition and slip band structure in ionic crystals. *Philosophical Magazine A*, 82(17-18):3229–3239, November 2002.

[Oht07] Eiji Ohtani. *Advances in High-pressure Mineralogy*. Geological Society of America, January 2007. Google-Books-ID: e9cB522h65MC.

[Ove62] William C. Overton. Relation between Ultrasonically Measured Properties and the Coefficients in the Solid Equation of State. *The Journal of Chemical Physics*, 37(1):116, 1962.

[PC96] C. H. Park and D. J. Chadi. Ground state structural anomalies in cuprous halides: CuCl. *Physical review letters*, 76(13):2314, 1996.

[PGM84] Stephen A. Payne, Andrea B. Goldberg, and Donald S. McClure. Two-photon spectroscopy of ions in crystals: Cu+ and Ag+ in the alkali halides. *The Journal of Chemical Physics*, 81(4):1529, 1984.

[PLR+94] A. Martín Pendás, V. Luana, J. M. Recio, M. Flórez, E. Francisco, M. A. Blanco, and L. N. Kantorovich. Pressure-induced B1-B2 phase transition in alkali halides: General aspects from first-principles calculations. *Physical Review B*, 49(5):3066, 1994.

[Res10] Raffaele Resta. Towards a Bulk Theory of Flexoelectricity. *Physical Review Letters*, 105(12), September 2010.

[RFF+02] J. M. Recio, M. Flórez, E. Francisco, M. A. Blanco, and A. Martín Pendás. Microscopic Study of the Rock Salt-Caesium Chloride Phase Stability in Alkali Halides. *High Pressure Research*, 22(2):443–446, January 2002.

[RMGN67] P.F. Raga, A. Myyrowicz, J.B. Grun, and S. Nikitine. The position, the intensity and the lifetime of the emission lines of CuCl as a function of temperature. *J.Phys.(France),Collog.*, 28:C3–116–C3–119, 1967.

[Ro94] K. Reimann and others. Two-photon absorption in CuCl and CuBr under hydrostatic pressure. *Physical Review B*, 49(16):11021, 1994.

[Sad14] A. Sadonnini. Phase Digrams for Ceramists. *Gazz.Chim.ital.*, 44:327, 1914.

[SB55] A.V. Stepanov and V.P. Bobrikov. Dependence of the optical elasticity limit determined on the basis of system (111):[011] upon temperature for rock salt crystals. *Sov.Phys.JETP, Engl.Transl.*, 1:177–181, 1955.

[SBS79] Jai Shanker, P. S. Bakhshi, and L. P. Sharma. Analysis of the crystal binding and the Anderson-Gruneisen parameters in the halides of copper (I), silver (I) and thallium (I). *Journal of Inorganic and Nuclear Chemistry*, 41(9):1285–1288, 1979.

[Sea81] W Skrotzki and et al. Plasticity of Polycrystalline Ionic Solids. *Phys.Stat.Sol (A)*, 66, 1981.

[SGB03] P. Sharma, S. Ganti, and N. Bhate. Effect of surfaces on the size-dependent elastic state of nano-inhomogeneities. *Applied Physics Letters*, 82(4):535, 2003.

[Sha76] RD t Shannon. Revised effective ionic radii and systematic studies of interatomic distances in halides and chalcogenides. *Acta Crystallographica Section A: Crystal Physics, Diffraction, Theoretical and General Crystallography*, 32(5):751–767, 1976.

[SI38] M. Straumanis and A. Ievins. Die Drehkristallmethode als Präzisionsverfahren und deren Vergleich mit der Pulvermethode. *Z.Physik*, 109:728, 1938.

[Sma27] A. Smakula. Einige Absorptionsspektra von Alkalihalogenidphosphore mit Silber und Kupfer als wirksamen Metallen. *Z.Phys.*, 45:1, 1927.

[SPK07] A. G. Shtukenberg, Y. Punin, and Bart Kahr. *Optically anomalous crystals*. Springer, Dordrecht, 2007. OCLC: ocm76363474.

[Spr76] M. T Sprackling. *The plastic deformation of simple ionic crystals*. Academic Press, London; New York, 1976. OCLC: 2975439.

[SSS13] D. B. Sirdeshmukh, L. Sirdeshmukh, and K. G. Subhadra. *Alkali Halides: A Handbook of Physical Properties*. Springer Science & Business Media, March 2013. Google-Books-ID: wCvrCAAAQBAJ.

[SSVdO93] U. Scholle, H. Stolz, and W. Von der Osten. Resonant Raman scattering and luminescence from size-quantized indirect exciton states in AgBr microcrystals. *Solid state communications*, 86(10):657–661, 1993.

[Sys69] P. A. Sysiö. On the additivity of crystal radii in alkali halides. *Acta Crystallographica Section B: Structural Crystallography and Crystal Chemistry*, 25(11):2374–2378, 1969.

[Tag86] A. K. Tagantsev. Piezoelectricity and flexoelectricity in crystalline dielectrics. *Physical Review B*, 34(8):5883, 1986.

[Tag91] A.K Tagantsev. Electric polarization in crystals and its response to thermal and elastic perturbations. *Phase Transit.*, 35:119–203, 1991.

[TLE+11] B. Toudic, R. Lefort, C. Ecolivet, L. Guérin, R. Currat, P. Bourges, and T. Breczewski. Mixed Acoustic Phonons and Phase Modes in an Aperiodic Composite Crystal. *Physical Review Letters*, 107(20):205502, November 2011.

[Tol63] K.B. Tolpygo. Long wavelength oscillations of diamond-type crystals including long range forces. *Sov. Phys. Solid State*, 4:1297–1305, 1963.

[UGRB01] T. Ungár, J. Gubicza, G. Ribárik, and A. Borbély. Crystallite size distribution and dislocation structure determined by diffraction profile analysis: principles and practical application to cubic and hexagonal crystals. *Journal of applied crystallography*, 34(3):298–310, 2001.

[UIN65] M. Ueta, M. Ikazawa, and S.-I. Nagasaka. Luminiscence of copper doped NaCl crystal with high concentration. *J.Phys.Soc.Jpn.*, 20:1724, 1965.

[VBPK73] S. N. Vaidya, S. Bailey, T. Pasternack, and G. C. Kennedy. Compressibility of fifteen minerals to 45 kilobars. *Journal of Geophysical Research*, 78(29):6893–6898, October 1973.

[VW26] Martin Volmer and A. Weber. Keimbildung in übersttätigten Gebilden. *Z.Phys.Chem.*, 1926.

[Wan37] Gregory H. Wannier. The Structure of Electronic Excitation Levels in Insulating Crystals. *Physical Review*, 52(3):191–197, August 1937.

[Web95] H.-J. Weber. Determination of internal strain by optical measurements. *Physical Review B*, 51(18):12209, 1995.

[WKLPV05] H.-J. Weber, H.-L. Keller, C. Lathe, and C. Popa-Varga. X-ray powder diffraction of NaCl under pressure: Nanocrystals induce anomalous strains. *Journal of Applied Physics*, 98(3):034317, 2005.

[Wog97] Ulrike Woggon. *Optical Properties of Semiconductor Quantum Dots*, volume 136 of *Springer Tracts in Modern Physics*. Springer Berlin Heidelberg, Berlin, Heidelberg, 1997.

[WSPV04] H.-J. Weber, J. Schreuer, and C. Popa-Varga. Elastic interaction between CuCl nanocrystals and a matrix of crystalline NaCl. *Physical Review B*, 69(23), June 2004.

[WYK94] Cheng-Zhang Wang, Rici Yu, and Henry Krakauer. First principles linear response calculations of lattice dynamics for CuCl. *Physical review letters*, 72(3):368, 1994.

[YOA87] Shigeriu Yamamoto, Ichiro Ohno, and Orson L. Anderson. High Temperature Elasticity of Sodium Chloride. *J.Phys.Chem.Solids*, 48:143–151, 1987.

[Yof93] A.D. Yoffe. Low-dimensional systems: quantum size effects and electronic propertiesof semiconductors microcrystallites and some quasi tw-dimensional systems. *Adv.Phys.*, 42:173, 1993.

[Zac31] W.H. Zachariasen. A set of empirical crystal radii for ions with inert gas configuration. *Z.Kristallogr.*, 80:137–53, 1931.

[ZC79] Alex Zunger and Marvin L. Cohen. Electronic structure of CuCl. *Physical Review B*, 20(3):1189, 1979.

[ZCB+08] P. Zubko, G. Catalan, A. Buckley, P. R. L. Welche, and J. F. Scott. Erratum: Strain-Gradient-Induced Polarization in SrTiO 3 Single Crystals [Phys. Rev. Lett. **99** , 167601 (2007)]. *Physical Review Letters*, 100(19), May 2008.

[ZCT13] Pavlo Zubko, Gustau Catalan, and Alexander K. Tagantsev. Flexoelectric Effect in Solids. *Annual Review of Materials Research*, 43(1):387–421, 2013.

List of Tables

List of Figures